# Novel Concepts for the Advancement & Miniaturization of Hyperspectral Imaging

Zur Erlangung des akademischen Grades eines
DOKTORS DER INGENIEURWISSENSCHAFTEN
von der KIT-Fakultät für Maschinenbau des
Karlsruher Instituts für Technologie (KIT)

genehmigte

**DISSERTATION**

von

M.Sc. Mohammad Abdo


| | |
|---|---|
| Tag der mündlichen Prüfung: | 04.12.2024 |
| Referent: | Prof. Dr. Jan G. Korvink |
| Koreferent: | Prof. Dr. rer. nat. Robert Brunner |

*In Loving Memory of My Beloved Father*

*Dr. Refaat Abdo*

*(1953 – 2021)*

# Abstract

Hyperspectral imaging (HSI) has emerged in recent years from the combination of optical spectroscopy and digital 2D imaging as a powerful modality for chemical analysis at scale. By providing a spectrum for every pixel in an image, the material composition and its spatial distribution can be determined for a variety of samples in a rapid, non-invasive, and contact-free manner. This technology holds great potential for public health, with demonstrated applications in the areas of food safety and early disease detection.

With the motivation to unlock this potential, this thesis focuses on the spatial-scan data acquisition technique, as an optimal match for health applications, and addresses two main challenges restricting its widespread adoption – the limited flexibility and adaptability to meet varying application requirements, and the limited progress in miniaturization to offer mobile and affordable systems. Adopting an "inside approach" in design and construction, this thesis introduces two novel spatial-scan systems based on employing internal active components to scan the target while eliminating the relative motion between system and target prevailing in conventional spectrographs.

The first system combines an internal piezoelectric line-scanning unit with a rotating camera mechanism, enabling a dual-mode system capable of switching between spatial and spectral imaging. A novel feed-forward compensation function is incorporated to automatically synchronize the motion of active components during data acquisition and enable higher flexibility, without compromising system performance. The second system combines a rotating slit to scan the target and a co-rotating Dove prism to realign the transmitted light with the diffraction grating to prevent spectral crosstalk and ensure a simplified data acquisition procedure.

This thesis also undertakes the miniaturization of the rotating slit mechanism as an initial step towards overall system miniaturization. The miniaturized mechanism is realized on a thin glass chip, based on the principles of electromagnetic inductive levitation and electrostatic actuation, to levitate and rotate an aluminum slit disc with defined electrodes resembling a three-phase motor. The levitation 3D wire-bonded microcoils and the actuation electrodes are combined on a single chip with an improved double-sided microfabrication process, opening new venues for micro-levitation in optical applications.

# Zusammenfassung

Die Hyperspektrale Bildgebung (HSI) hat sich in den letzten Jahren aus der Kombination von optischer Spektroskopie und digitaler 2D-Bildgebung zu einer leistungsstarken Methode für chemische Analysen im großen Maßstab entwickelt. Dabei wird jedem Pixel in einem Bild ein separates elektromagnetisches Spektrum zugeordnet womit die Materialzusammensetzung und ihre räumliche Verteilung für eine Vielzahl von Proben schnell, nicht-invasiv und kontaktfrei bestimmt werden. Diese Technologie besitzt ein enormes Potenzial für die öffentliche Gesundheit, mit nachgewiesenen Anwendungen in den Bereichen Lebensmittelsicherheit und Früherkennung von Krankheiten.

Mit der Motivation, dieses Potenzial zu nutzen, fokussiert sich diese Dissertation auf die räumliche Abtasttechnik als optimale Lösung für Gesundheitsanwendungen und behandelt zwei Hauptprobleme, die ihre vielseitigere Anwendung einschränken: die limitierte Flexibilität und Anpassungsfähigkeit an unterschiedliche Anwendungsanforderungen sowie die begrenzten Fortschritte in der Miniaturisierung zur Bereitstellung mobiler und kostengünstiger Systeme. Durch die Anwendung des “Inside-Ansatzes” in den Design- und Konstruktionsprozess stellt diese Dissertation zwei neuartige räumliche Abtastsysteme vor, die auf der Verwendung interner aktiver Komponenten zur Abtastung des Ziels basieren und die relative Bewegung zwischen System und Ziel, die in herkömmlichen Spektrographen vorherrscht, eliminieren.

Das erste System kombiniert eine interne piezoelektrische Linienabtastungseinheit mit einem rotierenden Kameramechanismus und ermöglicht ein Dual-Mode-System, das zwischen räumlicher und spektraler Bildgebung wechseln kann. Eine neuartige Feed-Forward-Kompensationsfunktion wird integriert, um die Be-

wegung der aktiven Komponenten während der Datenerfassung automatisch zu synchronisieren und eine höhere Flexibilität zu ermöglichen, ohne die Systemleistung zu beeinträchtigen. Das zweite System kombiniert einen rotierenden Schlitz zur Abtastung des Ziels sowie ein sich mitdrehendes Dove-Prisma, um das übertragene Licht mit dem Beugungsgitter auszurichten, sodass spektrale überlagerungen zu Verhindert werden. Darüber hinaus wird so ein vereinfachtes Datenerfassungsverfahren sichergestellt.

Diese Dissertation befasst sich weiterhin mit der Miniaturisierung des rotierenden Schlitzmechanismus als ersten Schritt zur Gesamtminiaturisierung des Systems. Der miniaturisierte Mechanismus wird auf einem Chip bestehend aus einem dünnen Glassubstrat Realisiert und basiert auf den Prinzipien der elektromagnetischen induktiven Levitation sowie dem elektrostatischen Antrieb. Durch diese Kombination wird eine Aluminium-Schlitzscheibemit definierten Elektroden, die einem Drei-Phasen-Motor ähneln, levitiert und gedreht. Die Levitation erfolgt durch dreidimensional drahtgebondete Mikrospulen. Die Antriebselektroden sind auf lediglich einem Chip kombiniert, der mit einem optimierten doppelseitigen Mikroherstellungsverfahren hergestellt wurde, was neue Möglichkeiten für die Mikrolevitation in optischen Anwendungen schafft.

# Nomenclature

## List of Abbreviations

| Abbreviation | Meaning |
|---|---|
| 1D | 1-dimensional |
| 2D | 2-dimensional |
| 3D | 3-dimensional |
| AC | Alternating current |
| AOTF | Acousto-optic tunable filter |
| APTF | Active-plasmonic tunable filter |
| CAD | Computer-aided design |
| CASSI | Coded aperture snapshot spectral imager |
| CCD | Charge-coupled device |
| CMOS | Complementary metal-oxide-semiconductor |
| CTIS | Computed tomography imaging spectrometry |
| CVF | Circular variable filter |
| DBR | Distributed Bragg reflector |
| DC | Direct current |
| DFG | Deutsche Forschungsgemeinschaft |
| DI | Deionized |
| DLW | Direct laser writing |
| DMD | Digital micromirror device |
| DP | Dove prism |
| DRIE | Deep reactive-ion etching |
| E. coli | Escherichia coli |

| Abbreviation | Meaning |
|---|---|
| EAGLE | Effizenz adaptiven Gittern und Linsen aus Elastomeren |
| EPO | European Patent Office |
| FAB | Free Air Ball |
| FSR | Free spectral range |
| FWHM | Full width at half maximum |
| HSI | Hyperspectral imaging |
| IAR | Institute for Anthropomatics and Robotics |
| ICP | Inductively coupled plasma |
| IIIT | Institute of Industrial Information Technology |
| IMEC | Interuniversity Microelectronics Centre |
| IMST | Institute for Microsystems Technology |
| IMT | Institute of Microstructure Technology |
| IR | Infrared |
| LCTF | Liquid crystal tunable filter |
| LED | Light-emitting diode |
| LIDT | Laser induced damage threshold |
| LVF | Linear variable filter |
| MEMS | Micro-electromechanical systems |
| MLA | Microlens array |
| NASA | National Aeronautics and Space Administration |
| OPD | Optical path difference |
| PCB | Printed circuit board |
| PEB | Post-exposure bake |
| PHARAO | Portable Hyperspectral Analysis by Real-Time Optical Unmixing |
| PM | Proof mass |
| POFA | Programmable Optical Filter Array |
| RF | Radio frequency |
| RGB | Red, green and blue |

| Abbreviation | Meaning |
|---|---|
| RIE | Reactive-ion etching |
| rms | Root mean square |
| STDEV | Standard deviation |
| USAF | United States Air Force |
| UV | Ultraviolet |
| VNIR | Visible and near-infrared |
| VSI | Vertical scanning interferometry |

## List of Symbols

| Symbol | Meaning | Unit |
|---|---|---|
| $A$ | Area | $\mathrm{m}^2$ |
| $\vec{B}$ | Magnetic flux density | T |
| $C$ | Capacitance | F |
| $d$ | Distance | m |
| $\vec{E}$ | Electric field | $\mathrm{V/m}$ |
| $F_e$ | Electrostatic force | N |
| $\vec{F}_L$ | Lorentz force | N |
| $h$ | Levitation height | µm |
| $I_L$ | Levitation coil current | A |
| $I_S$ | Stabilization coil current | A |
| $I_o$ | Amplitude of input current | A |
| $I_e$ | Eddy current | A |
| $J$ | Eddy current density | $\mathrm{A/m}^2$ |
| $k_e$ | Coulomb's constant | $\mathrm{N\,m}^2/\mathrm{C}^2$ |
| $L$ | Inductance | H |
| $\ell$ | Image line transmitted through slit aperture | |
| $\ell(\theta)$ | Image line transmittance angle | ° |
| $\ell(\theta_{\mathrm{ref}})$ | Image line reference angle | ° |

| Symbol | Meaning | Unit |
|---|---|---|
| $M$ | Number of slit positions for a complete scan | |
| $m$ | Diffraction order | |
| $N_c$ | Number of coil windings | |
| $N_G$ | Number of illuminated grating slits | |
| $N_{(x,y)}$ | Number of sampling times of an image point | |
| $q$ | Electric charge | C |
| $R$ | Resistance | Ω |
| $r_{(x,y)}$ | Radius at sampling point | m |
| $r_{in}$ | Inner radius of stator and rotor electrodes | m |
| $r_{out}$ | Outer radius of stator and rotor electrodes | m |
| $U$ | Energy stored | J |
| $V$ | Voltage | V |
| $\vec{v}$ | Velocity | m/s |
| $Z$ | Impedance | Ω |
| $\mathscr{D}$ | Angular dispersion of a grating | °/nm |
| $\delta$ | Skin depth | m |
| $\varepsilon_0$ | Permittivity of free space | F/m |
| $\varepsilon_r$ | Relative permittivity | |
| $\Lambda$ | Grating period | µm |
| $\lambda$ | Wavelength | nm |
| $\mu_o$ | Permeability of vacuum | H/m |
| $\mu_r$ | Relative permeability | |
| $\omega$ | Angular frequency of input current | rad/s |
| $\Phi$ | Magnetic flux | Wb |
| $\mathscr{R}$ | Chromatic resolving power of a grating | |
| $\sigma$ | Electrical conductivity | S/m |
| $\tau_e$ | Electrostatic torque | N m |
| $\theta_i$ | Incidence angle of light beam | ° |
| $\theta_m$ | Diffraction angle in diffraction order $m$ | ° |

| Symbol | Meaning | Unit |
|---|---|---|
| $\theta_{Camera}$ | Rotation angle of camera mechanism | ° |
| $\theta$ | Slit rotation angle | ° |
| $\theta_s$ | Step angle of rotating slit | ° |
| $\theta_{\text{SlitArc}}$ | Arc angle defined by slit width | ° |
| $\theta_{rotor}$ | Arc of rotor electrode | ° |
| $\theta_{stator}$ | Arc of stator electrode | ° |
| $\theta_{overlap}$ | Overlap angle between stator & rotor electrodes | ° |
| $\xi$ | Electromotive force | V |
| Al | Aluminum | |
| Ar | Argon | |
| Au | Gold | |
| $Au_2S$ | Gold(I) sulfide | |
| $CHF_3$ | Trifluoromethane (Fluoroform) | |
| Cr | Chromium | |
| Cu | Copper | |
| HF | Hydrofluoric acid | |
| Hg | Mercury | |
| I/KI | Iodine potassium-iodide | |
| $O_2$ | Oxygen | |
| PGMEA | Propylene glycol methyl ether acetate | |
| pH | Measure of acidity or basicity | |
| Si | Silicon | |
| PSi | Porous Silicon | |
| $Si_3N_4$ | Silicon nitride | |
| $SiO_2$ | Silicon dioxide | |

# Contents

# 1 Introduction

## 1.1 What is Hyperspectral Imaging

Hyperspectral imaging (HSI) is an emerging technology, which combines the techniques of conventional 2D imaging and optical spectroscopy. This combination enables identifying the material composition of the objects in an image. This is achieved by acquiring a spectrum for every pixel in the image, as illustrated in Figure 1.1. The acquired spatial and spectral data are represented using two spatial dimensions and one spectral dimension, forming a 3D dataset often referred to as the "Hyperspectral Data Cube", as illustrated in Figure 1.2.

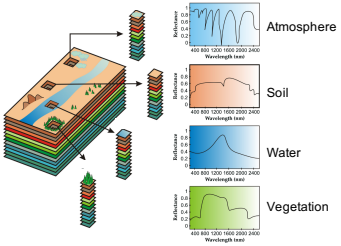


**Figure 1.1:** Hyperspectral imaging provides a spectrum for every pixel in an image (reproduced from [1] ©2007 IEEE).

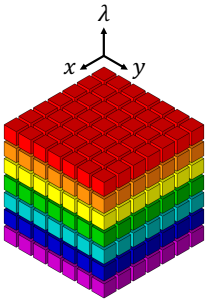


**Figure 1.2:** Representation of the hyperspectral data cube with two spatial dimensions and one spectral dimension [2].

While conventional color imaging is limited to only three bands (red, green, and blue), hyperspectral imaging acquires data across many contiguous spectral bands, up to several hundred bands [3]. The spatially resolved spectral information reveals the chemical composition of the target in a contact-free non-destructive fashion.

Hyperspectral imaging was originally developed by NASA in the mid 1980's for remote sensing applications [4]. Over the past few decades, and owing to its unique information, HSI has found many applications in other disciplines including precision agriculture [5, 6], industrial sorting [7–9], security [10–12], and environmental monitoring [13, 14]. Examples for such applications are shown in Figure 1.3

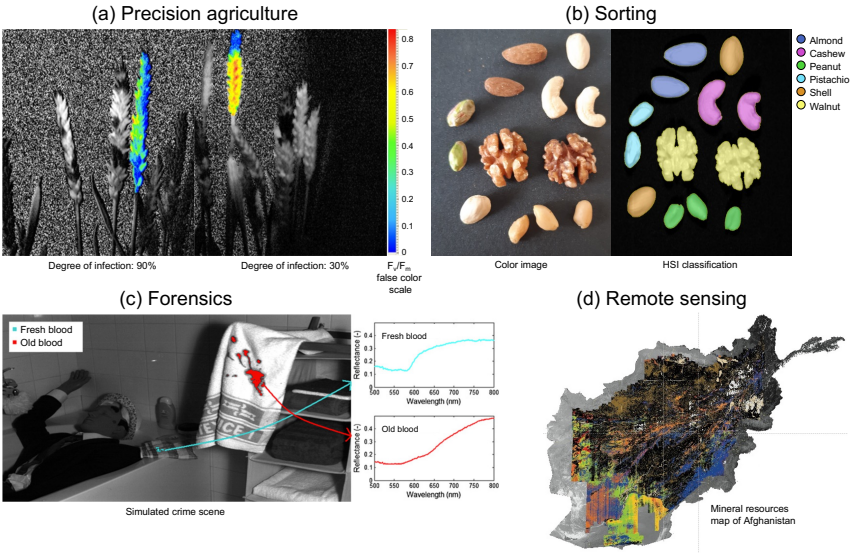


**Figure 1.3:** HSI application examples in different fields: (a) Precision agriculture: early detection of plant diseases (reproduced from [6], licensed under CC BY 3.0). (b) Sorting: distinguishing different kinds of nuts (reproduced from [9] ©2021 SPIE) . (c) Forensics: distinguishing fresh & old blood stains in a simulated crime scene (reproduced from [12] ©2012, with permission from Elsevier). (d) Remote sensing: mapping surface materials & mineral resources (adapted from [15]. Public domain).

## 1.2 Motivation

Public health is one of the areas where hyperspectral imaging can have a significant impact on society. This can be realized by using hyperspectral imaging for the prevention and early detection of diseases. One important step towards better

prevention of diseases is ensuring the safety of food products and maintaining a healthy food intake. On the other hand, the early and fast diagnosis of diseases improves the chances of treatment. Figure 1.4 shows some use cases that demonstrate the potential of HSI in public health applications as a tool for health monitoring, medical diagnosis, and food analysis.

In the area of food safety and quality, hyperspectral imaging is receiving growing interest due to the wide range of applications it can serve as a contact-free and non-destructive analysis tool. The traditional methods in this area include visual inspection by human labour and sending food samples to microbiology labs and waiting up to several days for the results. Compared to these methods, hyperspectral imaging offers rapid detection of contamination with high accuracy and high throughput.

The potential of HSI in the assessment of food safety and quality was demonstrated in several studies on different kinds of food including meat, vegetables, fruits, and grains. A review paper by Huang et al. cites over fifty studies in this area [20]. Examples include quantifying the concentration of bacteria in beef and pork and estimating their shelf life [21, 22], revealing defects within cucumbers and pickles [23], detecting bruises in apples [24], identifying expired salmon [25], and detecting biofilms of Salmonella and E. coli on surfaces of materials that come in contact with the food during handling and processing such as stainless steel and granite [26].

In the area of medical diagnostics, HSI demonstrated high potential as a non-invasive and rapid detection technique, based on several studies in the literature. Lu et al. gathered a large number of these studies in his review of medical hyperspectral imaging [27]. One of the main applications is the detection of cancer. In one study, Dicker et al. distinguished between benign and malignant dermal tissue based on their spectral differences [28]. In another study, Liu et al. was able to recognize tongue tumor with a success rate of 96.5 % [29]. Panasyuk et. al. demonstrated that HSI can be a useful tool in guided-surgery by identifying small residual tumor during tumor resection [17]. In relation to diabetes, Yudovsky et al. used HSI to assess the risk of developing diabetic foot ulceration [30]. In

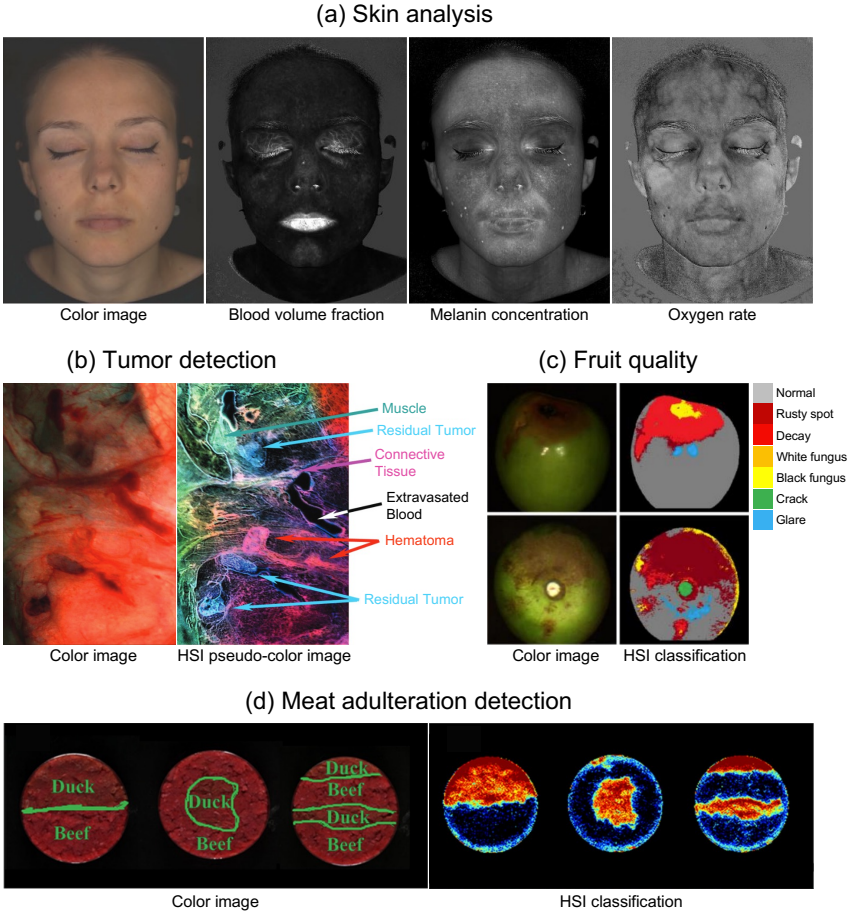


**Figure 1.4:** Public health application examples of HSI in the areas of medical diagnostics and food safety. (a) Facial skin analysis: mapping blood volume fraction, melanin concentration, and oxygen rate (reproduced from [16] ©2020 John Wiley & Sons). (b) Guided surgery: distinguishing between different tissues and detecting residual tumor (reproduced from [17] ©2007 Taylor & Francis). (c) Fruit quality: classification of skin defects in jujube (adapted from [18], licensed under CC BY 4.0). (d) Food adulteration: detection of minced beef adulteration with duck meat (adapted from [19] ©2019, with permission from Springer Nature).

ophthalmology, a study demonstrated using HSI to monitor ischemia, which can lead to blindness, by mapping the oxygen saturation in the retina [31]. In dentistry, HSI showed potential for the early detection of caries [32].

For hyperspectral imaging to fulfill its potential in serving the public health, it needs to become adopted on a much wider scale. HSI devices and applications need to become available at homes and in clinics, and to become part of everyday life. This will allow medical doctors to detect and diagnose diseases in a faster and easier way. Patients will be able to regularly monitor their condition and share test reports with their doctors without the need for repeated visits to the clinic. This can also help extend the reach of medical services to poor and remote areas. On the other hand, consumers will be able to check the safety of their food to make sure it is free of contaminants and allergens and will also be able to assess the nutritional value of their meals in a more efficient way.

Unlocking this potential of HSI for the benefit of public health provides the motivation for the work of this thesis. The way to achieve this is through developing mobile, flexible, and low-cost hyperspectral imaging devices, which can provide fast and reliable results. This development entails a number of technical challenges to improve upon the state-of-the-art of hyperspectral imaging hardware to increase their flexibility and reduce their size form. The work carried out to tackle these challenges is organized as explained the following section.

## 1.3 Thesis Scope & Organization

The thesis starts with an overview of the state-of-the-art of hyperspectral imaging systems in **Chapter 2**. This overview is presented from two perspectives: the data acquisition techniques and the miniaturization. First, the different data acquisition techniques are explained and the state-of-the-art hardware realizations of these techniques are presented. The advantages and limitations of each technique are discussed in light of the public health applications. This discussion is extended to cover the miniaturization of HSI systems and to review the state-of-the-art small-size and low-cost HSI hardware. The chapter concludes with identifying

the technical gaps in the HSI hardware development and miniaturization, focusing on one of the main HSI techniques, namely the spatial-scan technique.

The following chapters present the work carried out in this thesis to address the identified gaps. **Chapter 3** provides the theoretical foundations for this work. First, optical spectroscopy is presented as the broader domain encompassing hyperspectral imaging, providing an understanding of how light-matter interaction leads to the distinctive material spectra. This is followed by explaining diffraction and the diffraction grating, which is a key element in many modern spectroscopic instruments, including the systems introduced in this thesis. After that, the fundamentals of electromagnetic inductive levitation and electrostatic actuation are presented, which together form the working principle of the miniaturization concept introduced in this thesis.

**Chapter 4** presents a novel HSI system concept based on the spatial-scan technique. This concept introduces a new line-scan approach that combines a line-scanning slit and a rotating camera. This provides higher flexibility in data acquisition without sacrificing the spatial nor the spectral resolution. First, the system concept and opto-mechanical construction is presented. This is followed by the spectral calibration of the system and the derivation of the feed-forward compensation function that is used to automate the system. Finally, the experimental work to provide validation of the new system is presented.

**Chapter 5** presents another novel HSI system concept based on the spatial-scan technique. This concept is based on a new rotational-scan approach, providing an alternative to the conventional line-scan methods, by combining a rotating slit and a rotating dove prism. While eliminating one of the main limitations of spatial-scan systems, this concept also provides the blueprint for the miniaturization efforts in this thesis. The system concept and construction is presented, followed by the system calibration and image construction. Finally, the system validation experiments are presented.

**Chapter 6** presents the miniaturization work in this thesis. The aim of this work is to use microfabrication techniques to realize a miniaturized HSI system based on the rotational-scan concept, presented in Chapter 5. This begins with

the miniaturization of the rotating slit mechanism through the development of an improved microfabrication process for double-sided fabrication on a thin glass substrate. The chapter begins by highlighting the state-of-the-art micro-levitation chip and discussing its limitations from the perspectives of optical applications and microfabrication. Afterwards, the design of the new chip is presented and the improved microfabrication process is explained. The chapter concludes with a demonstration of the new chip.

Finally, **Chapter 7** provides a summary of the results obtained in this thesis and an overview of the future work. This includes other novel concepts for hyperspectral analysis and system miniaturization, which have emerged within this research from the collaboration with other institutes at KIT and at Furtwangen University.

# 2 State of the Art

This chapter provides an overview of the state-of-the-art hyperspectral imaging systems. In light of the motivation of this thesis, of enabling HSI for public health applications in everyday life, The state-of-the-art is discussed from two perspectives: the data acquisition techniques and the system miniaturization. Section 2.1 presents the main data acquisition techniques and the notable hardware realizations of each technique. Section 2.2 presents the miniaturization efforts to realize a mobile and low-cost HSI system to facilitate the wide adoption of HSI technology in daily life. Section 2.3 concludes the chapter by highlighting which of the main techniques can provide the optimal candidate for public health applications and by identifying the technical gaps and challenges that will be addressed by the work of this thesis.

## 2.1 Data Acquisition Techniques

Different techniques for the acquisition of hyperspectral data have been developed over the years. The acquisition techniques can be divided into four main categories [33], as explained in the following subsections. Figure 2.1 demonstrates three of these main categories and depicts how the data cube is constructed in each category.

### 2.1.1 Spatial-Scan

The spatial-scan technique is based on sequentially scanning the target image to capture the spectral data for one part of the image at a time, as shown in Figure 2.1(a). One approach, known as the “whiskbroom” [34], uses a pinhole to select

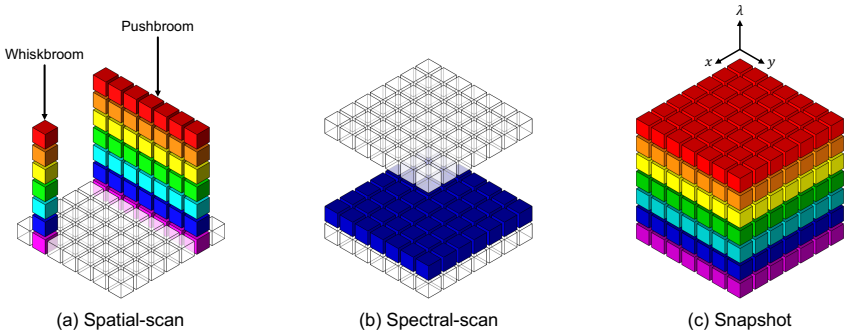


**Figure 2.1:** Three of the main HSI data acquisition techniques. (a) The spatial-scan technique acquires the spectral data for one part of the image at a time, either point-by-point (whiskbroom) or line-by-line (pushbroom). (b) The spectral-scan technique acquires a sequence of 2D images, each at a different waveband. (c) The snapshot technique acquires the spatial and spectral data of the target in a single shot [2].

one point of the image. By passing the light through a dispersive optical element, such as a grating or a prism, the spectrum of the selected point is obtained and recorded with a line detector or a 2D image sensor. To acquire the full hyperspectral data cube, the target image needs to be scanned point-by-point in two dimensions. A faster approach, known as the "pushbroom" [35], uses a slit aperture to select one line of the image. In this case, the target image needs to be scanned line-by-line in only one dimension to acquire the full data cube. Different methods for the spatial scanning of the target are shown in Figure 2.2.

### 2.1.2 Spectral-Scan

The basic principle of the spectral-scan technique is constructing the hyperspectral data cube by combining 2D images of the target, where each image is recorded at a different waveband, as shown in Figure 2.1(b). The sequential variation of wavebands during acquisition can be done either on the detection side or on the target side. On the detection side, this is achieved by projecting the target image through a sequence of bandpass filters. A number of methods were reported in the literature to provide the filters sequence, as demonstrated in Figure 2.3, including

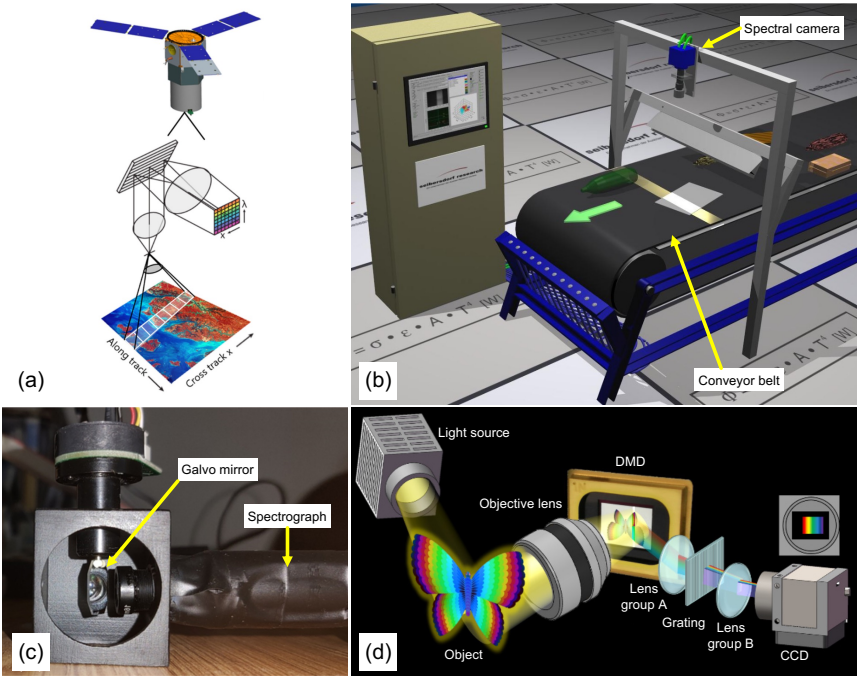


**Figure 2.2:** Pushbroom HSI systems scan the target line-by-line. (a) In remote sensing, the scanning is achieved through the motion of a satellite or a plane (reproduced from [36], licensed under CC BY-NC-ND 4.0). (b) In ground-based systems, conveyor belts are used to introduce relative motion between the system and the target (reproduced from [8] ©2005 SPIE). (c) Scanning mirrors were introduced to scan the target without relative motion (reproduced from [37] ©2012, with permission from Elsevier). (d) New system concepts are emerging to avoid the relative motion by scanning the target internally using a DMD (reproduced from [38] ©2019 Optica Publishing Group).

the use of a circular variable filter (CVF) [39, 40], a linear variable filter (LVF) [41–43], or a tunable filter [44], such as a Fabry-Pérot tunable filter [45, 46], a liquid crystal tunable filter (LCTF) [47], an acousto-optic tunable filter (AOTF) [48], or an active-plasmonic tunable filter (APTF) [49]. On the target side, the sequence is provided by illuminating the target using a source with a different waveband for each image. A common approach for this is the use of an array of narrow-band light emitting diodes (LEDs) [50, 51].


**Figure 2.3:** Different realizations of the spectral-scan technique with different methods for providing the wavebands sequence: (a) Filter wheel (reproduced from [39] ©2008 IEEE). (b) Linear variable filter (reproduced with permission from [42] ©2019 Optical Society of America). (c) Fabry-Pérot tunable filter (cropped from [52] ©2017 SPIE). (d) LED array (adapted with permission from [51] ©2020 American Chemical Society).

### 2.1.3 Time-Scan

In the time-scan technique, a superposition of the spatial and spectral data is acquired. This requires employing mathematical transformations to extract the spectral information from the acquired data. The main example here is Fourier-transform imaging spectrometry, where an interferometer is used to split the incoming light into two beams with an optical path difference (OPD). The two beams are joined back at the detector, which records an interferogram from a number of different OPDs. The Fourier transform is then applied to the interferogram to extract the spectral data. Different methods for introducing the optical path difference were reported including the use of a Michelson interferometer with a

beam splitter, a fixed mirror, and a moving mirror [53] and the use of birefringent blocks [54, 55]

### 2.1.4 Snapshot

The snapshot technique enables the acquisition of the spatial and spectral information of the target in a single shot (Figure 2.1(c)), which allows for video-rate spectral imaging. One of the main approaches reported in the literature to realize this combines image duplication and a form of on-chip filter array, as shown in Figure 2.4(a). The image duplication is achieved using a microlens array (MLA), which projects smaller duplicates of the target image on the detector. The filter array consists of a number of elements, each corresponding to a unique spectral band. By placing the filter array directly on top of the image sensor, the sensor area is divided into a corresponding number of distinct spectral channels. By projecting each duplicate image through one element of the filter array, a set of 2D images of the target, each at a different spectral band, is recorded in a single shot. By stacking the images together, the data cube can be constructed.

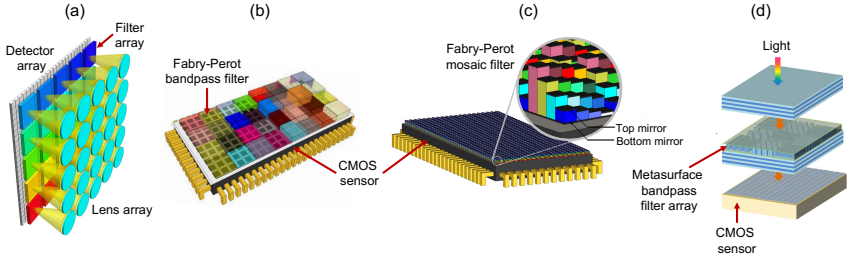


**Figure 2.4:** Snapshot spectral imaging based on image duplication and on-chip filter arrays. (a) A lens array duplicates the target image and projects each duplicate through a different channel of the filter array (reproduced from [56], licensed under CC BY 4.0). Different types of filter arrays include: (b) Fabry-Pérot tiled filters (adapted from [57] ©2014 IEEE), (c) Fabry-Pérot per-pixel mosaic filters (adapted from [58] ©2014 SPIE), and (d) Metasurface filter array (adapted from [59], licensed under CC BY 4.0).

Different methods were reported for the realization of the filter array, some of which are demonstrated in Figure 2.4(b-d). A tiled filter array based on Fabry-Pérot

interferometers, directly deposited on the CMOS sensor, is reported by IMEC, Belgium [60, 61]. Another variation is the deposition of the filter elements in a per-pixel mosaic arrangement that extends the traditional Bayer RGB matrix to multispectral or hyperspectral imaging [58, 62]. Another – more recent – method for the realization of the filter elements involves the use of metasurfaces [59, 63]. Other than the filter array, snapshot spectral imaging was also demonstrated using a microspectrometer array [64] and using a slanted linear variable filter in a multi-aperture system [65]. A more comprehensive overview of the different snapshot approaches is provided in the review paper of Hagen and Kudenov [56].

While the previous four subsections cover the main categories of hyperspectral data acquisition, it is worth mentioning that there are other different techniques which include hybrid and computational techniques. The spatio-spectral scanning technique is an example of a hybrid between the spatial-scan and the spectral-scan techniques which records the data cube in diagonal, rather than orthogonal, slices [66]. Computational techniques estimate and construct the data cube numerically instead of measuring every voxel of the cube optically. One of the early methods is computed tomography imaging spectrometry (CTIS) [67, 68] which uses a grating to simultaneously record parallel 2D projections of the data cube in different directions on the detector array. The recorded projections are then used to numerically construct the data cube using an algorithm of computed tomography. The coded aperture snapshot spectral imager (CASSI) is another computational method which uses a coded aperture together with a dispersive element to record a coded 2D projection of the data cube that contains a mixture of spatial and spectral information [69–71]. A numerical estimation algorithm is then used to construct the data cube. However these methods typically require more complex hardware setups, higher computational power, and longer post-processing times for data cube construction.

## 2.2 Miniaturization

The adoption of hyperspectral imaging on a wide scale in everyday life requires small-size, mobile, and low-cost devices. This is not the case in conventional systems which are bulky, costly, and complex, which limited their use to industrial and research applications. An example for such systems is the FX10 spectral camera from Specim Ltd., which is shown in Figure 2.6(a). The FX10 operates in the VNIR range between 400 – 1000 nm, and has a size of 150 mm × 85 mm × 71 mm, a mass of 1.3 kg, and a price tag in the range of €10,000 [72]. In recent years, there have been continuous efforts to develop miniaturized spectral imaging systems that can either be used as standalone handheld devices or be integrated into other systems such as medical devices, home appliances, and smartphones. This will open the door for HSI technology to serve public health applications for patients and doctors in clinics and hospitals, as well as for consumers in homes and shops.

Most of the miniaturization efforts have focused on spectral-scan and snapshot techniques, while less progress was reported for the miniaturization of spatial-scan and time-scan techniques. This can be explained with the high compatibility of key components in spectral-scan and snapshot techniques, namely tunable filters and filter arrays, with microfabrication.

In the spectral-scan technique, the Fabry-Pérot tunable filter has emerged as a key component to enable compact and miniaturized systems. This is because its relatively simple structure, which consists of two parallel mirrors enclosing an interference cavity, is well-suited for microfabrication, as shown in Figure 2.3(c). The high precision actuation to control the cavity size, required for spectral tuning, is another motivation for microfabrication, where different actuation mechanisms can be used including magnetic [73], electrothermal [74], piezoelectric [75], and electrostatic actuation [76–79]. The miniaturized Fabry-Pérot tunable filter has been utilized to develop handheld systems [80–82] and to enable spectral imaging in a smartphone through an external cover [52, 83], which are shown in

Figure 2.5(a) and (b). Table 2.1 summarizes the reported spectral ranges, spectral resolutions, and actuation mechanisms of these devices.

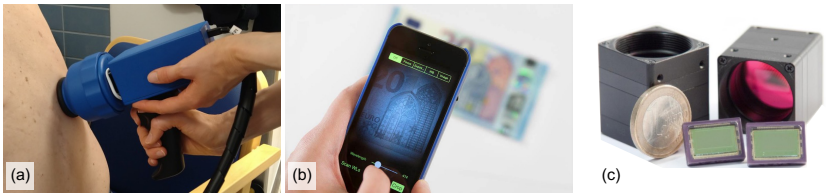


**Figure 2.5:** Miniaturization of spectral imaging systems has mostly focused on spectral-scan and snapshot techniques. A Fabry-Pérot tunable filter chip was used to enable: (a) handheld device for medical applications (cropped from [80], licensed under CC BY 4.0) and (b) spectral tuning in a smartphone cover for mobile applications (reproduced from [52] ©2017 SPIE). (c) The on-chip mosaic filters are used to enable small-size snapshot cameras (adapted from [84] ©2015 SPIE).

In the snapshot technique, the integration of thin filter arrays directly on the image sensor has been the key for enabling a number of compact and small-size systems, as discussed in Section 2.1.4. Demonstrations include the compact multispectral cameras based on the monolithic deposition of Fabry-Pérot interference filters on the CMOS sensor [60, 61]. Figure 2.5(c) shows a small-size multispectral camera which is based on the mosaic filter array of IMEC, Belgium [84]. Table 2.2 provides an overview of the main characteristics of notable state-of-the-art compact snapshot cameras.

**Table 2.1:** Compact spectral-scan devices based on the miniaturized Fabry-Pérot tunable filter and their main characteristics

| Ref. | Type | Spectral range | Spectral resolution | Actuation |
|---|---|---|---|---|
| [80] | Handheld | 475 – 975 nm | 8 – 18 nm | Piezoelectric |
| [81] | Handheld | 430 – 580 nm | 20 nm | Electrostatic |
| [82] | Handheld | 500 – 885 nm | 9 – 40 nm | Piezoelectric |
| [83] | Smartphone | 450 – 550 nm | 8 – 15 nm | Electrostatic |

When it comes to the miniaturization of the spatial-scan technique, less progress has been reported. Stuart et al. presented a low-cost pushbroom device based on

**Table 2.2:** Compact snapshot devices and their main characteristics

| Ref. | Type | Spectral range | Spectral bands |
|---|---|---|---|
| [60] | Tiled Fabry-Pérot filter array | 600 – 1000 nm | 32 |
| [61] | Mosaic Fabry-Pérot filter array | 1100 – 1650 nm | 9 |
| [84] | Mosaic Fabry-Pérot filter array | 600 – 900 nm | 25 |
| [59] | Tiled metasurface filter array | 700 – 950 nm | 20 |
| [65] | Slanted linear variable filter | 450 – 850 nm | 66 |

converting a standard smartphone into an HSI sensor [85]. A 3D-printed housing encloses a transmission diffraction grating and has an entrance slit with 500 µm width. The housing is attached to a Samsung Galaxy A12. The attachment can be adjusted to fit a wide range of smartphones. The phone is mounted on a linear stage with a stepper motor to scan the device against the target for data acquisition. The video mode of the smartphone camera is used to record data in the visible range between 400 – 700 nm with a spectral resolution of 14 nm (FWHM). Figure 2.6(b) shows the smartphone with the attached housing mounted on the linear stage.

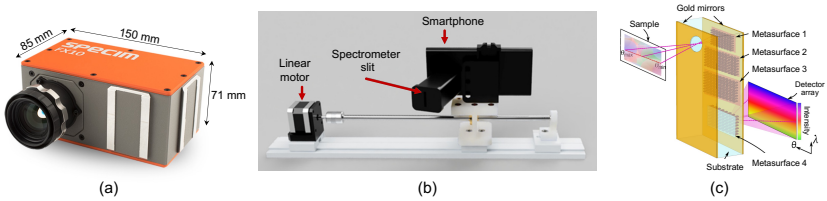


**Figure 2.6:** (a) FX10 VNIR pushbroom hyperspectral camera from Specim Ltd is an example of conventional HSI systems used in industry and research (reproduced from [72]). (b) A portable small-size smartphone-based pushbroom system (adapted from [85], licensed under CC BY 4.0). (c) A folded-metasurface line-scanning hyperspectral imager (reproduced from [86] ©2019 American Chemical Society).

Another advancement towards the miniaturization of spatial-scan devices is based on metasurfaces, which are ultra-thin and planar materials that can be designed to control the amplitude, phase, and polarization of light on a subwavelength level.

Faraji-Dana et al. demonstrated a line-scanning HSI imager that is 1 mm thick with a total volume of 8.5 $mm^3$ based on a folded metasurface structure consisting of four metasurfaces, three reflective and one transmissive [86]. A schematic of the folded metasurface pushbroom imager is shown in Figure 2.6(c). The first reflective metasurface acts as blazed grating and disperses the incoming light. The other three metasurfaces together focus the light and project it on the detector plane, which is designed to be 1 mm parallel to the substrate. The metasurfaces consist of $\alpha$-Si nanoposts resting on a fused silica substrate covered with 2 µm SU-8, which is covered with a gold layer to make the metasurfaces reflective. The spectral range is between 750 – 850 nm and the reported spectral resolution is 1.4 nm. Zhao et al. reported a similar structure but with only two metasurfaces and a spectral range between 850 – 1000 nm [87].

## 2.3 Conclusions

### 2.3.1 Candidate for Public Health

Choosing a single technique to be used universally for public health applications in everyday life is a challenging task. The choice of the preferred technique is highly dependent on the requirements of each specific application, including the data acquisition and data processing speed, and the spatial and spectral resolution. When it comes to public health applications, the most important trait of the preferred technique is to provide highly reliable data to avoid the risks of false diagnoses and misleading information to the users. This translates into high spatial and spectral resolutions for analyzing the smallest features and traces relevant to the user's health. Other desirable traits include high adaptability to a wide range of application scenarios and a reasonable speed of data acquisition and processing.

In this thesis, the spatial-scan technique is proposed as the preferred candidate for public health applications. The main argument for this preference is that it is feasible to acquire data with high spatial and spectral resolution over a broad and continuous spectral range, solely by proper optical design and selection of system components. This allows the spatial-scan technique to meet the main criteria for

public health applications. In contrast, it is harder to achieve such performance with the other techniques due to the accompanying challenges and limitations on the hardware side.

The spectral-scan technique suffers from low optical throughput due to the reliance on bandpass filters. In addition, it provides the spectral data at a limited number of discrete wavelengths. Increasing the number of spectral bands requires using a high number of filters. While this is difficult with circular variable filters (CVF), which are usually limited to a few bands, it is feasible with linear variable filters (LVF), however at the cost of lower spectral resolution, due to the sensitivity of the filter elements to the incidence angle of the incoming light, and the need to spatially scan the target against the linear filter. Using a tunable filter to scan across a high number of spectral bands requires high tuning precision over a wide tuning range. In the visible range (400 – 700 nm), as an example, this means controlling the cavity size of the Fabry-Pérot interferometer in the range between 140 – 390 nm, depending on the optical properties of the interferometer mirrors [88, 89]. However, different actuation mechanisms suffer from different limitations. The magnetic actuation requires an external magnet, which increases the system size. The electrothermal approach requires heating and cooling and consequently suffers from slow tuning. The piezoelectric actuation suffers from hysteresis effect and requires a feedback mechanism. Finally, the electrostatic actuation, which is used more often in this context due to its fast response, suffers from the pull-in effect, which limits the actuator's maximum displacement to one-third of the cavity size, thereby restricting the wavelength tuning to only two-thirds of the full range.

The time-scan technique can achieve high spectral resolution over a continuous wide range. However, the need to split the incoming light into two beams with a phase difference in between usually translates into more complex hardware with high precision moving parts to acquire interferograms over a wide range of optical path differences (OPDs). In the Michelson interferometer, as an example, the moving mirror needs to be controlled with a precision better than $\lambda/20$ [54]. This is a precision of 20 nm for blue light, which is difficult to achieve without mounting

the system on a damping platform. In addition to the hardware challenges, there is an additional computational cost to transform the acquired interferogram into spectral data.

The snapshot technique, while it offers the advantage of real-time acquisition or video-rate spectral imaging, it sacrifices both spatial and spectral resolution because the area of the image sensor is divided into a limited number of spectral channels. In addition, the static nature of the on-chip filter arrays limits the adaptability and flexibility in different application scenarios because switching to a different spectral range would require replacing the entire CMOS image sensor with all the integrated filers. Based on the discussion above, the spatial-scan technique is chosen as the best-suited technique for public health applications.

### 2.3.2 Technical Gaps

The current state-of-the-art spatial-scan systems, however, suffer from a number of drawbacks that limit the range of applications they can serve. The main drawback is the need for relative motion to scan the target and the imaging system against each other during data acquisition. This dependency on relative motion goes back to the early development of the spectral imaging technology by NASA in the mid 1980's for remote sensing applications [4]. Imaging spectrometers – also known as spectrographs – were mounted on satellites and airplanes to scan the surface of the earth, as shown in Figure 2.2(a), and collect data about vegetation, forests, oceans, and mineral resources. In this context, the relative motion is inherently part of the application scenario and doest not represent a drawback. The reliance on the scanning relative motion continued as the technology was introduced in ground-based systems. Motorized stages and conveyor belts (Figure2.2(b)) were used to introduce the relative motion and scan either the target or the imaging system against the other [90]. However, in many scenarios, especially in the public health domain, this relative motion is not practical or not even feasible. For example, in endoscopy, it would be highly challenging to introduce such motion inside a patient's body during examination. Yoon et al. proposed to achieve this using

freehand movement with a hyperspectral endoscopy system [91]. However, this required additional equipment to co-register the wide-field image and additional time for data processing to remove the artifacts caused by the freehand motion. Another public health example where the relative motion is highly impractical is when consumers need to check their food against contaminants or allergens. In such case, the relative motion can be introduced either by freehand motion, which will complicate the data processing, or using a motorized scanner, which will complicate the hardware requirements. Such examples highlight the need for getting rid of the relative motion altogether.

Another drawback of the current spatial-scan systems is the limited flexibility in adapting to the application requirements in terms of data acquisition parameters, such as changing the acquisition speed or reducing the size of the acquired dataset by choosing a specific region of interest. The lack of direct access to the spatial imaging view of the target in conventional spectrographs can also be considered a drawback that limits the flexibility of the systems and their adaptability to changes in the target scene. The common root of these drawbacks is that conventional spectrographs were constructed from static passive components. With the absence of any active system component, the reliance on relative motion continued and the flexibility and adaptability of the systems remained limited.

Over the past years, a number of pushbroom HSI systems were reported to mitigate the need for relative motion. The common concept behind these systems is using active system components to scan a projected image of the target rather than directly scanning the target itself. In some systems, a planar mirror is mounted on a high-resolution motor and is used to scan a reflection of the target image against an imaging spectrograph [37, 92, 93], as shown in Figure 2.2(c). Other systems used linear actuators to move the front optics and the spectrograph against each other [94, 95] to scan the projection of the target image at the focal plane of the front optics across the entrance slit. By including active components in these systems, the spatial scanning was achieved without the need to move the target nor the imaging system. While the relative motion requirement is removed, the common aspect among these systems is what can be described as

an “outside approach”, where external hardware components are added around a conventional spectrograph that is left as a black box, with all its conventional passive components, which increases the hardware complexity and cost.

Recent years have seen the emergence of a new contrasting paradigm that can be described as an “inside approach”. This approach tries to re-think the design and the construction of the conventional spectrograph and introduce new system concepts to scan the target image using active internal components, with the goal of developing more flexible and compact systems. This can be seen in a new system concept, which is based on a digital micromirror device (DMD) [38, 96], as shown in Figure 2.2(d). The DMD is used to simulate the function of a scanning slit. When actuating one row of micromirrors, they tilt to reflect the light from one line of the image into the monochrome sensor, through a transmission grating, to record the spectral data for that line. By sequentially switching from one row of micromirrors to the next, the spatial scanning of the target is performed internally and the spectral data is acquired in a line-by-line fashion similar to the pushbroom approach.

This new design of a pushbroom system, utilizing the DMD as an active internal component, has mitigated the drawbacks of the relative motion while offering higher flexibility in controlling the acquisition parameters. For example, the system resolution can be adapted by controlling how many micromirror rows are used simultaneously to capture the data of one line. This would be similar to changing the slit width in a spectrograph. The acquisition speed can be changed by changing the rate of actuating the micromirror rows. In addition, the DMD can be used to acquire a smaller set of data from a specific region of interest to reduce the data processing load.

There are, however, some drawbacks to this approach. The most significant of which is that each row of micromirrors of the DMD will reflect the light to the grating at a different angle. This results in a different position of the spectrum on the image sensor for each row, due to the change in the incidence angle of the reflected light on the grating. This can undermine the spectral calibration of the system. This can also compromise the system resolution because it is not possible

to use the full sensor area due to the continuous lateral shifting of the spectrum. Another drawback is the information loss due to the pixel-wise arrangement of the DMD micromirrors, which typically has a fill factor around 92% [97, 98]. Xiao et al. managed to increase the fill factor by replacing the DMD with an array of linear micromirrors [99]. The discussion above highlights two main technical gaps in the development of spatial-scan HSI systems. The first gap is the need for new system concepts and designs with high flexibility and adaptability that can acquire the data cube without relative motion and while avoiding the other drawbacks mentioned above. The second technical gap was highlighted in Section 2.2, which is the limited progress in the miniaturization of spatial-scan systems. Despite the promising results reported for the smartphone-based system [85] and the metasurface-based concepts [86, 87], they all still require relative motion to scan the target. Therefore, there is still a need to develop a miniaturized spatial-scan system that can achieve high resolution acquisition of the data cube without relative motion.

The work of this thesis aims to address these technical gaps through the development of new systems concepts (Chapters 4 and 5) and the miniaturization (Chapter 6) of spatial-scan HSI systems.

# 3 Theoretical Foundations

This chapter lays the theoretical foundation for the work undertaken in this thesis. It provides context and explains the principles underlying the system development and miniaturization presented in the following chapters.

Section 3.1 begins with optical spectroscopy as the broad domain to which spectral imaging belongs. The principles of light-matter interaction, which form the backbone of spectral analysis, are explained within a concise historical overview. This provides an understanding of how the material composition is linked to distinctive spectra, while situating the spectral imaging technology within the centuries-long advancements in the field.

Section 3.2 focuses on diffraction, as an optical phenomenon that plays an essential role in spectroscopy, and especially in spatial-scan HSI systems. The section explains diffraction by tracing back its first recorded observations and the evolution of our understanding of its phenomena, as part of our understanding of the nature of light. The section concludes with presenting the diffraction grating as the most established and widely used diffractive element in spectroscopic instruments, including the systems introduced in Chapters 4 and 5. This discussion explains the working principle of the grating and its governing equations.

Sections 3.3 and 3.4 delve into the underlying physics of electromagnetic inductive levitation and electrostatic actuation, respectively. Together they provide the foundation for understanding the working principle of the micromachined levitating and rotating slit device presented in Chapter 6, which is proposed as the starting point for the overall miniaturization of the rotational-scan HSI concept.

## 3.1 Optical Spectroscopy

Optical spectroscopy is a scientific analytical technique based on the interaction of light with matter to study its composition, structure, and properties. This interaction can take different forms including absorption, reflection, scattering, or emission based on the type of material and the interacting light wavelength. Light, in this context, refers to the electromagnetic radiation covering the range from ultraviolet (UV) to infrared (IR). Spectroscopy has become an essential tool for chemical analysis due to its non-destructive nature and the precise and versatile information it can provide on a wide range of samples including solids, liquids, and gases and from microscopic to celestial objects. That is why spectroscopy is widely used today in many scientific and industrial fields including chemistry, biology, astrophysics, pharmaceuticals, medical diagnostics, and mining [100].

Spectroscopy has its roots back in the 17th century when Isaac Newton used a glass prism to disperse sunlight into its spectral constituents for the first time [100], similar to Figure 3.1(Left). His work laid the foundation for understanding light as a composition of different spectra that can be separated from each other and introduced the term "*spectrum*" in the scientific sense used today. In the early 19th century, William Wollaston built upon Newton's prism experiments and made the first observations of dark lines in the solar spectrum [100, 101]. In the same period, Josef von Fraunhofer made his significant contributions to the field. He is credited with the development of the diffraction grating into a high-quality powerful tool for the dispersion of light, which is still in use today in modern spectroscopic equipment. He used the grating in his meticulous study of the solar spectrum and cataloged the dark lines, which are known today as Fraunhofer lines [100, 101]. Those lines, which can be seen in Figure 3.1(Right), are attributed to the absorption of specific wavelengths by elements present in the atmosphere. In the mid-19th century, Gustav Kirchhoff and Robert Bunsen together managed to link specific chemical elements to their characteristic spectral lines, establishing spectroscopy as a tool for chemical analysis [100, 101].

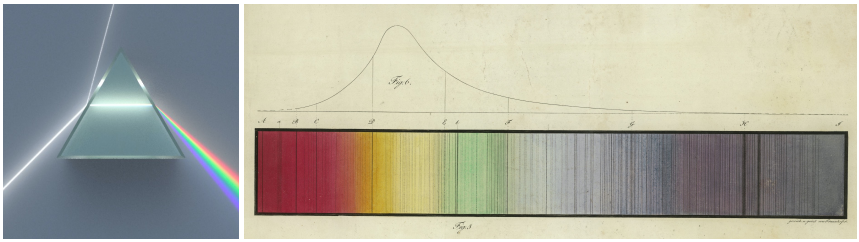

**Figure 3.1:** (Left) A beam of white light is reflected, refracted, and dispersed into its spectra upon hitting a dispersive prism (cropped from [102], licensed under CC BY-SA 3.0). (Right) An image of the copper etching made by Fraunhofer himself, depicting the full visible spectrum with the Fraunhofer lines, where some of them are marked with letters. Above the spectrum is the eye's spectral response to daylight which was also measured by Fraunhofer. Archive BN 43952 at the Deutsches Museum (reproduced from [103], licensed under CC BY-SA 4.0).

The understanding of this link and why certain atoms interact with certain wavelengths of light evolved with the development of the quantum theory in the 20th century. The birth of this theory is often attributed to Max Planck who proposed that energy is quantized and can be absorbed or emitted in discrete units called "*quanta*" [100, 101]. Albert Einstein extended the quantum theory, through his explanation of the photoelectric effect, by proposing that light itself can be considered as consisting of discrete packets of energy, that later became known as "*photons*" [101, 104]. Later on, Niels Bohr adopted the quantum theory when he presented his model for the hydrogen atom, in which he proposed that electrons orbit the nucleus in discrete energy levels and that electrons can transition between these levels by absorbing or emitting energy in discrete quanta (photons) [101, 105]. With each element having a unique electronic structure, with a unique set of energy levels, the wavelengths of photons absorbed or emitted for electron transitions is specific to each element, leading to characteristic spectral lines for each element. The discovery of this link has deepened our understanding of atomic and molecular structures and formed the backbone of modern spectroscopy.

While spectroscopy became a widely adopted analytical tool, it was limited to point measurements without spatial context. Obtaining spatially resolved information of the chemical composition required repeating the measurement at different

points in the sample. This was the case until spectral imaging became feasible with the advent of digital sensors and the progress in computing in the late 20th century. The development of the charge-coupled device (CCD) and the complementary metal-oxide-semiconductor (CMOS) sensors enabled the recording of high-resolution data on 2-dimensional pixel arrays and marked the beginning of digital imaging. The exponential growth in computing power, accelerated by the invention of the microprocessor, enabled the processing of large multi-dimensional datasets typically acquired by spectral imaging. The continuous and fast-paced development of data analysis algorithms, powered by machine learning and artificial intelligence, is poised to unlock even more applications of spectral imaging and achieve higher levels of precision and accuracy.

## 3.2 Diffraction

Diffraction is a phenomenon observed when waves, such as light, encounter an obstacle or a narrow opening that alters the further propagation of the waves in terms of amplitude or phase. This is explained with the help of the Huygens-Fresnel principle which describes wave propagation by considering each point on a wavefront as a point source of spherical wavelets and that the sum of these secondary wavelets determines the shape of the wavefront at the following instant in time. Wavelets emanating from the edges of an obstacle or through an aperture interfere and form a new wavefront that is observed as bending around the obstacle or spreading out from the aperture. This interference of wavelets is what leads to the bright and dark patterns referred to as the diffraction pattern, where bright areas correspond to constructive interference and dark areas to destructive interference [101, 105].

Diffraction has been the subject of study for centuries, as theories and understanding of the nature of light evolved. The first recorded use of the term "*diffraction*" in the scientific sense used today is attributed to Francesco Maria Grimaldi in the 17th century [106]. Grimaldi, in his experiments, observed that a cone of light passing through two narrow apertures produced a spot much larger

than predicted by the principle of rectilinear propagation of light, implying wave-like properties of light. This posed a contradiction to Newton's "*corpuscular theory*", which explained light as composed of tiny particles, or "*corpuscles*", that travel in straight lines. Another contradiction in that period came from Christiaan Huygens, who proposed the "*wave theory*" of light and formulated his principle of secondary wavelets to explain diffraction. However, Newton's corpuscular theory remained the prevailing theory until the early 19th century when Thomas Young conducted his renowned double-slit experiment. Young explained the pattern of alternating bright and dark fringes observed on a screen after light passes though two closely spaced narrow apertures in terms of diffraction and interference, thus providing compelling evidence for the wave theory of light. Contemporary to Young, Augustin Fresnel developed the mathematical framework to accurately describe diffraction patterns, specifically near-field diffraction – also known as "*Fresnel diffraction*" – where the light source, the observation screen, or both are at a distance from the aperture that is comparable to or smaller than the wavelength of light. Another prominent contemporary of that period was Joseph von Fraunhofer, who refined and improved the diffraction grating[1] and conducted extensive experiments documenting the diffraction patterns in the far-field, where the source and the screen are at large distances from the aperture – also known as "*Fraunhofer diffraction*" [101, 105].

The diffraction grating is considered the most established and most used dispersive element. A diffraction grating typically consists of a large number of closely and equally spaced slits or grooves that are etched on the surface of a reflective or transparent substrate. Each slit or groove acts as a source of secondary wavelets, when a beam of light encounters the grating. The wavelets emanating and spreading out from each slit or groove interfere with each other constructively and destructively at different angles. Constructive interference takes place when the path difference between wavelets from adjacent slits or grooves is an integer multiple of the wavelength, resulting in interference maxima at specific angles

[1] The invention of the diffraction grating is attributed to David Rittenhouse in 1785.

known as diffraction orders. The angles of the diffraction orders are determined by the grating equation [101, 105]:

$$\Lambda \sin\theta_m - \Lambda \sin\theta_i = m\lambda \tag{3.1}$$

where $\Lambda$ is the grating period, $\lambda$ is the wavelength of light, $\theta_i$ and $\theta_m$ are the angles of incidence and diffraction respectively[2], and $(m = \pm 1, \pm 2, \pm 3, \dots)$ is the diffraction order, as illustrated in Figure 3.2. Diffraction orders found on the same side, relative to the zero order, as the grating normal are considered positive.

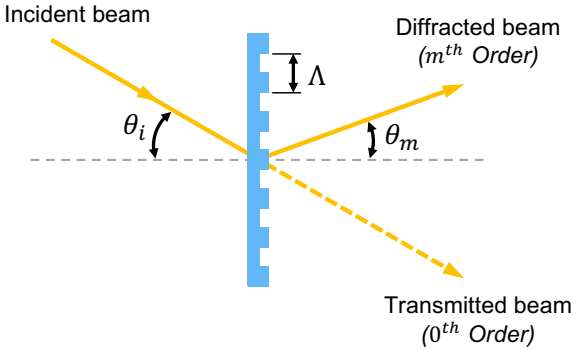


**Figure 3.2:** Illustration of a transmission grating with a corrugation of period $\Lambda$. The incident beam has an angle $\theta_i$, with respect to the substrate normal, and is diffracted at an angle $\theta_m$, where $m$ corresponds to the diffraction order. The transmitted beam, corresponding to the $0^{th}$ order, emerges at the incidence angle $\theta_i$. (Refraction has been ignored in this depiction.)

The optical performance of a diffraction grating is characterized by several parameters. Dispersion $(\mathscr{D})$ measures the ability of a grating to disperse an incoming beam into its spectral components and is defined as the variation of the diffraction angle $\theta_m$ with wavelength $\lambda$, as expressed by [105]:

$$\mathscr{D} = \frac{d\theta_m}{d\lambda} = \frac{m}{\Lambda \cos\theta_m} \tag{3.2}$$

[2] Using the convention that angles in the first and third quadrants are positive and angles in the second and fourth quadrants are negative [101].

This indicates higher dispersion for higher diffraction orders. However, since higher orders typically have lower efficiency, higher dispersion is usually achieved in practice by decreasing the grating period $\Lambda$. The free spectral range (FSR) defines the wavelength interval over which the wavelengths from adjacent orders of diffraction do not overlap. For diffraction order $m$, this is given by [105]:

$$\Delta\lambda_{FSR} = \frac{\lambda_{long}}{|m|+1} \tag{3.3}$$

where $\lambda_{long}$ is the longest wavelength in the wavelength range of interest. The chromatic resolving power ($\mathscr{R}$) is a measure of a grating's ability to separate two closely spaced spectral lines and determines the smallest difference in wavelength $(\Delta\lambda)_{min}$, that can be resolved by the grating. This is expressed by [105]:

$$\mathscr{R} = \frac{\lambda}{(\Delta\lambda)_{min}} = mN_G \tag{3.4}$$

where $N_G$ is the total number of slits or grooves illuminated by the incident light.

## 3.3 Electromagnetic Inductive Levitation

Levitation refers to the free floating of an object without physical attachment to its surroundings. This phenomenon has attracted the attention of researchers in microelectromechanical systems (MEMS) as a way to overcome the dominance of friction in the micro-scale, which decreases the output torque in micromotors, limits the rotation speed and motion range in micro-rotors and microactuators, and causes mechanical wear, which eventually leads to device failure. Levitation can be used to achieve frictionless motion in microsystems leading to improved performance and long device lifetime, which would benefit the development of a wide range of applications in areas such as inertial sensors, micro-bearings, and micro-transporters, micromanipulation, and micro-positioning systems [107].

In this thesis, levitation is used to enable a miniaturized frictionless rotating slit. The rotating slit is a key element in the new rotational-scan concept presented in

Chapter 5. The miniaturization of this new system starts with the miniaturization of the rotating slit, which is presented in Chapter 6.

Among the methods developed for levitation in the micro-scale, electromagnetic inductive levitation stands out as the most promising candidate. This is because it can be used to achieve stable passive levitation, without dependance on feedback control or any external medium. Another advantage is the high compatibility with microfabrication techniques compared to other magnetic-based methods which rely on permanent magnets and superconducting materials [107].

The working principle of the electromagnetic inductive levitation is depicted in Figure 3.3, which shows two coaxial ring-shaped coils with a levitating disc-shaped proof mass (PM) on top. The inner coil is used for levitation, while the outer coil is used for stabilization of the proof mass, which is made of a conductive non-magnetic material. An alternating current (AC) applied to the inner coil generates a time-variable magnetic flux in space. The variable magnetic flux induces eddy currents when it intercepts the surface of the proof mass. The eddy currents generate an opposing magnetic flux to that of the inner coil and creates a repulsive force that causes the disc to levitate. This force is the vertical component of the Lorentz force [107, 108].

When the axis of the proof mass exactly coincides with the axis of the levitation coil, in the absence of the outer coil, there is no resultant force in the lateral direction. This is because the radial Lorentz force is distributed in the proof mass in axis-symmetrical way that counteracts to zero. However, this is rarely the case, and therefore any tiny displacement of the proof mass results in a non-zero lateral runaway force that pushes the proof mass out of equilibrium and away from the stable levitation position. This is where the outer stabilization coil comes into action. By applying an AC signal with 180° phase-shift with respect to the levitation coil, the resultant lateral Lorentz force acts as a restoring force that brings the proof mass back to the center position, which becomes the stable equilibrium position [107–109].

In order to understand levitation in mathematical terms, the Lorentz force acting on the proof mass needs to be analyzed. The Lorentz force, which is experienced

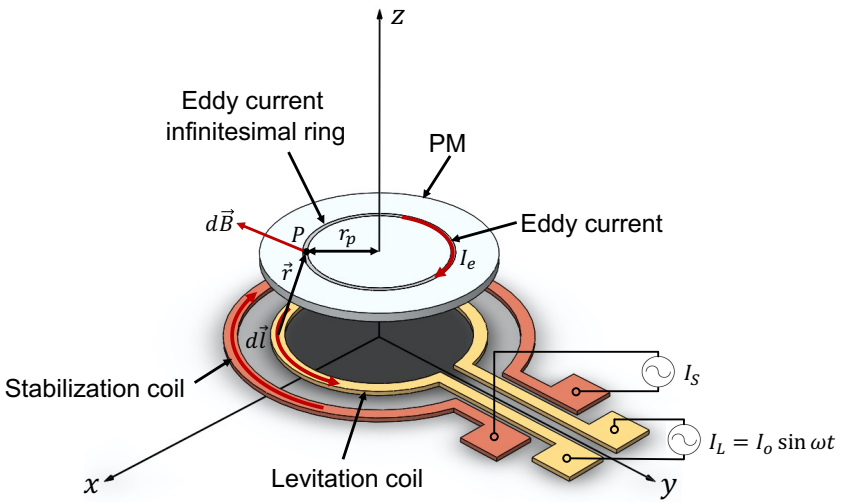


**Figure 3.3:** Working principle of electromagnetic inductive levitation. The AC current of the levitation coil generates a time-variable magnetic field which induces eddy currents in the proof mass. The induced eddy currents generate a counteracting magnetic field causing the PM to levitate [107, 108, 110].

by a charged particle moving in an electromagnetic field, is generally given by the equation [111]:

$$\vec{F}_L = q(\vec{E} + \vec{v} \times \vec{B}) \tag{3.5}$$

where $q$ is the charge of the particle, $\vec{E}$ is the electric field, $\vec{v}$ is the velocity of the particle, and $\vec{B}$ is the magnetic flux density. In the case of the two-coil structure, shown in Figure 3.3, the Lorentz force is mainly due to the magnetic flux which induces the eddy currents in the proof mass. Expressing the Lorentz force, therefore, requires defining the magnetic flux $\Phi$ generated by the levitation coil and the induced eddy current. Consider an infinitesimal ring with radius $r_p$ within the proof mass, where $P$ is an arbitrary point in the ring, as depicted in Figure 3.3. When the levitation coil is activated with an AC current $I_o \sin \omega t$, a time-varying magnetic field is generated in space, and the magnetic flux density

$\mathrm{d}\vec{B}$ at point $P$, due to the infinitesimal current element $\mathrm{d}\vec{l}$ of the coil, is given by the Biot-Savart law [111, 112]:

$$\mathrm{d}\vec{B} = \frac{\mu_o}{4\pi} \frac{I_o \sin \omega t \, \mathrm{d}\vec{l} \times \vec{r}}{|\vec{r}|^3} \tag{3.6}$$

where $\mu_o$ is the vacuum permeability, $I_o$ is the amplitude of input current, $\omega$ is the angular frequency of input current, and $\vec{r}$ is a position vector of the point $P$ with respect to $\mathrm{d}\vec{l}$. The magnetic flux density at point $P$, due to the entire current loop $lc$ of the coil, is then found by integrating Eq.(3.6) over $lc$:

$$\vec{B} = \frac{\mu_o I_o \sin \omega t}{4\pi} \oint_{lc} \frac{\mathrm{d}\vec{l} \times \vec{r}}{|\vec{r}|^3} \tag{3.7}$$

and the total magnetic flux $\Phi$ passing through the surface area $S$ of the infinitesimal ring in the proof mass is given by [111]:

$$\Phi = \int_S \vec{B} \cdot \mathrm{d}\vec{A} \tag{3.8}$$

where $\mathrm{d}\vec{A}$ is an area element of $S$. Based on Faraday's law of inductance, the electromotive force in the infinitesimal ring is given by [111]:

$$\xi = -\frac{\mathrm{d}\Phi}{\mathrm{d}t} \tag{3.9}$$

Consequently the eddy current induced in the infinitesimal ring is given by:

$$I_e = \frac{\xi}{Z_{ring}} \tag{3.10}$$

where $Z_{ring} \approx R_{ring} + j\omega L_{ring}$ is the impedance of the infinitesimal ring, where $R_{ring}$ is the resistance and $L_{ring}$ is the inductance of the infinitesimal ring, and the approximation is based on assuming the frequency is not significantly high and

ignoring the intrinsic capacitance of the infinitesimal ring. Combining equations 3.7 and 3.9, the induced eddy current becomes:

$$I_e = -\frac{\mathrm{d}\Phi}{Z_{ring}\,\mathrm{d}t} = -\frac{\mu_o \omega I_o \cos\omega t}{4\pi Z_{ring}} \int_S \oint_{lc} \frac{\mathrm{d}\vec{l}\times\vec{r}}{|\vec{r}|^3} \cdot \mathrm{d}\vec{A} \tag{3.11}$$

In order to express the Lorentz force acting on the eddy current infinitesimal ring in the proof mass, a slightly different form of Eq.(3.5) is used:

$$\vec{F_L} = \oint_{l_p} I_e \left(\mathrm{d}\vec{l'} \times \vec{B}\right) \tag{3.12}$$

where $\mathrm{d}\vec{l'}$ is a differential element along the path of the eddy current in the infinitesimal ring $l_p$. By substituting Eq.(3.7) and (3.11) into Eq.(3.12), the Lorentz force acting on the eddy current infinitesimal ring becomes:

$$\vec{F_L} = \oint_{l_p} \left( -\frac{\mu_o \omega I_o \cos\omega t}{4\pi Z_{ring}} \int_S \oint_{lc} \frac{\mathrm{d}\vec{l}\times\vec{r}}{|\vec{r}|^3} \cdot \mathrm{d}\vec{A} \left( \mathrm{d}\vec{l'} \times \frac{\mu_o I_o \sin\omega t}{4\pi} \oint_{lc} \frac{\mathrm{d}\vec{l}\times\vec{r}}{|\vec{r}|^3} \right) \right) \tag{3.13}$$

As explained above, the Lorentz force has a vertical component and a radial component. The vertical component provides the levitation while the radial component affects the stability of the levitated proof mass. This radial component would turn into an escape force that will push the proof mass to fall in case of any perturbation due to environmental disturbances or geometrical asymmetry. This explains the need for the outer stabilization coil to counteract this effect and restore the equilibrium position of the proof mass.

Equation (3.13) indicates that levitation is proportional with the electrical conductivity of the proof mass and with the frequency and amplitude of the current in the levitation coil. A higher conductivity proof mass means lower resistance and lower impedance, and therefore a higher induced eddy current. Similarly, a higher frequency and a higher amplitude of the levitation current result in a higher magnetic flux density and consequently a higher induced eddy current.

However, as the input current frequency increases, the skin effect becomes more dominant. The skin effect is observed in the concentration of the induced eddy currents in the proof mass near the surface adjacent to the coils. This is because the alternating magnetic field of the coils can only penetrate a certain depth into the proof mass. This leads to an exponential decrease in the eddy current away from the proof mass surface, which is expressed by [108, 113]:

$$J(a) = J_s e^{-a/\delta} \tag{3.14}$$

where $J(a)$ is the eddy current density at depth $a$ into the proof mass, $J_s$ is the eddy current density at the proof mass surface adjacent to the coils, and $\delta$ is the depth at which the current density decreases to $1/e$ of $J_s$. This depth is approximated by:

$$\delta = \sqrt{\frac{2}{\mu_r \mu_0 \omega \sigma}} \tag{3.15}$$

where $\mu_r$ and $\sigma$ are the relative permeability and the conductivity of the proof mass, respectively.

This shows that the skin depth decreases with the increase in the input current frequency. As the skin effect becomes dominant, this hinders further increase in the eddy current in the proof mass and consequently limits the increase in levitation with the increase in frequency. On the other hand, increasing the amplitude of the input current in the coils, as an alternative approach to increasing levitation, leads to high heat dissipation and can cause damage to the levitation device.

The first prototype of a micromachined electromagnetic inductive levitation device was pioneered by Shearwood et al. in 1995 [114]. Using surface micromachining technology, a design with two concentric coils for levitation and stabilization, similar to the one depicted in Figure 3.3, was fabricated and used to demonstrate the levitation of 12 µm thick aluminum disc with a diameter of 400 µm within a height range of 30 µm. In 1996, Shearwood et al. presented a modified design with a three coil stator and used it to rotate the levitated disc with 100 rpm speed [115]. In 2000, Shearwood et al. demonstrated a higher rotational

speed of 1000 rpm using a design including a four-phase stator [116]. The group of Zhang et al. proposed an alternative design in 2006 where they separated the coils for levitation, stabilization, and rotation [117, 118] and were able to achieve a rotation speed up to 1000 rpm in air and 4000 rpm in vacuum with an aluminum proof mass of 2.2 mm diameter and 20 µm thick at a levitation height of 200 µm.

The common aspect among all the micro-levitation devices mentioned above is the use of planar microcoils fabricated using surface micromachining. The main disadvantage of this approach is the limitation in the number of coil windings. The low number of windings in planar coils is compensated for by using currents as high as 800 mA [115, 119] to excite the coils. This leads to high dissipation of energy in the form of heat which results in high operating temperatures in the devices that can reach $600°C$ [116]. This can cause stresses in the metal layers leading to delamination and eventually to device failure.

Overcoming these drawbacks requires increasing the coil windings. According to Faraday's law of inductance, the electromotive force, and consequently the eddy currents induced in the proof mass, are proportional to the number of windings in the coils $N_c$ [111]:

$$\xi = -N_c \frac{\mathrm{d}\Phi}{\mathrm{d}t} \tag{3.16}$$

However, increasing the number of windings using planar microcoils means the stacking of metal layers on top of each other with multiple repeated steps of metallization, photolithography, patterning, and vias for each added layer, which increases the fabrication complexity significantly.

Another alternative to increasing the coil windings is to replace 2D planar microcoils with 3D solenoidal microcoils fabricated using an automatic wire bonder using a 3D winding process developed by Vlad Badilita et. al. [109, 120–122]. This has allowed for increasing the coil windings and improving the levitation performance while maintaining operating temperatures around $100°C$. Using the 3D wire bonding process, the two-coil configuration shown in Figure 3.3 can be can be utilized, however, with two 3D solenoidal coils instead of the

planar coils, as shown in Figure 3.4. This configuration will be adopted for the development of the miniaturized rotating slit, which is presented in Chapter 6.

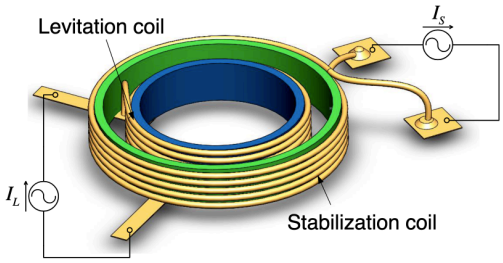


**Figure 3.4:** Electromagnetic inductive levitation structure consisting of two concentric 3D solenoidal coils for levitation and stabilization (reproduced from [110]).

## 3.4 Electrostatic Actuation

Electrostatic actuation is one of the mechanisms often used in microactuators due its simplicity, efficiency, and compatibility with standard microfabrication processes. It can achieve very fine steps with high precision. The working principle is based on the electrostatic force, which is the force between two charges, where the attraction or repulsion between the charges is utilized to create motion. According to Coulomb's law, this force is directly proportional to the product of the charges $q_1$ and $q_2$ and inversely proportional to the square of the distance $d$ between them, as given by [111]:

$$F_e = k_e \frac{q_1 \cdot q_2}{d^2} \tag{3.17}$$

where $k_e$ is Coulomb's constant ($8.9876 \times 10^9\ \mathrm{Nm^2/C^2}$).

In the context of microactuators, the charges are distributed on surfaces facing each other when a voltage $V$ is applied, as shown in Figure 3.5. The charged surfaces, referred to as electrodes, form a parallel-plate capacitor with capacitance $C$ given by [111]:

$$C = \varepsilon_0 \varepsilon_r \frac{A}{d} \tag{3.18}$$

where $\varepsilon_0$ is the permittivity of free space and $\varepsilon_r$ is the relative permittivity of the medium between the two plates, $A$ is the overlap area of the plates, and $d$ is the distance between them, as shown in Figure 3.5.

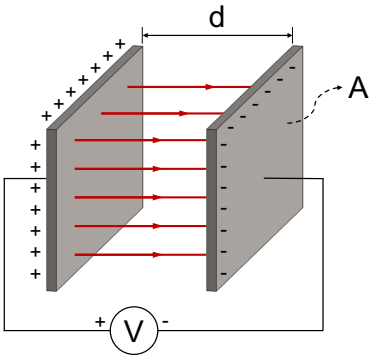


**Figure 3.5:** Schematic representation of the parallel-plate capacitor [111].

The attraction between the opposite charges on the parallel electrodes gives rise to the electrostatic force that can move the electrodes relative to each other. This force can be derived from the energy $U$ stored in the capacitor and can be expressed as [111]:

$$F_e = -\frac{\mathrm{d}U}{\mathrm{d}x} = \frac{1}{2}\frac{\mathrm{d}C}{\mathrm{d}x}V^2 \tag{3.19}$$

The derivative $\frac{\mathrm{d}C}{\mathrm{d}x}$, where $x$ is a variable representing the displacement, indicates that the displacement of the movable electrode, and the accompanying change in the separation distance or the overlap area between the electrodes, affects the capacitance, and consequently the electrostatic force. This variable capacitance effect is the key principle behind electrostatic stepper motors.

The stepper motor consists of a stationary stator and a movable rotor, as illustrated in Figure 3.6. The stator consists of multiple electrodes arranged in a pattern

that three distinct phases are created. The rotor is positioned in close proximity to the stator without any contact between the two. A step motion is achieved by activating one phase of the stator electrodes to generate an electrostatic force, which attracts the adjacent rotor electrodes to align with the current active phase. By sequentially shifting the active phase of the stator, a moving electrostatic field is generated which causes the rotor to follow. By precisely timing the activation sequence and controlling the applied voltages, the rotor motion can be discretized in fine steps to control its positioning. The number of steps and the step resolution of the motor depends on the number of electrodes and the precision of the applied voltages.

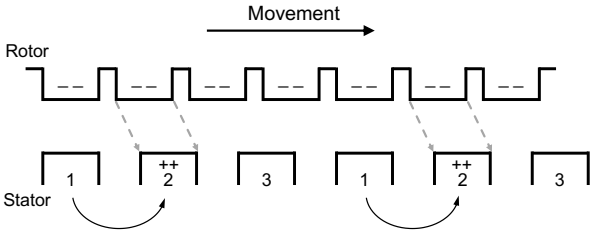


**Figure 3.6:** The working principle of a three-phase electrostatic motor where the sequential activation of stator electrodes creates an electrostatic force that moves the rotor to align with the active phase.

In the case of a rotational stepper motor, like the rotating slit presented in Chapter 6 and shown in Figure 3.7, the stator and rotor electrodes are arranged in a circular pattern. The sequential activation of the stator electrodes, in this case, gives rise to electrostatic torque $\tau_e$ and leads to angular displacement of the rotor which changes the overlap area between the stator and rotor electrodes. For two opposite electrodes, this area is defined by the inner and outer radii $r_{in}$ and $r_{out}$ and the overlap angle $\theta_{overlap}$ of the two electrodes as given by:

$$A = \frac{(r_{out}^2 - r_{in}^2)}{2} \theta_{overlap} \tag{3.20}$$

where $\theta_{overlap}$ is in radians. Substituting this area into Eq.(3.21), the capacitance becomes:

$$C = \varepsilon_0 \, \varepsilon_r \, \frac{(r_{out}^2 - r_{in}^2)}{2h} \, \theta_{overlap} \tag{3.21}$$

where the separation distance $d$ was substituted by the levitation height $h$ which separates the stator and rotor electrodes in the case of the levitating slit in Figure 3.7. Consequently the electrostatic torque $\tau_e$, in this case, becomes:

$$\tau_e = \frac{1}{2} \frac{\mathrm{d}C}{\mathrm{d}\theta_{overlap}} V^2 = \varepsilon_0 \, \varepsilon_r \, \frac{(r_{out}^2 - r_{in}^2)}{4h} \, V^2 \tag{3.22}$$

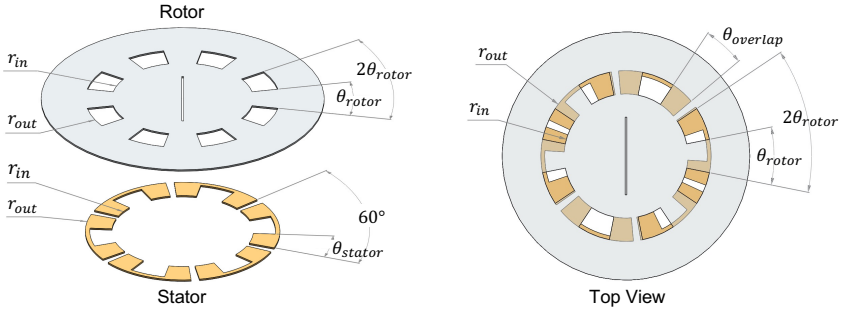


**Figure 3.7:** Design of an 8-electrode rotating slit with a three-phase stator highlighting the main design parameters defining the electrode sizes and their overlap area. The top view on the right demonstrates the scenario where the slit electrodes are aligned with one phase of the stator electrodes, distributed between the top right and the bottom left corners.

With the advantages of electrostatic actuation, there are still some considerations that need to be taken into account. One consideration is the pull-in effect, where the parallel electrodes snap together when the applied voltage reaches a critical value. In scenarios where the actuation takes place along the separation distance between the electrodes, this limits the maximum displacement of the actuator to roughly one-third of the initial distance. Another consideration is the dielectric breakdown which can cause an electric sparkover leading to a device failure. This can occur if the applied voltage is too high causing the ionization of the dielectric molecules between the two electrodes.

# 4 Internal Line-Scan HSI System

The work presented in this chapter was published by the author and is reproduced here from:

- [MA1] M. Abdo, E. Förster, P. Bohnert, V. Badilita, R. Brunner, U. Wallrabe, and J.G. Korvink. “Dual-mode pushbroom hyperspectral imaging using active system components and feed-forward compensation”. Review of Scientific Instruments 89.8 (2018), with the permission of AIP Publishing.
- [MA4] M. Abdo, E. Förster, P. Bohnert, M. Stürmer, V. Badilita, R. Brunner, U. Wallrabe, and J.G. Korvink.“Automatic correction of diffraction pattern shift in a pushbroom hyperspectral imager with a piezoelectric internal line-scanning uni”. Photonic Instrumentation Engineering IV. Vol. 10110. pp. 24-31. SPIE 2017.

This chapter presents a new system concept for hyperspectral imaging based on the pushbroom spatial-scan technique. The new concept follows the “inside approach”, discussed in Section 2.3, to develop a pushbroom system with active internal components, with the aim to offer better performance and higher flexibility in a more compact size form. The new system contains two main active components: an internal line-scanning unit and a rotating camera mechanism. By incorporating these active internal components, the new system offers higher flexibility without compromising performance. The spatial scanning is achieved using a precisely moving slit, without the need for any relative motion. The rotating camera provides the flexibility of switching between 2D spatial imaging and spectral imaging without the need for additional imaging components. More flexibility is achieved through a novel feed-forward compensation function, which is established by the

automated synchronization of the active components. This function allows more flexible data acquisition, through selection of specific regions of interest, while maintaining the spectral calibration of the system and ensuring the use of the maximum area of the image sensor.

Section 4.1 illustrates the working principle of pushbroom HSI systems, introduces the new system concept, and explains the opto-mechanical construction of the system. Before the new system can be used for spectral imaging, spectral calibration is needed, which is presented in Section 4.2, which also demonstrates the spectral resolution that can be achieved by the system. In Section 4.3, the novel feed-forward compensation function, which enables the automation and synchronization of the two main active components, is explained and experimentally demonstrated. Section 4.4 provides the first experimental validation of the system while Section 4.5 summarizes the outcomes of the work presented in the chapter.

## 4.1 System Concept & Construction

The presented system is based on the pushbroom hyperspectral imaging method, which is illustrated schematically in Figure 4.1. A slit aperture is positioned at the focal plane of the front optics, where an intermediate image of the target is produced. The slit selects one line of the image, which is collimated and projected through the transmission diffraction grating. For each point on the line, the grating produces a spectrum, which is resolved laterally across the CCD detector and recorded. The recorded spectra for each line of the image constitute one plane of the hyperspectral data cube.

The construction of the system is shown in Figure 4.2, and is based on the design developed by the SciTec Group of the Ernst-Abbe-Hochschule Jena [123–125] within the collaborative project EAGLE II[1]. The system incorporates two active components: the internal line-scanning unit and the rotating camera mechanism.

[1] Biomimetisches hyperspektrales Kunstauge auf der Basis von Effizenz adaptiven Gittern und Linsen aus Elastomeren (EAGLE II). Project No.74851430 of the German Research Foundation (Deutsche Forschungsgemeinschaft—DFG)

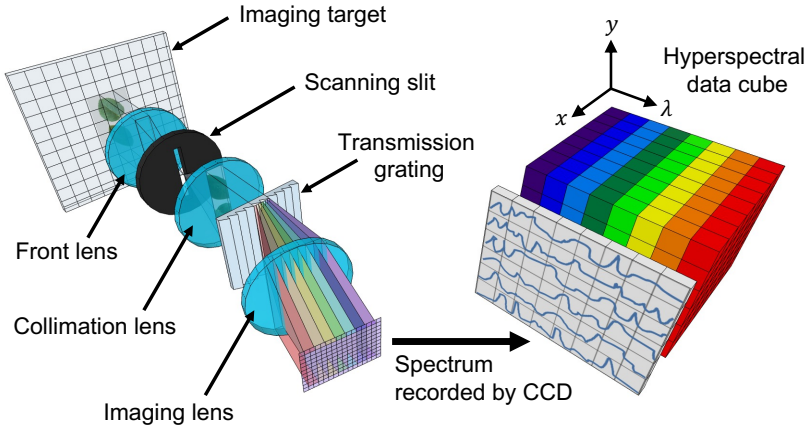


**Figure 4.1:** Schematic illustration of the working principle of the pushbroom hyperspectral imaging technique. Reproduced from [MA1, MA4].

The internal line-scanning unit, shown in a closer view in Figure 4.2(b), consists of a commercial slit with a width of 20 µm (product no. S20R, Thorlabs, USA) mounted to a linear piezo motor (Piezo LEGS LL10, PiezoMotor, Sweden). A position gauge fixed to the back of the piezo motor, in combination with a position encoder (Mercury MII6000, MicroE Systems, USA), allow moving the slit with a step resolution of 100 nm. The unit is mounted into the system so that the slit aperture is positioned at the focal plane of the front optics, which allows the spatial scanning of the target image without the need for relative motion between the target and the system. This eliminates the need for complex external scanning mechanisms, and offers more flexibility in data acquisition, which enhances the adaptability of the system to different application scenarios. The motion range of the piezo motor allows moving the slit completely outside the intermediate image, which facilitates switching between 2D spatial imaging and spectral imaging.

The second active component in the presented system is the rotating camera mechanism, which enables the switching between the two imaging modes and is essential to establishing the feed-forward compensation function, which is

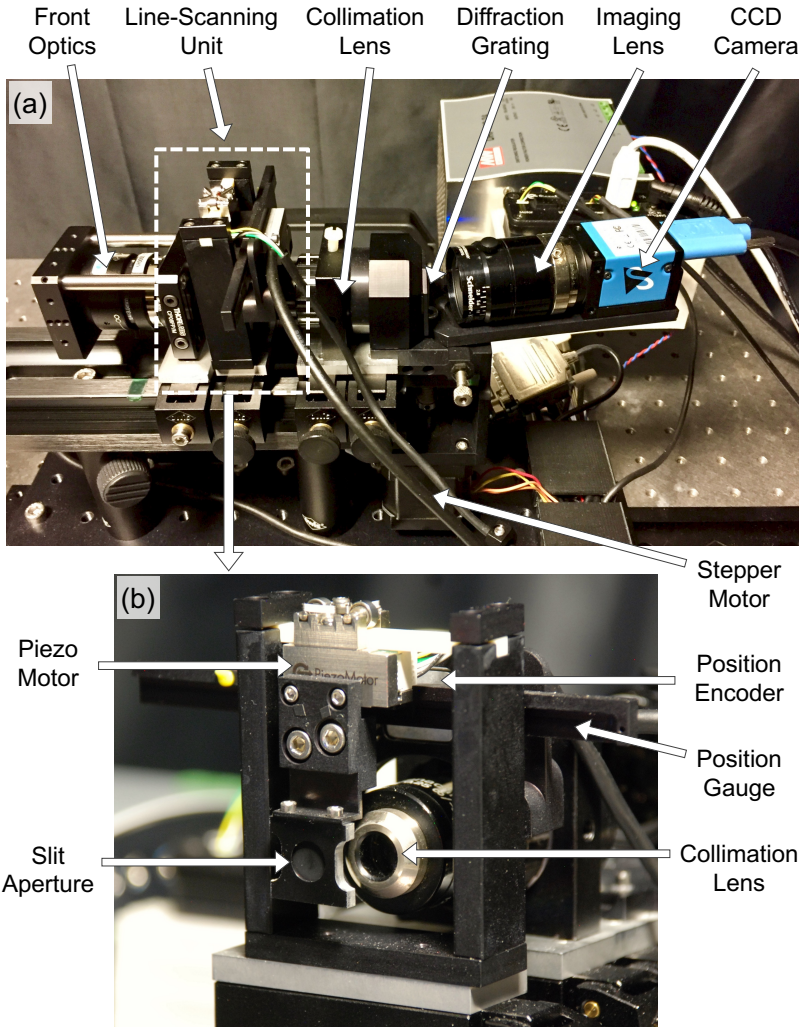


**Figure 4.2:** (a) Construction of the dual-mode spatial-scan hyperspectral imaging system. (b) A closer view of the internal line-scanning unit consisting of the slit aperture mounted to the piezo motor. Reproduced from [MA1].

presented in the following section. A monochrome CCD camera (DMK 23U274, The Imaging Source, Germany) is equipped with an imaging lens (Xenoplan 2.8/50-0902, Schneider Kreuznach, Germany) to focus the incoming light on the CCD detector, which has an array of 1600 $\times$ 1200 pixels. The camera is mounted on a rotating arm where the angle of rotation is controlled by a stepper motor (ST4209, Nanotec Electronic, Germany), which has a step angle of 0.9°. The motor is driven by a stepper motor controller (SMCI12, Nanotec Electronic, Germany), which enables precise positioning of the camera arm with a step resolution of 1/64 of the motor step angle, resulting in a minimum angular step size of approximately 0.014°.

In the spatial imaging mode the light travels directly through the system to form a 2D image of the target on the CCD sensor. In the spectral imaging mode, the slit is moved to select one line of the intermediate image formed by the front optics, which consist of a wide angle machine vision lens (3.5 mm EFL, product no. MVL4WA, Thorlabs, USA) in combination with an f60 biconvex lens. The image line is collimated and magnified by the collimation lens (microscope objective, GF Planachromat 12.5$\times$/0.25, Zeiss Jena, Germany). The transmission diffraction grating (300 lines/mm – product no. GT13-03, Thorlabs, USA) is mounted manually into the system to produce the spectrum for the selected image line. Finally, the rotating camera is positioned at the angle of the first diffraction order to capture and record the produced spectra.

## 4.2 Spectral Calibration

Spectral calibration is an essential step to enable hyperspectral imaging in a push-broom system. With the vertical orientation of the slit and the grating in the presented system, shown in Figure 4.1, the diffraction image recorded by the CCD detector for each slit position is a 2D image, where the $y$-axis corresponds to different points along the slit, and the $\lambda$-axis corresponds to different wavelengths, while the spatial scanning is done along the $x$-axis. By mapping the pixel columns of the detector to narrow contiguous spectral bands, as shown in Figure 4.3,

and recording the light intensity for each band, the spectral information can be extracted.

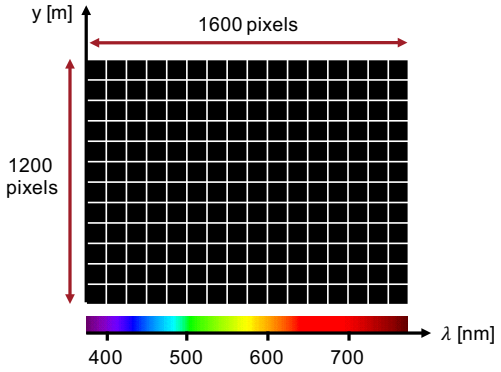


**Figure 4.3:** Representation of the spectral calibration of the CCD detector by mapping pixel columns to spectral bands. Reproduced from [MA1].

In order to establish the spectral calibration, light sources with well-defined emission spectra are used as a reference for pixel mapping. In the calibration setup shown in Figure 4.4, three lasers with the wavelengths 450 nm (blue), 532 nm (green), and 635 nm (red), (products no. CPS450, CPS532, and CPS635, Thorlabs, USA), are used together with an Hg(Ar) spectral calibration lamp (product no. 6035, Newport, USA). The lasers and the spectral lamp are aligned on top of each other as seen in the spatial mode view in the inset. The monochrome camera is replaced with an identical color camera (DFK 23U274, The Imaging Source, Germany) for better representation of the results. In the spectral mode, the light from each source is diffracted based on its wavelength resulting in the three laser spots and the spectral lines of the Hg(Ar) lamp being resolved laterally across the CCD detector as shown in Figure 4.5. To establish the pixel mapping, a vertical line is drawn at the center of each laser spot to indicate the pixel column number corresponding to each laser wavelength, which is highlighted on the horizontal axis at the bottom of Figure 4.5.

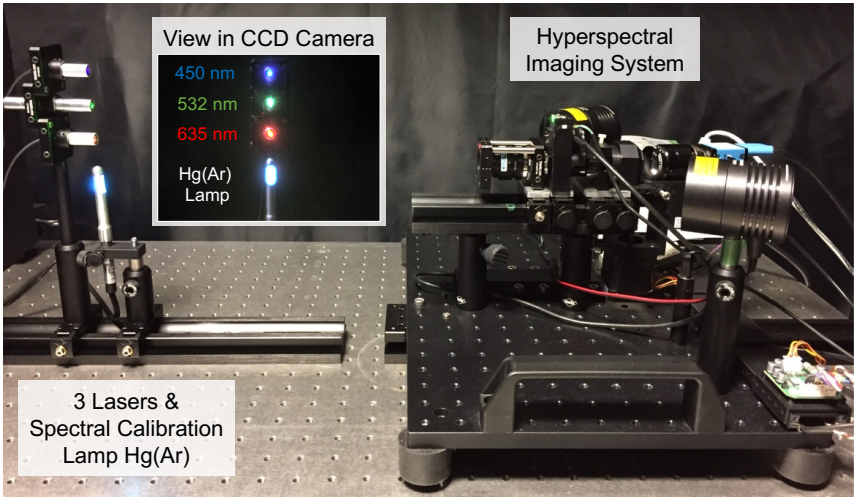


**Figure 4.4:** Spectral calibration setup using three lasers with different wavelengths in addition to Hg(Ar) lamp. The inset shows the calibration light sources in the spatial imaging mode. Reproduced from [MA1].

Using the wavelength differences, and the distances in pixel columns between the reference lines of the three lasers, the pixel columns 204 and 1382 are calculated for the spectral range limits of the system at 400 nm and 750 nm, respectively, as depicted in Figure 4.5. The limits are defined based on the transmission characteristics of the optical components and the sensitivity of the CCD detector, and they restrict the area of the detector that can be used for spectral imaging, which represents about 74% of the total sensor area. This can be improved by adapting the selection of the optical components and the image sensor to have a broader spectral range for the system.

From the spectrum of the Hg(Ar) lamp, two contiguous lines can be distinguished in the yellow range, which are magnified in the inset in Figure 4.5. The two lines belong to the Hg spectrum and have the wavelengths 576.96 nm and 579.06 nm, respectively [126]. This demonstrates a spectral resolution of approximately 2 nm for the presented system, which is suitable for a wide range of applications.

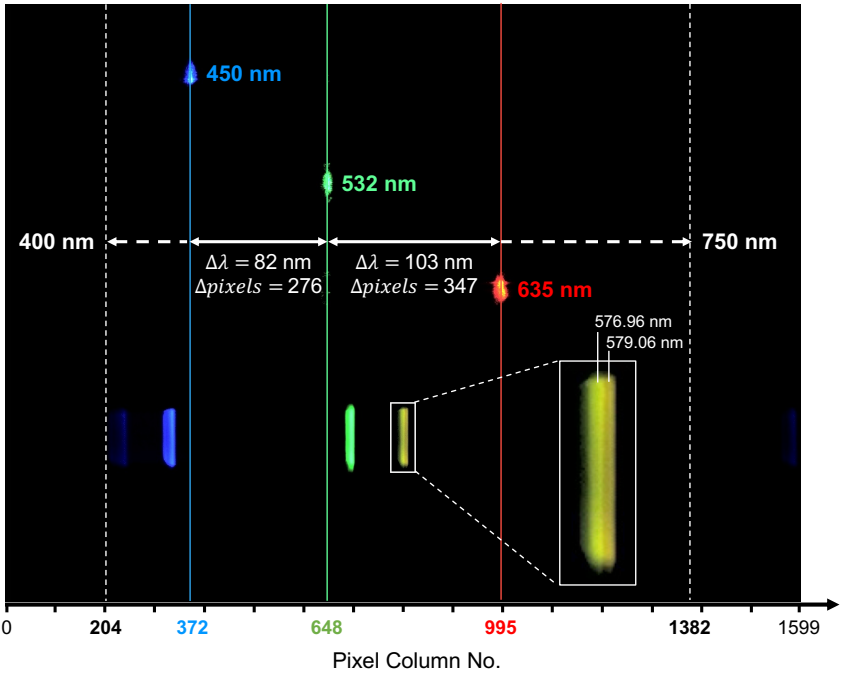


**Figure 4.5:** Calibration light sources in the spectral imaging mode are used for mapping pixel columns to spectral bands, defining the spectral range limits between 400 – 750 nm on the CCD detector, and demonstrating the spectral resolution of the system, which is approximately 2 nm. Reproduced from [MA1].

## 4.3 Slit Scanning & Feed-Forward Compensation

The spectral calibration in the previous section was established with the slit positioned at the center of the image, which coincides with the optical axis of the system. As the slit moves away from the optical axis to scan the target, the light passing through the slit has a different angle of incidence to the grating,

and consequently a different first order diffraction angle for each slit position, according to the grating equation (Eq.(3.1)):

$$\Lambda \sin \theta_m - \Lambda \sin \theta_i = m\lambda$$

where $\theta_m$ is the diffraction angle, $\theta_i$ is the incidence angle, $m$ is the diffraction order, $\lambda$ is the wavelength, and $\Lambda$ is the grating period. This in turn results in a lateral shift of the diffraction image at the CCD detector, as illustrated in Figure 4.6, which compromises the established spectral calibration of the system.

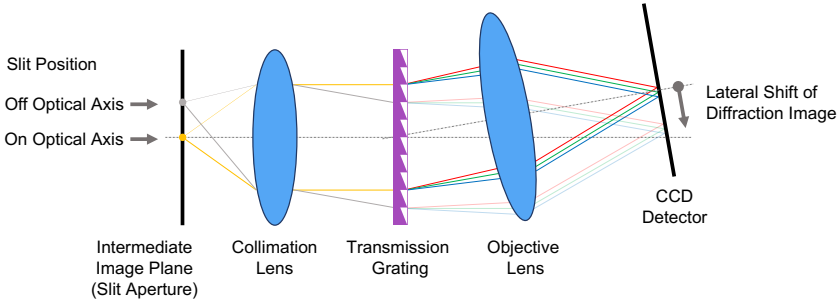


**Figure 4.6:** Lateral shift of the diffraction image on the CCD detector resulting from the scanning motion of the slit. Reproduced from [MA1, MA4].

This lateral shift is demonstrated experimentally in Figure 4.7 for different slit positions. A white imaging target is positioned in front of the system and is illuminated with the same three lasers of the spectral calibration. A diffuser plate is used to help spread out the light over the target. In the left column, the spatial mode images for slit positions selected between $-700\,\mu m$ and $700\,\mu m$ from the center slit position are shown. The images were cropped for better representation of the results. In the middle column, the spectral mode image for each slit position is provided, which has the blue, green, and red lines corresponding to the diffraction of the three lasers. All the images in the middle column were acquired while the rotation angle of the camera is fixed to $10.238^\circ$. The images show how the spectral lines of the lasers shift laterally across the CCD detector when the slit

moves from one position to the next. This lateral shift voids the established pixel mapping and spectral calibration of the system. Another drawback of the fixed camera is observed in the spectral image of slit position $-700\,\mu m$, where the blue line has shifted outside the image sensor area. This results in a loss of the spectral data for parts of the image located beyond this slit position. In systems with passive components, where the detector is fixed at a certain angle, one method to overcome these drawbacks is to limit the scanning range of the slit, which consequently reduces the area of the target image that can be scanned. Another method is to project the diffraction image on a smaller area of the image sensor, which consequently compromises the imaging resolution.

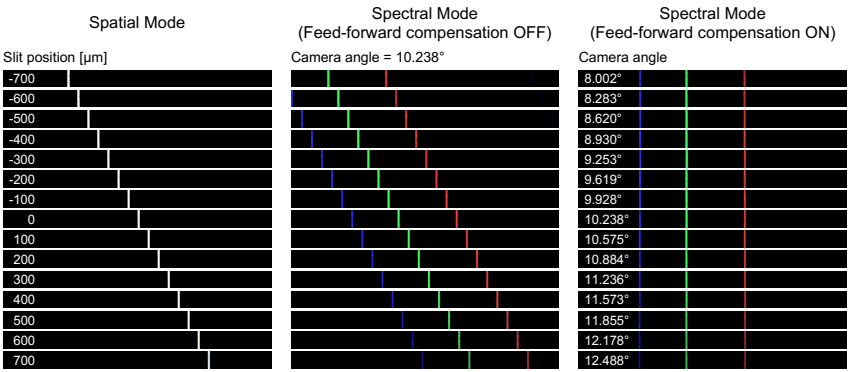


**Figure 4.7:** Experimental demonstration of the lateral shift of the diffraction image of the three lasers due to the scanning motion of the slit, and how the feed-forward compensation function can be used to compensate for this shift and maintain the spectral calibration of the system. Reproduced from [MA1].

To solve the lateral shift problem, a new method is proposed. This method allows to maintain the spectral calibration of the system during slit scanning, without sacrificing the scanning range nor the imaging area of the sensor. Following the approach of using active system components, this method is based on utilizing the rotation mechanism to adjust the angle position of the camera for each slit position to compensate for the shift in the diffraction image on the CCD detector. This is demonstrated in the right column of Figure 4.7, which shows the spectral mode

image for each slit position after adjusting the camera angle to bring the spectral lines of the three lasers back to their reference position defined in the spectral calibration. By expanding the measurements in Figure 4.7 for slit positions defined across the scanning range of the slit from $-1200\,\mu m$ to $1200\,\mu m$, with a distance of $50\,\mu m$ between each two positions, and recording the camera angle required to maintain the spectral calibration for each slit position, a linear relation is found between the camera angle and the slit position, which is expressed by the equation:

$$\theta_{Camera} = 10.247258 + 0.003253 \times SlitPosition \tag{4.1}$$

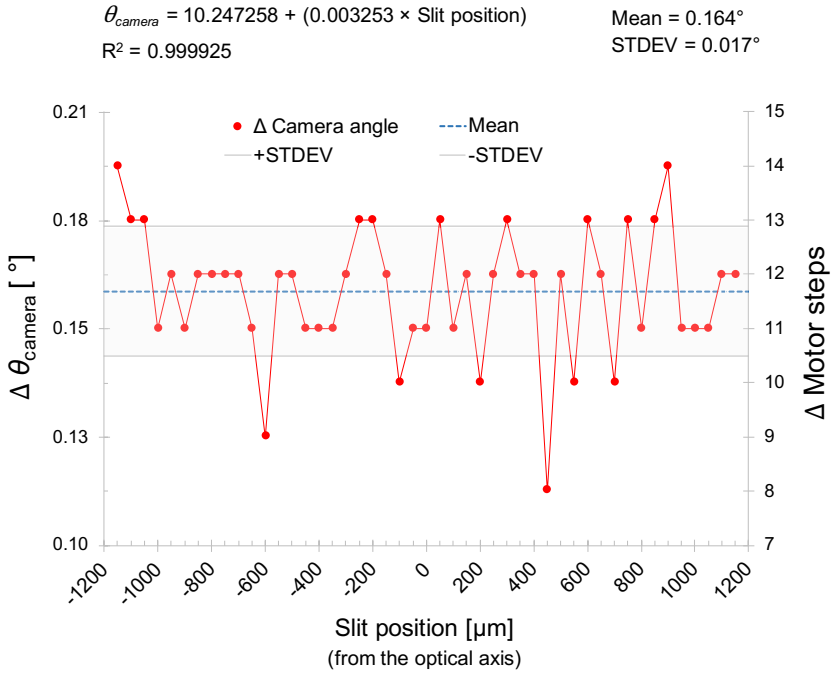


**Figure 4.8:** Change in camera angle corresponding to change in slit position showing the effect of the quantization error of the stepper motor controller. Reproduced from [MA1].

Using this relation, the feed-forward compensation function is established by programming the relation expression into the system control software to automatically synchronize the rotation of the camera with the scanning motion of the slit. Establishing the feed-forward compensation function enables hyperspectral imaging and automated data acquisition in the presented system, which is demonstrated in the following section.

The change in the camera angle ($\Delta\theta_{Camera}$) corresponding to the shift from one slit position to the next in the experiments above is shown in Figure 4.8. While the distance between each two slit positions is fixed to 50 µm, the corresponding change in the camera angle varies around a mean value of 0.164°. The number of motor steps corresponding to this mean value falls between 11 and 12. Therefore, the variation in the camera angle can be attributed to the quantization error of the stepper motor controller, which has an angular step resolution of about 0.014°. This can be improved using a more precise controller and a stepper motor with a smaller step size.

## 4.4 System Validation

This section provides a proof-of-concept experiment to demonstrate hyperspectral imaging using the presented system. In this experiment, the setup shown in Figure 4.9 is used, where an artificial plant is placed in front of the system as an imaging target. Within the artificial plant, three real plant leaves are hidden, as shown in the inset in the figure. The real and artificial leaves appear similar in color and can be difficult to distinguish by the human eye. The main objective of the experiment is to use the system to acquire the spectral data of the target, to extract and compare the spectra of the leaves, and to distinguish between real and artificial leaves. Two Quartz Tungsten-Halogen lamps with broadband emission (product no. QTH10/M, Thorlabs, USA) are used to illuminate the target, and two diffuser plates are used to spread out the light more evenly on the samples.

The control software of the system was developed in LabVIEW®, and is shown in Figure 4.10. The software is used to control the active system components, and

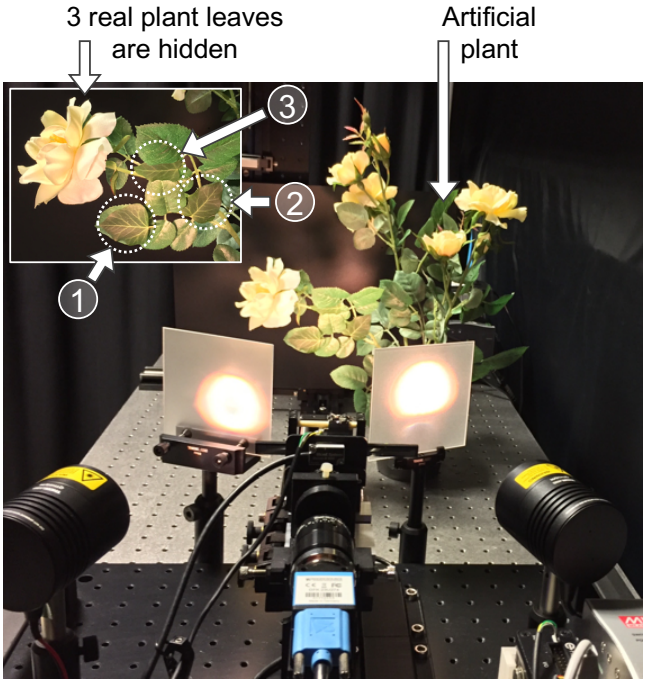


**Figure 4.9:** Validation experiment using the HSI system to reveal real plant leaves, numbered 1, 2, and 3 in the inset, which are hidden in an artificial plastic plant. Reproduced from [MA1].

allows the user to adjust the slit position and the rotation angle of the camera. The software is also used to switch between spatial and spectral imaging modes automatically, except for the grating which is mounted on and off manually. The feed-forward compensation function, which synchronizes the position of the slit and the camera, is programmed into the software and can be switched on and off by the user. The main user interface window provides live feed from the CCD camera. In Figure 4.10, the live feed shows the target plant leaves in the spatial imaging mode. The leaves for which the spectral data is extracted are numbered, where leaves 1 – 3 are real and leaf 4 is artificial.

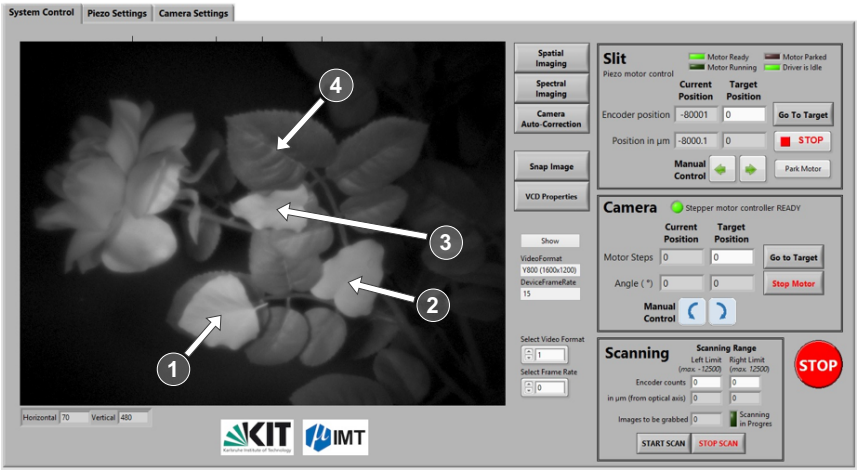


**Figure 4.10:** System control software in LabVIEW showing the real plant leaves hidden in the artificial plastic plant viewed in the spatial monochrome mode of the system. Reproduced from [MA1].

In order to acquire the spectral information for the plant leaves, the system is switched to the spectral imaging mode and the feed-forward compensation function is activated. The slit is moved to select the image lines where the leaves are located, which correspond to slit positions $-220\,\mu m$, $0\,\mu m$, $460\,\mu m$. For each slit position, the camera angle is adjusted automatically by the feed-forward compensation function, and a 2D image is recorded to capture the spectral data. The spectrum for each leaf is extracted by plotting the recorded intensity of the incoming light against the wavelength range of the system.

The spectra are extracted using MATLAB®, and are shown in Figure 4.11, where the intensity was normalized with respect to a spectrum obtained from imaging a white reference. The figure shows a clear distinction between the spectra of the real leaves and the spectrum of the artificial leaf. The figure also shows good matching between the spectra of the real leaves relative to each other, and also compared to the spectrum of Chlorophyll, which is found in green plant leaves [127, 128]. This provides validation for the presented hyperspectral

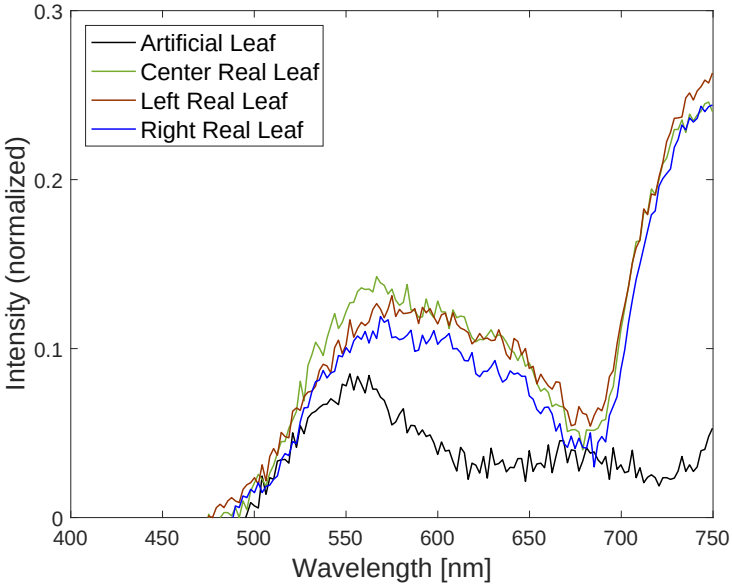


**Figure 4.11:** Extracted spectra from the validation experiment showing clear distinction between the real plant leaves and the plastic leaf. Reproduced from [MA1].

imaging system, and demonstrates how the system can be used in target detection applications, for example, to reveal hidden objects in a scene.

This experiment also demonstrates how using active system components has enabled high flexibility in the presented system. For example, using the scanning slit, it was possible to acquire the spectral data only for specific regions of interest, which are the image lines where the real plant leaves are located. This can help save time and use storage and processing resources more efficiently. The rotating camera mechanism, while enabling the feed-forward compensation function, also allows access to the spatial view of the target, which can be used to select the regions of interest. With the automation and synchronization of the system components established in the control software, the entire hyperspectral data cube can be acquired by scanning through the entire range of slit positions

from $-1200\,\mu m$ to $1200\,\mu m$, with steps equal to the slit width of $20\,\mu m$. This results in a $121 \times 1200 \times 169$ data cube, which can be acquired in less than one minute.

## 4.5 Conclusions

This chapter demonstrated the advantages of using active system components in the realization of pushbroom hyperspectral imaging systems. A new system concept was presented employing an internal line-scanning unit and a rotating camera mechanism, which offers higher flexibility compared to conventional spectrographs with passive components. Using the scanning unit, the spatial scanning for data acquisition is achieved without relative motion between the target and the system, which reduces the instrumentation complexity and allows more application scenarios. The rotating camera enables access to both spatial and spectral imaging modes in one system. In conventional systems, this requires the use of multiple cameras. A novel feed-forward compensation function to compensate the shift in the diffraction angle resulting from the scanning motion of the slit is established through automation and synchronization of the active system components. This function allows data acquisition without sacrificing the scanning range nor the imaging resolution. The feed-forward compensation function also facilitates higher flexibility in determining the size of the acquired dataset by selecting regions of interest. A spectral resolution of approximately 2 nm was demonstrated for the presented system, which is comparable to the state-of-the-art and suitable for a wide range of applications. The resolution can be improved by opting for a narrower slit width, or using a grating with a higher dispersive power. However, the spectral resolution can be degraded by the quantization error of the stepper motor controller, which affects the accuracy of the angle position of the rotating camera. A more precise controller and a motor with a smaller step angle can be used to avoid this degradation.

The advantages and flexibility in the presented system were enabled by using two active components, which were automated and synchronized. However, one

main component is still passive, which is the diffraction grating. The passive grating, which needs to be manually mounted on and off in the system to switch between spatial and spectral imaging, puts a limit to the automation and flexibility of the presented system. This creates the next opportunity for integrating an active component to improve the system by replacing the passive grating with an active switchable grating, such as the switchable phase grating in [129] as an example, which can lead to a fully automated system. Another opportunity is to realize the internal scanning unit in a more compact form, for example using a variable optofluidic slit aperture [130]. Therefore, continuing to adopt the internal active components approach opens the door for realizing more flexible and more compact pushbroom systems in the future.

# 5 Internal Rotational-Scan HSI System

The work presented in this chapter was published by the author in:

[MA2] Mohammad Abdo, Vlad Badilita, and Jan Korvink. “Spatial scanning hyperspectral imaging combining a rotating slit with a Dove prism.” Optics Express 27.15: 20290-20304 (2019). 

This chapter continues to adopt the “inside approach” and the use of internal active components to present another novel concept for a spatial-scan hyperspectral imaging system based on rotational rather than linear scanning. The new system combines a rotating slit together with a rotating Dove prism. The rotating slit enables the spatial scanning of the target image internally without the need for relative motion and without additional external hardware. The rotating Dove prism, also called a “derotator” ensures that the light is transmitted to the diffraction grating without change in the incidence angle, and therefore simplifies the data acquisition procedure. The aim of this work is to provide a simpler hardware configuration for a spatial-scan hyperspectral imaging system to open the door for more applications in the future.

The system concept is explained in more detail in Section 5.1. A comprehensive description of the system construction is provided in Section 5.2. In Section 5.3, experiments and results demonstrating the rotation of the slit and the Dove prism are presented, and a validation experiment is conducted where the system is used to acquire and differentiate between spectra of different plant leaves. Section 5.4 provides a summary of the main outcomes of the chapter.

## 5.1 System Concept

A new concept for a spatial-scan hyperspectral imaging system, illustrated in Figure 5.1, is proposed. This concept introduces a rotational-scanning approach that combines a rotating slit and a rotating Dove prism to enable internal spatial scanning of the target image without additional external hardware. The slit is positioned to select one line of the intermediate image at the focal plane of the front optics, and its rotation allows scanning the target one line at a time. The Dove prism is positioned along the optical path of the light transmitted and collimated from the slit to counteract the slit rotation.

The Dove prism (DP) is an optical element typically having the geometry of a truncated right-angle prism, with a symmetry plane coinciding with its longitudinal axis, and can be used to invert or rotate an image. Light entering the prism through one of the slanted faces undergoes refraction, then total internal reflection from the long face, before exiting through the other slanted face to form an inverted, non-reversed image. When the prism is rotated around its longitudinal axis, the formed image rotates with twice the rotation angle of the prism.

In the proposed rotational-scan system, when the slit aperture and the Dove prism's symmetry plane are aligned with the vertical $y$-axis (Figure 5.1), the image line $\ell$ is transmitted through the slit and the prism in its reference orientation $\ell(\theta_{\text{ref}})$, which is aligned with the grating. Light from each point on the line is diffracted through the grating and projected over the same range of pixel columns in the image sensor, allowing the recording of a spectrum for each point. The recorded spectra represent one plane of the 3D hyperspectral data cube.

When the slit is rotated to scan the target image and acquire the data cube, while the Dove prism is fixed, the selected image line is rotated $\ell(\theta)$ when transmitted to the grating. Light from each point on the line will be diffracted through a different point along the $x$-axis of the grating. Accordingly, the spectrum of each point will be projected over a different range of pixel columns in the sensor, resulting in overlap between the spectral bands, which does not allow the extraction of spectral data. This is demonstrated experimentally in Figure 5.5.

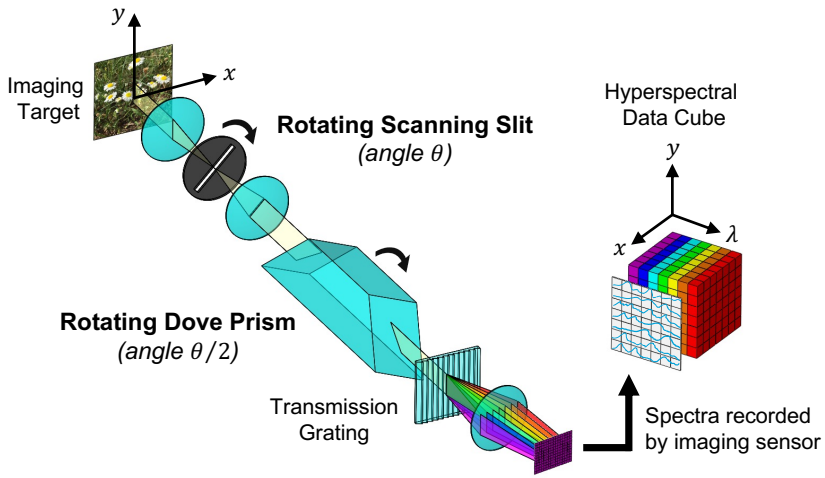


**Figure 5.1:** Schematic illustration of the system concept featuring a rotating slit and a co-rotating Dove prism (at half the slit rotation angle). Reproduced from [MA2].

By rotating the Dove prism with half the angle of the slit, as illustrated in Figure 5.1, the transmitted image line will be rotated back to its reference orientation and realigned with the grating, so that $\ell(\theta_{\text{ref}}) = DP((\theta - \theta_{\text{ref}})/2) \cdot \ell(\theta - \theta_{\text{ref}})$. Repeating this for each slit position, the Dove prism ensures the transmission of the selected image line in a vertical, upright position, aligned with the grating, avoiding the overlap of the spectral bands when recorded by the image sensor. This constitutes the working principle of the rotational-scan concept. By combining a rotating slit with a rotating Dove prism and synchronizing their rotations, the target image can be spatially scanned through the slit rotation. The Dove prism cancels the rotation effect, facilitating the extraction of spectral information.

## 5.2 System Construction

In order to demonstrate the rotational-scan concept, the system shown in Figure 5.2(a) is constructed. The front optics consist of a wide angle machine vision

lens (3.5 mm EFL, product no. MVL4WA, Thorlabs, USA) combined with an f60 biconvex lens. Together they form an intermediate image of the target. The slit has a width of 20 $\mu$m (Thorlabs No. S20R) and is fixed into a rotating mount (Thorlabs No. CRM1P/M). The slit is positioned at the intermediate image plane to select one line of the target image. The rotating mount allows scanning the slit over 360°. However a rotation of 180° is sufficient to cover all the spatial positions of the target due to the symmetrical arrangement of the slit and the system components with respect to the optical axis of the system.

The image line from the slit is collimated and magnified using a microscope objective (GF Planachromat 12.5×/0.25, Zeiss Jena, Germany). The collimated light beams then enter the Dove prism (Thorlabs No. PS992M-A)[131], which is also fixed to a 360° rotating mount. This allows rotating the Dove prism by half the angle of the slit rotation during data acquisition in order to bring the image line back to a vertical upright orientation before the light is transmitted to the diffraction grating. The grating (300 lines/mm – Thorlabs No. GT13-03) diffracts the incoming light and produces a spectrum for every point on the image line. A monochrome CCD camera (DMK 23U274, The Imaging Source, Germany) with an imaging lens (Xenoplan 2.8/50-0902, Schneider Kreuznach, Germany) is positioned at an angle corresponding to the first diffraction order to record the spectra for the selected image line.

In order to test the system concept, the imaging targets shown in Figures 5.2(b) and 5.2(c) are used. The two images were acquired by adjusting the system for spatial 2D imaging by removing the slit and the grating and aligning the CCD camera along the optical axis of the system, where an identical color camera (DFK 23U274, The Imaging Source, Germany) is used in place of the monochrome camera for better visibility of the targets. In Figure 5.2(b), three lasers are mounted above each other and positioned with an offset to the optical axis of the system. This arrangement allows selecting only one laser at a time to be viewed when using the rotating slit to scan through the field of view. Therefore, this target is used to simultaneously demonstrate the effect of the slit and the Dove prism rotation in the *spatial* imaging mode. Figure 5.2(c) shows the imaging target

used to demonstrate the effect of the slit and Dove prism rotation in the *spectral* imaging mode. Five angular positions are highlighted, which are 0°, 30°, 45°, 60°, and 90°. Each angular position is marked with a number of black stripes to facilitate its recognition when selected by the rotating slit in the spectral imaging mode.

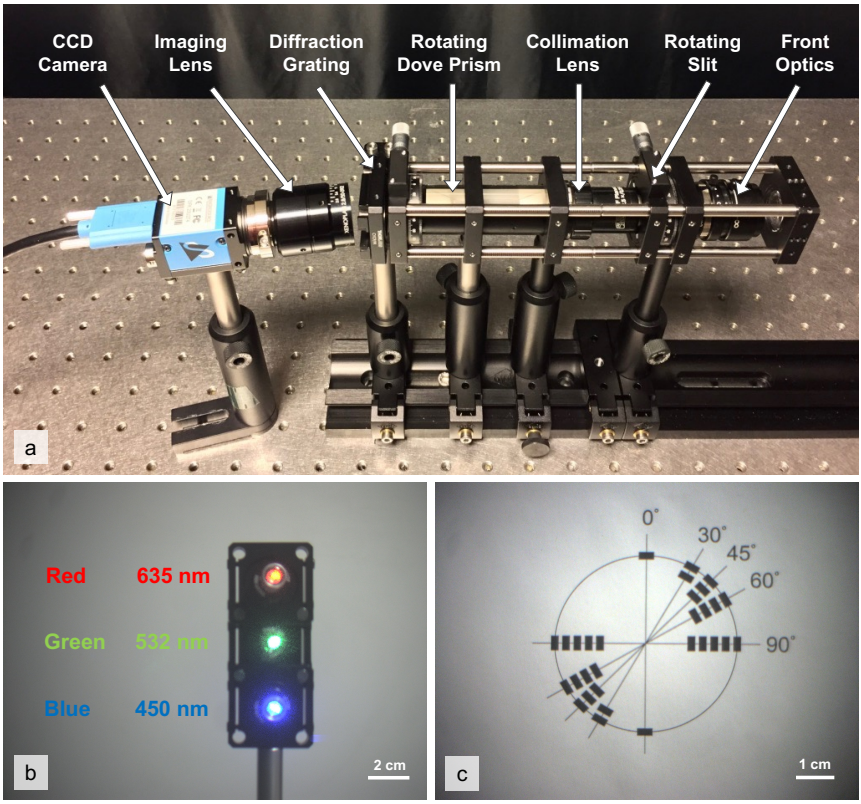


**Figure 5.2:** (a) Construction of the rotational-scan HSI system. (b) Imaging target for spatial mode with red, green, and blue lasers. (c) Imaging target for spectral mode where different number of stripes is used to highlight each angular position. Reproduced from [MA2].

## 5.3 Results & Discussion

The experimental work was divided into three parts to show how the system works in the spatial and spectral imaging modes, and to provide validation of the system. The obtained results are explained and discussed in the following subsections.

### 5.3.1 Spatial Imaging Mode

The aim of these experiments is to show how the rotating slit can be used to scan the field of view and select different points in the target image, and how the Dove prism can be used to bring the selected image line to a vertical upright orientation.

First, the slit was rotated with different angles to select each laser of the imaging target in Figure 5.2(b), while keeping the Dove prism fixed without rotation. This is

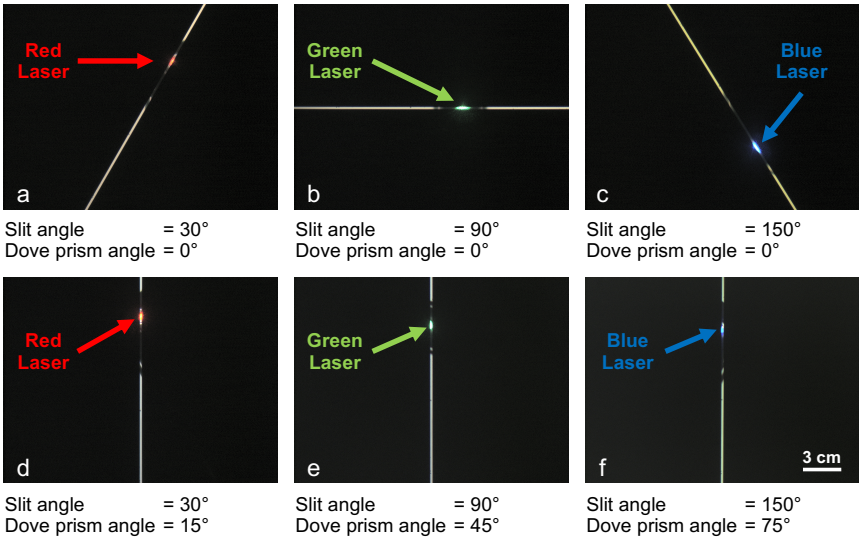


**Figure 5.3:** Experimental demonstration of the slit and the Dove prism rotation in spatial imaging mode. (a-c) The slit is rotated to access the red, green, and blue lasers, which are located at different spatial positions as shown in Figure 5.2(b), while keeping the Dove prism fixed. (d-f) By rotating the Dove prism, with half the rotation angle of the slit, the slit image can be re-oriented to the vertical upright position. Reproduced from [MA2].

shown in Figure 5.3(a-c), where the red laser was selected with a slit rotation angle of 30°, the green laser was selected when the slit was in a horizontal orientation corresponding to a rotation angle of 90°, and the blue laser was selected with a slit rotation angle of 150°. After that, the Dove prism was rotated with half the slit angle for each slit position to bring the selected image line to a vertical upright orientation, as shown in Figure 5.3(d-f). Such orientation is specifically important to facilitate spectral imaging as explained in the following subsection.

Using the rotating slit to scan the field of view means that the spatial sampling will be a function of the radius along the slit from the center of the image. For each spatial point located at $(x,y)$ from the center, the number of sampling times $N_{(x,y)}$ during a complete scan of the slit (rotation of 180°) will be inversely proportional to the radius $r_{(x,y)}$ and will range between $N_{(x,y)} = 1$ for points at the perimeter of the slit rotation ($r_{(x,y)} = \frac{1}{2} \times$ *slit length*) and $N_{(x,y)} = M$ for the center point, where $M$ is the number of angular slit positions required for a complete scan, assuming no overlap between slit positions at the perimeter. The spatial resolution, therefore, will depend on the reconstruction of the scanned image from the individual images of all slit positions. This is demonstrated in Figure 5.4, where the 1951 USAF resolution test chart is used to demonstrate the spatial resolution of the system and to show the effect of the slit rotation and image reconstruction on the spatial sampling and the spatial resolution.

The slit used in these experiments has a width of 20 µm and a length of 3 mm (Thorlabs No. S20R). This means that the number of angular slit positions required to scan a complete image of the target is approximately 236, with a step angle of approximately 0.76°, taking into account that a rotation of 180° is sufficient due to the symmetrical arrangement of the slit and the system components with respect to the optical axis of the system.

Figure 5.4(a-c) shows the USAF test chart in spatial imaging mode while the slit was removed from the optical path. These images serve as a reference for comparison with the reconstructed image in Figure 5.4(d-f). The red rectangle in Figure 5.4(a) is magnified in Figure 5.4(b) and shows group 1 of the test chart where the lines of element 6 can still be distinguished. This indicates a spatial

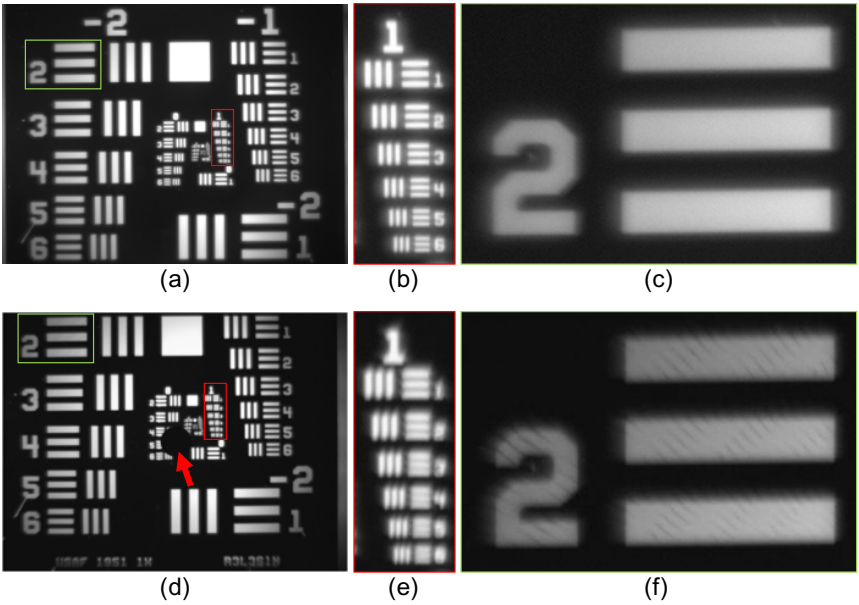


**Figure 5.4:** Spatial resolution of the system demonstrated in spatial imaging mode (a-c) and in a constructed image of 474 slit positions corresponding to a slit rotation of 360° (d-f). (a) Spatial mode image of the 1951 USAF resolution test chart. (b) Magnification of group 1 (red rectangle) indicates a spatial resolution of 140.31 µm, which corresponds to element 6. (d) Constructed image of the test chart by combining the images from 474 angular slit positions corresponding to a slit rotation of 360°. (e) Deterioration of spatial resolution to 250 µm, corresponding to element 1, due to image construction. Comparing the magnifications of element 2 in group -2 (green rectangle) in the upper left corner shows the difference between the spatial mode image (c) and the constructed image (f), where the effect of the slit rotation and image construction can be observed. The red arrow in (d) points to a black circular spot in the center of the constructed image which is due to the slit aperture being offset from the rotation axis of the slit component. Reproduced from [MA2].

resolution of 140.31 µm. Figure 5.4(c) is a magnification of the green rectangle in the upper left corner of Figure 5.4(a) and shows element 2 in group -2 of the test chart without any signs of slit scanning nor image reconstruction. In order to acquire the images in Figures 5.4(d)-5.4(f), the slit was inserted into the system. The manual re-arrangement of the system to insert the slit caused the slight translation in position of the test chart image in Figure 5.4(d) compared

to Figure 5.4(a). However, this slight translation does not affect the information obtained from the figures. Due to the large number of slit positions (≈236) and the small step angle (≈0.76°) required for a full scan of the image, which are difficult to control by manual adjustment, the rotational slit mount (Thorlabs No. CRM1P/M) was replaced with a rotational stepper motor (Thorlabs No. K10CR1) with a step angle resolution of 0.0073°. Due to a slight offset of the slit aperture from the rotation axis of the slit component with approximately 80 µm, the scanning is done by rotating the slit over 360° rather that 180° in order to minimize the area of the image which cannot be accessed by the slit rotation to the circular spot indicated by the red arrow in the reconstructed image in Figure 5.4(d). This, however, demonstrates the importance of the rotational symmetry and the high precision alignment of the system components for this technique. With 360° slit rotation and with a step angle of 0.76°, 474 slit images were acquired for the reconstruction of the test chart image in Figure 5.4(d). The image reconstruction was done using MATLAB®by combining the acquired images in a 3D matrix and then selecting the highest intensity from the scanned images for each pixel in the lateral image. The red rectangle in the reconstructed image is magnified in Figure 5.4(e) and shows group 1 of the test chart. Comparison between Figures 5.4(b) and 5.4(e) shows a deterioration of spatial resolution after image reconstruction from 140.31 µm (element 6) to 250 µm (element 1). Figure 5.4(f) is a magnification of the green rectangle in the reconstructed image and shows element 2 in group -2 of the test chart, where the signs of slit scanning and image reconstruction can be observed. This is due to the reduced number of sampling times and reduced overlap between slit positions in the upper left corner of the image, compared to other parts of the image closer to the center.

### 5.3.2 Spectral Imaging Mode

For these experiments, the system was re-arranged by inserting the diffraction grating into the optical path, and positioning the CCD camera with an angle corresponding to the first diffraction order. The color camera was used for better

demonstration of the results. The imaging target in Figure 5.2(c) was used and was illuminated by the three lasers in Figure 5.2(b), in addition to a broadband light source (Thorlabs No. QTH10/M) projected through a horizontal rectangular aperture. A diffuser glass plate was used to help spread the light over the target. The resulting image, shown in Figure 5.5, displayed blue, green, and red lines, in addition to a broad spectrum corresponding to the diffraction of the light transmitted from the three lasers and the broadband source.

First, the slit was rotated to different angles corresponding to those highlighted on the imaging target, while fixing the Dove prism without any rotation. The result is shown in the left column of Figure 5.5, where the spectral lines of the three lasers are seen to rotate as a result of the slit rotation. The rotation represents a problem for spectral imaging and for the extraction of the spectral information. This is due to the fact that, with the rotation, each pixel column of the CCD detector is recording data from different spectral bands. For example, a pixel column around the center in Figure 5.5(a-c) shows signals recorded from the blue, green, and red spectral bands, with their geometrical separation a function of the angle of rotation. In Figure 5.5(d), all spectral bands overlap with each other as the band separation reduces to zero. This prevents establishing spectral calibration for the system, where each pixel column is assigned a unique spectral band. Consequently, it hinders the extraction of spectral information for each point on the image line.

In order to solve this problem, the Dove prism is used to bring the image line back to a vertical upright orientation before the light is transmitted to the diffraction grating. By rotating the Dove prism with half the slit angle for each slit position, the vertical orientation of the spectral lines of the three lasers can be maintained, as can be seen in the right column of Figure 5.5. The black stripes crossing the spectral lines are used to recognize the rotation angle of the slit based on the imaging target in Figure 5.2(c). In Figure 5.5(h), with a slit angle of 90° and a Dove prism angle of 45°, the rectangular aperture of the broadband source is now projected to the grating in a vertical upright orientation, resulting in the broadband spectrum covering a larger area of the sensor. Maintaining the vertical orientation of the spectral bands facilitates establishing the spectral calibration of the system

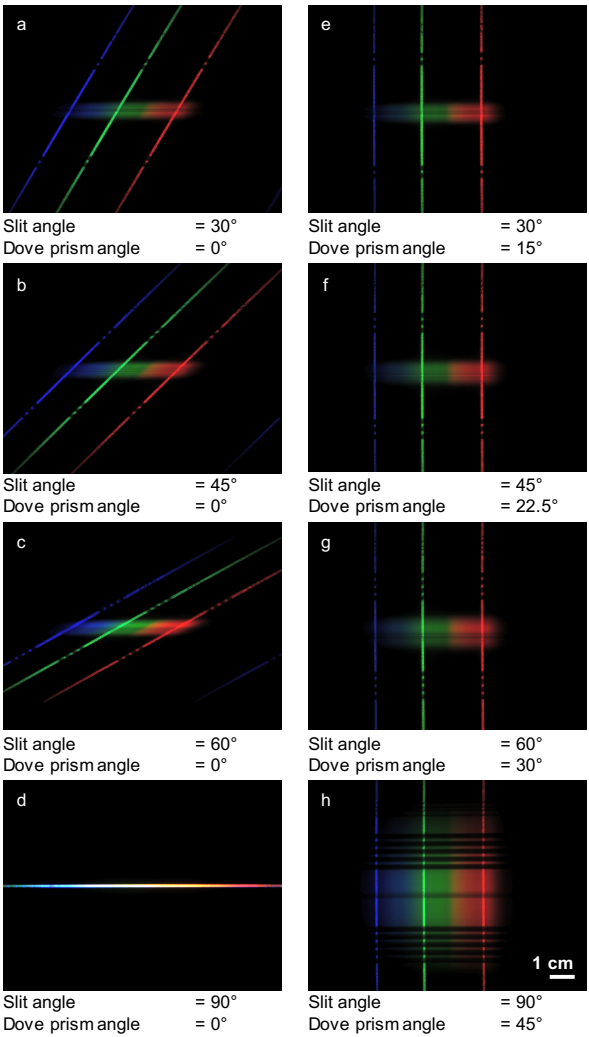


**Figure 5.5:** Experimental demonstration of the joint slit and Dove prism rotation in spectral imaging mode using three lasers and a broadband source, where the stripes crossing the spectral lines indicate the slit angular position according to Figure 5.2(c). (a-d) Rotation of the slit while the Dove prism is fixed leads to a rotation of the spectral lines of the three lasers and to loss of spectral information due to overlap of the spectral bands within the pixel columns of the sensor. (e-h) By rotating the Dove prism with half the rotation angle of the slit, the orientation of the spectral lines can be maintained in the vertical upright position. (h) At 90° rotation, the broadband light passes through the entire slit which leads to a larger vertical distribution of its spectral response. Reproduced from [MA2].

by assigning each pixel column to a unique spectral band within the spectral range of the system, which is limited between 400 nm and 750 nm. This can be done by using the wavelengths of the three lasers as a calibration reference, and by using the distances between the three spectral lines to interpolate the wavelength to be assigned for each pixel column. After establishing the spectral calibration, the system can be used for spectral imaging and for extracting the spectral information of the target.

Figure 5.6 demonstrates the spectral resolution of the system using the spectral lines of an Hg(Ar) spectral calibration lamp (product no. 6035, Newport, US). The spectrum of the Hg(Ar) lamp shows two contiguous lines in the yellow range with wavelengths of 576.96 nm and 579.06 nm. The two lines are magnified in the inset, which shows that the two lines can be distinguished, although being partially overlapped. This demonstrates that a spectral resolution close to 2 nm can be achieved with the presented system.

### 5.3.3 System Validation

The aim of this experiment is to provide validation for the system concept combining the rotating slit and the rotating Dove prism. This is achieved by using the system to acquire and extract spectral information from an imaging target, which is shown in Figure 5.7. Eight disk samples taken from real and artificial plant leaves are fixed to the target plane and arranged in a circular array. Pairs of samples are fixed along the same angular line, so that two samples can be viewed at a time when the slit is rotated to the corresponding angle. The target is illuminated with two Quartz Tungsten-Halogen lamps (Thorlabs No. QTH10/M) with broadband emission, and using two diffuser plates to distribute the light over the samples.

Starting with leaf samples 1 & 2, the slit and the Dove prism are kept in the vertical upright position without any rotation to allow the light to transmit directly to the diffraction grating. The diffraction image carrying the spectral information for the two leaves is recorded by the CCD camera, where the monochrome camera is used to record the light intensity in each spectral band without any filters. For

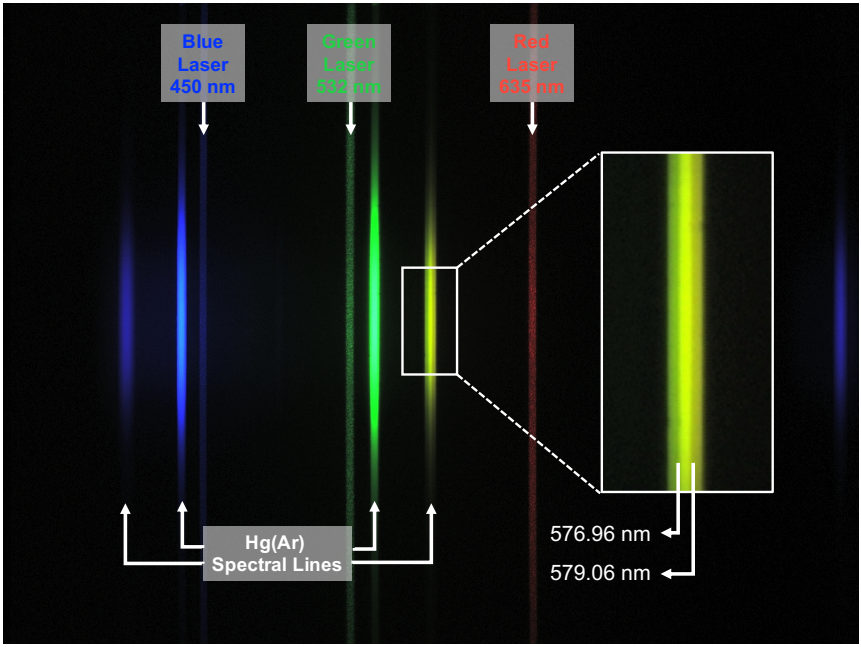


**Figure 5.6:** Demonstration of the spectral resolution of the system using an Hg(Ar) spectral lamp. The magnification in the inset shows two spectral lines with 2.1 nm separation partially overlapping. Reproduced from [MA2].

the rest of the leaves, the slit is rotated with the designated angle for each pair of leaves, the Dove prism is rotated with half the slit angle, and the diffraction image for the two leaves is recorded by the camera. The rotation of the slit and the Dove prism was done manually using two identical rotational mounts (Thorlabs No. CRM1P/M).

In the next step, the spectral information for each leaf is extracted using MATLAB®. This is done by plotting the light intensity recorded in each spectral band over the spectral range of the system, where the intensity was normalized with respect to a spectrum obtained from imaging a white reference. The acquired spectra for the eight leaf samples are shown in Figure 5.8. By comparing the spectra in the figure, the real and artificial leaves can be readily distinguished. The

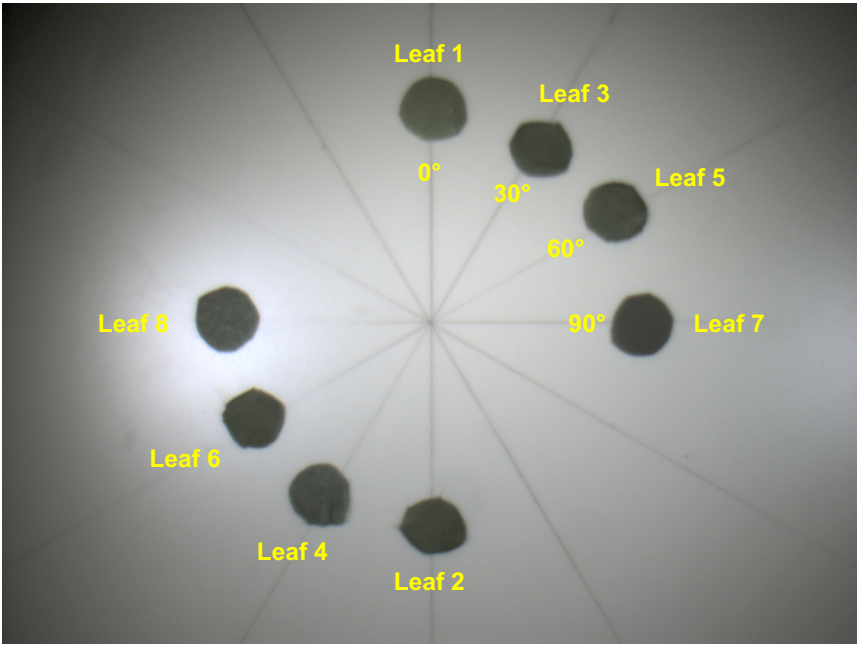


**Figure 5.7:** Imaging target for the validation experiment, combining disk samples from real and artificial plant leaves. Reproduced from [MA2].

spectra of leaves 2, 3, 5, and 6 are similar to each other, and also similar to the spectrum of Chlorophyll, which is a dye found in green plant leaves [127, 128]. This experiment provides validation for the system concept, and demonstrates how the system can be used in applications such as material sorting or target detection.

## 5.4 Conclusions

This chapter presented a new concept for spatial-scan hyperspectral imaging, which combines a rotating slit and a rotating Dove prism. It was demonstrated how the rotating slit can be used to select one line of the target image at each angular position, and how the Dove prism, when rotated with half the rotation angle of the slit, can be used to cancel the rotation effect and project the selected

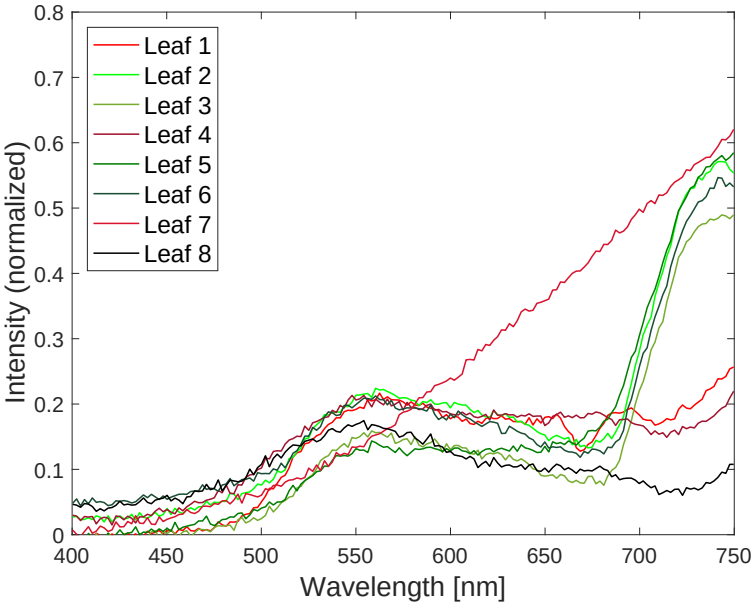


**Figure 5.8:** Extracted spectra for the plant leaves samples in the validation experiment showing the distinction between real leaves (2,3,5,6) and plastic leaves (1,4,7,8). Reproduced from [MA2].

image line in a vertical upright orientation, which is aligned with the grating. This prevents the pixel columns of the image sensor from recording signals from different spectral bands, which maintains the spectral calibration of the system and facilitates the extraction of spectral information. A spatial resolution of 140.31 µm in the spatial mode and a spectral resolution close to 2 nm in the spectral mode were demonstrated, which is sufficient for a broad range of applications. A proof of concept was provided, which showed how the system can be used for material sorting applications, as an example.

Introducing this new concept adds to the set of techniques developed for spatial-scan hyperspectral imaging. The new technique offers the further advantage of performing the spatial scanning internally without the need for relative motion

between the entire imaging system and the target, which would otherwise require additional external hardware in conventional systems. This advantage opens the door for more applications for spatial-scan hyperspectral imaging, where the relative motion is either not feasible or not practical.

Using the slit rotation for scanning leads to spatial sampling being a function of the radius from the center of the image, with the number of sampling times for each point being inversely proportional to its distance from the center, due to the overlap between adjacent slit positions. In addition, scanning a full image requires rotating the slit over a large number of angular positions with a small step angle for each position ($\approx$236 positions with $\approx 0.76^\circ$ for $180^\circ$ rotation of a slit with 20 µm width and 3 mm length). This demands high precision in rotational symmetry and alignment of the systems components, using high precision actuators to synchronize the angular positions of the slit and the Dove prism, and careful selection of the sampling routine and image reconstruction algorithm.

In the experiments presented in this chapter, a slight offset of the slit aperture from the rotational axis of the slit component lead to loss of information from a circular part around the center which could not be accessed by the rotation of the slit. Using manual actuators to synchronize the rotation of the slit and the Dove prism lead to a long measurement time for a small number of data acquisition points, in the order of $4-5$ minutes for the 4 slit positions in the validation experiment. This can be significantly improved using automated rotational motors, such as (Thorlabs K10CR1) with an angular speed of $10^\circ/\text{s}$, where it would be feasible to scan 236 slit positions in less than 30 seconds, with 30 ms of exposure time for each position. For image reconstruction, we used a simple algorithm based on selecting the maximum intensity for each pixel from the scanned slit images. The reconstructed image showed reduced spatial resolution of 250 µm in addition to slight artifacts from slit rotation and image reconstruction towards the peripheries of the image. This can be improved using a more sophisticated sampling and reconstruction algorithm that allows more overlap between slit positions and uses averaging rather than maximum intensities to improve the

signal-to-noise ratio. The spectral resolution can also be improved by using a narrower slit width or a grating with higher dispersion.

Future work will aim to further develop this system. This includes using higher precision components to ensure rotational symmetry and perfect alignment of the system components. Future developments also include replacing the manual rotational mounts with rotational motors and developing a software to automate and synchronize the rotation of the slit and the Dove prism to enable the acquisition of full hyperspectral 3D data sets. Different sampling and image reconstruction algorithms will be tested to improve the quality of the reconstructed image. In Chapter 6, the miniaturization of this concept is pursued, starting with the rotating slit mechanism.

Due to the novelty of this system, a patent application was filed to the European Patent Office (EPO) [MA7][1]. However the EPO found that an earlier patent [132] reporting a hyperspectral endoscopic device that incorporates a Dove prism to rotate the incoming image presents a similar concept and therefore the patent application was withdrawn. Nevertheless, the rotational-scan concept for hyperspectral imaging started receiving more attention after the publication of this work. Cai et al. [133] reported a rotational-scan system based on a conventional spectrograph mounted on a rotating platform in front of a fixed camera. With the lack of active components, the spectral axis of the spectral images continues to rotate for each image. To solve this problem, they used the Hough Transform algorithm to restore the spectral axis based on the rotation angle, which leads to a higher computational complexity. Luo et al. [134] reported a similar system, however with a camera that rotates with the spectrograph to avoid rotating the spectral axis. However, since the recorded images are still rotated relative to each other, they developed a reconstruction algorithm to assemble the image and the spectral dataset of the target.

[1] EP3748317 – A method and a device for acquiring spatially resolved spectral information. Application Nr. 19178381.0 filed on 05.06.2019.

# 6 MEMS Levitation Slit for Rotationl-Scan HSI

This chapter presents the initial efforts aiming at the miniaturization of the rotational-scan system based on the rotating slit and dove prism, introduced in the previous chapter. This begins with the realization of the rotating slit in a miniaturized MEMS-based chip. Section 6.1 explains the working principle of this chip, which combines electromagnetic inductive levitation and electrostatic actuation. This is followed by discussing the state-of-the-art in micro-levitation and its limitations in Section 6.2. The development of an improved microfabrication process for an optically compatible micro-levitation chip is detailed in Section 6.3. After that, Section 6.4 presents the design and fabrication of the rotating slit disc. Section 6.5 provides an experimental demonstration of the newly fabricated chip and slit disc. Finally, Section 6.6 summarizes the main outcomes of the chapter.

## 6.1 Working Principle

The working principle of the miniaturized rotating slit combines electromagnetic induction and electrostatic actuation, as illustrated in Figure 6.1. The electromagnetic induction, realized using two concentric microcoils with AC currents having 180° phase-shift to one another, provides the levitation force that lifts the slit disc to enable frictionless rotation. The AC current in the inner coil generates a time-varying magnetic field that induces eddy currents in the slit disc, which is made of non-magnetic conducting metal foil. The induced eddy currents generate a magnetic field opposing that of the coil and resulting in a repulsive force that causes the disc to levitate. The outer coil, in a similar way, provides the stabilization force

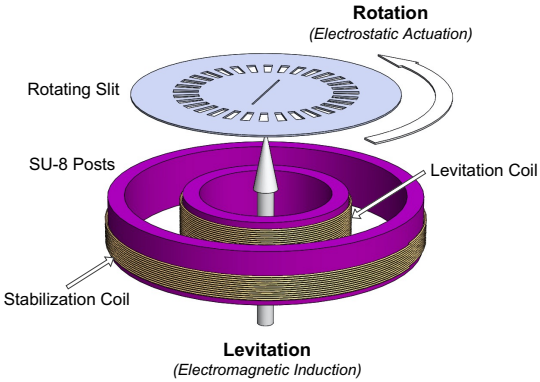


**Figure 6.1:** Schematic representation of the working principle of the miniaturized rotating slit, where electromagnetic induction levitates the slit disc and electrostatic actuation is used to control the slit rotation.

that maintains the levitating slit in its center position. This is explained in more detail in Section 3.3. The rotation and the angular position of the levitating slit disc can then be controlled by means of electrostatic actuation, explained in Section 3.4. This is achieved by integrating a circular array of capacitive electrodes in the slit disc and the top surface of the levitation chip that resembles a three-phase stepper motor. By energizing each phase of the chip (stator) electrodes, the slit disc rotates to align the adjacent phase of the slit (rotor) electrodes. By synchronizing the activation of the stator electrodes, continuous and controlled rotation of the slit can be achieved, where the size and the number of electrodes in each phase determines the minimum rotation angle and the number of slit positions that can be used for imaging.

## 6.2 State of the Art

The state-of-the-art micro-levitation chip was reported by the Group of Dr. Vlad Badilita [108, 135–139] based on the development of a microfabrication technique for 3D solenoidal microcoils using an automatic wire bonding machine [109,

120–122] (Figure 6.2). The new technique allows the 3D winding of coils around cylindrical posts to increase the number of windings to enhance the levitation performance while avoiding the use of high AC currents and the associated drawbacks of heat dissipation.

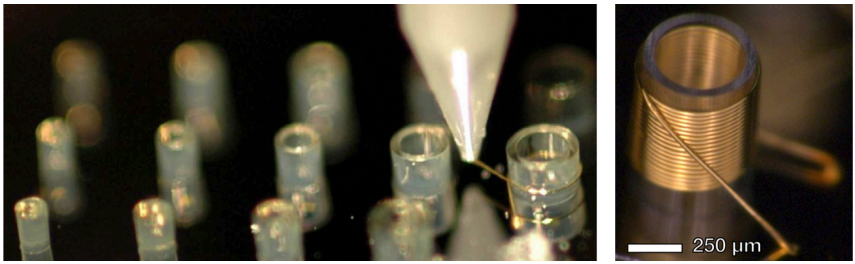


**Figure 6.2:** Fabrication of 3D solenoidal microcoils with multiple windings around supporting SU-8 structures using an automatic wire bonder and a 3D coil winding process. (Left: reproduced from [122] ©2010 IOP Publishing Ltd. Right: reproduced from [121] ©2009, with permission from Elsevier).

The state-of-the-art chip, which is shown in Figure 6.3, consists of two substrates which are assembled together using flip chip bonding and used to levitate a disc-shaped aluminum proof mass. The bottom substrate is made of a pyrex wafer and carries the two concentric 3D coils for levitation and stabilization. The top substrate is made of a silicon wafer, with 1 µm thick layer of oxide for passivation, and carries a two-phase array of electrostatic electrodes along with the electrical pads and connectors on the top side. On the backside, a deep-etched groove is opened to encapsulate the coils and bring them as close to the proof mass as possible. The chip was demonstrated to levitate proof masses with diameters ranging between 2.7 – 3.3 mm to heights ranging between 35 µm to 190 µm using an AC current with 9 MHz frequency and rms amplitude between 100 mA and 130 mA. The two-phase electrostatic electrodes were used to demonstrate angular oscillation of 37° around the vertical axis using a proof mass with four electrodes.

However, the presented state-of-the-art chip is not suited for hyperspectral imaging. First, there is no optical path for imaging through the chip. And second,

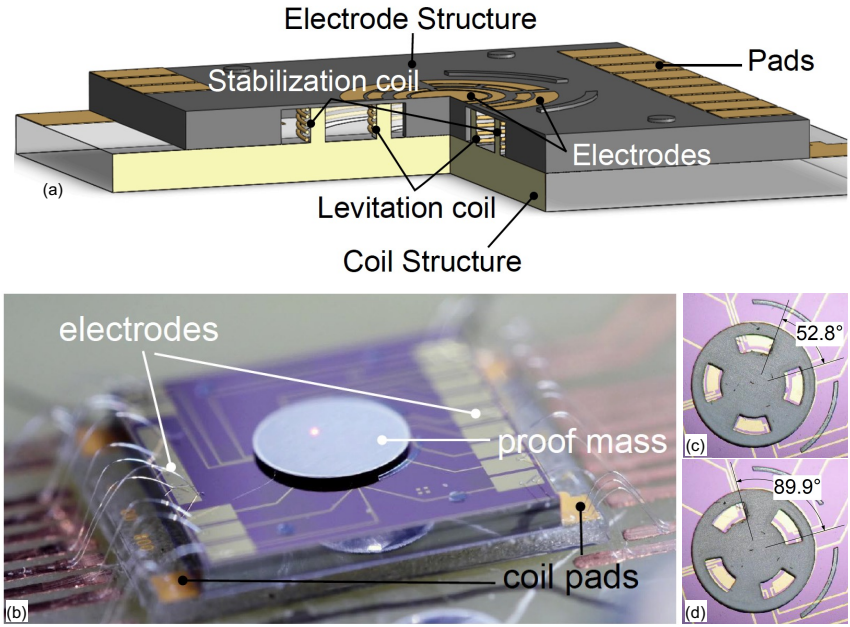


**Figure 6.3:** State-of-the-art micro-levitation chip with 3D microcoils developed by the Group of Dr. Vlad Badilita [108, 138, 139]. (a) CAD drawing of the chip revealing the two coils on the bottom substrate encapsulated into a deep-etched groove in the backside of the top substrate. (b) The assembled chip in operation with a levitating aluminum disc-shaped proof mass on top. (c) Proof mass with four electrodes aligned with the first phase of two-phase electrostatic electrodes. (d) Proof mass rotated with 37° around the vertical axis after alignment with the second phase of the electrostatic electrodes. The figure is reproduced from [108].

it is not possible to control the proof mass rotation to achieve a full scan of a field of a view using the reported design.

The next section explains the changes made to the micro-levitation chip and the improvements made to the microfabrication process to realize a chip that can be used for the rotational-scan hyperspectral imaging technique reported in Chapter 5.

## 6.3 HSI-Compatible Micro-Levitation Chip

The development of a micro-levitation chip with a rotating slit for hyperspectral imaging builds upon the state-of-the-art chip presented above. The objective is to adapt the chip design and fabrication process to establish an optical path to allow imaging through the chip, to incorporate a defined slit aperture in the proof mass to allow scanning a field of view in a sequential fashion, and to modify the electrostatic electrodes in the proof mass and the chip to control the slit rotation in pre-defined angular steps to scan the full filed of view.

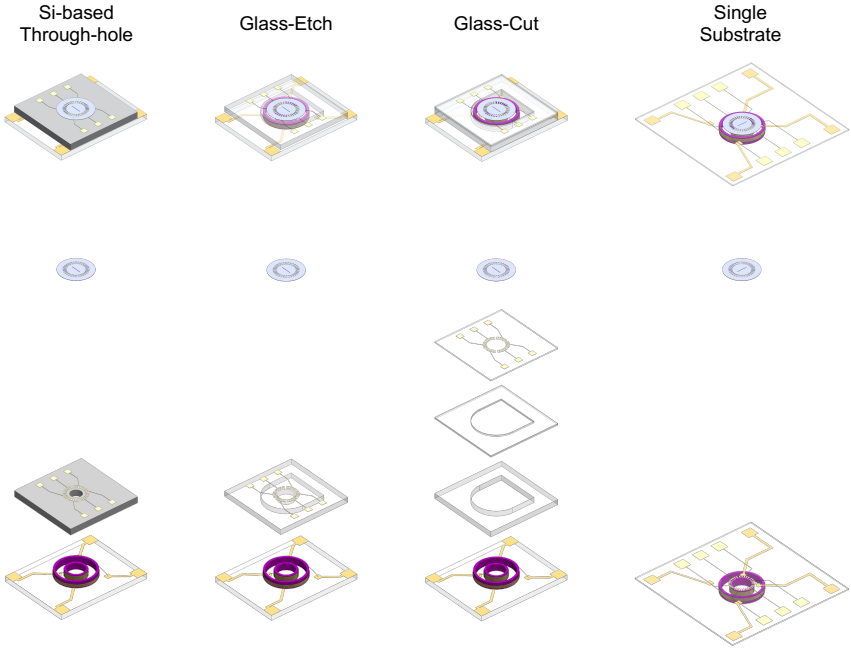


**Figure 6.4:** The development of a micro-levitation chip for hyperspectral imaging has gone through four designs. (Top) CAD view of the complete chip for each approach. (Bottom) Exploded CAD view of each chip.

This adaptation process has gone through four different approaches for the design and fabrication of the micro-levitation chip, which are illustrated in Figure 6.4. The first approach, referred to as the *"Si-based Through-hole"*, adopts the same structure of the state-of-the-art chip and adds a through-hole in the center of the top silicon substrate to establish an optical path for imaging. The second approach is the *"Glass-Etch"* and it replaces the top silicon substrate with a glass substrate, where the deep coils groove on the backside is etched using laser. In the third approach, the *"Glass-Cut"*, the top substrate is replaced with a stack of a thin glass substrate carrying the electrodes in addition to a number of laser-cut glass substrates used to form the encapsulation of the coils. Finally, the fourth and final approach, described as the *"Single-Substrate"* or the *"Double-Sided"* approach, simplifies the design and the fabrication process of the chip to a single thin glass substrate carrying the coils on one side and the rotation electrodes on the other side. Switching from one approach to the next was, each time, motivated and driven by the drawbacks and challenges faced. The final *"Double-Sided"* approach is, therefore, presented as an improved process to realize a simplified version of the micro-levitation chip in terms of design and fabrication, which can also benefit other optical and non-optical applications of levitation.

In the following subsections, a detailed description of the fabrication process for each approach is presented, together with an explanation of the challenges that motivated switching to the following approach.

### 6.3.1 Si-based Through-hole Approach

The initial idea to adapt the micro-levitation chip for hyperspectral imaging was to use the same structure reported in the state-of-the-art, consisting of a pyrex bottom substrate for the coils and a silicon top substrate for the electrodes and open a through-hole in the center of the top silicon to provide an optical path for imaging through the chip. This structure is illustrated in Figure 6.5 and the fabrication process is explained in detail below.

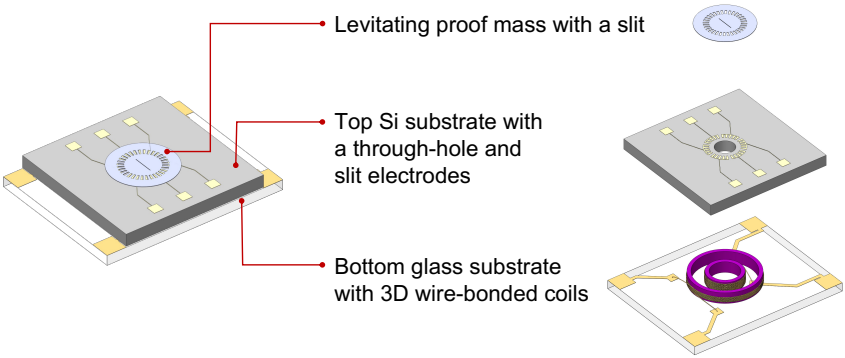


**Figure 6.5:** Construction of the Si-based micro-levitation chip design with a through-hole in the top substrate.

#### 6.3.1.1 Fabrication of Coils Substrate

The fabrication process of the bottom substrate which carries the coils is adopted from the state-of-the-art reported in [108, 109, 122, 135] and consists of three major steps: patterning of the coil pads, fabrication of the SU-8 posts, and 3D winding of the microcoils. The detailed fabrication steps are illustrated in Figure 6.6 and described in the following:

#### Patterning of Coil Pads

The coil pads serve as the electrical contacts to supply the AC current to the two on-chip coils. The inner pads serve as the start and end points for the 3D winding of each coil, while the outer pads are wire bonded to the PCB to connect the coils to the current signal.

(a) *Wafer Cleaning:* a 4-inch glass wafer (MEMpax® borosilicate from SCHOTT AG) with 500 µm thickness is used as the bottom substrate. The top side of the wafer is cleaned using $O_2$ plasma to remove any contaminants from the surface and to improve the adhesion of metal layers during evaporation.

The cleaning is carried out for 10 minutes using the parameters in Appendix A.1.

(b) *Cr/Au Evaporation:* a Cr layer of 20 nm followed by an Au layer of 100 nm are deposited on the cleaned surface using the metal evaporation technique. This forms the seed layer for gold electroplating to form the electrical pads and connectors. The Cr layer is used to improve the adhesion of the gold layer to the glass surface.

(c) *Photolithography of Coil Pads:* in order to form the mold for electroplating the coil pads and connectors, a photoresist layer with 20 µm thickness is deposited on top of the metal layers. The photoresist SU-8 3025 (from Kayaku Advanced Materials Inc.–formally MicroChem Corp.) is spin-coated using the parameters in Appendix A.2. The spin coating is followed by a soft bake at 95 °C for 12 minutes and then photolithography using UV exposure ($\lambda$ = 365 nm and energy density of 400 mJ/cm$^2$). After exposure, the wafer is left for post-exposure bake (PEB) at 95 °C for 4 minutes to harden the exposed resist. To open the mold cavity that will be electroplated, the photoresist is developed using PGMEA for 20 minutes, followed by 10 minutes in isopropanol, and then the wafer is left in an oven at 30 °C for 2 hours for drying. After that, the wafer is kept in a water bath in a vacuum chamber at 50 °C to remove any air bubbles that could be trapped inside the SU-8 mold, which can degrade or even break the electroplated electrical connection to the coils.

(d) *Gold Electroplating:* the wafer is transferred to the electroplating solution ($Au_2S$ with a pH value of 9) to increase the thickness of the gold layer inside the mold cavity from 100 nm to 10 µm. The increased thickness reduces the electrical resistance in the coil pads and connectors and provides more stable and reliable contacts for the following Cu ball-wedge wire bonding during the coil winding. The total electroplated area is 392 mm$^2$ and the

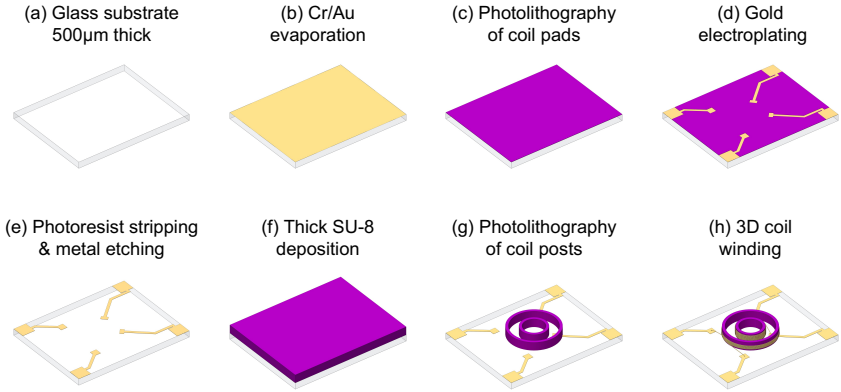


**Figure 6.6:** Fabrication steps of the bottom glass chip with levitation coils.

total duration is 80 minutes, using the electroplating parameters in Appendix A.3, which corresponds to a deposition rate of 125 nm/min.

(e) *Photoresist Stripping & Metal Etching:* after electroplating, the photoresist mold is stripped using $O_2$ plasma (with the R3T machine from MUEGGE GmbH) at 22 °C for one hour and then the wafer is cleaned with isopropanol before drying. After that, the seed layers of Cr and Au are etched away using wet etching. First, a solution of I/KI in distilled water with a ratio of 1:3 is used to etch the Au layer for 1 minute. Then a Cr etch solution (Chromium Etch 200 from NB Technologies GmbH) is used to etch the Cr layer for 130 seconds.

After etching the evaporated metal layers, the first major step is completed and the coil pads and connectors are well defined on the glass substrate, as shown in Figure 6.6(e), and ready for the following wire bonding steps.

### SU-8 Coil Posts

The SU-8 coil posts provide support structures for the 3D coil winding. Two concentric posts are fabricated with inner wall diameters of 2 mm and 3.8 mm for

the inner and outer posts, respectively. The wall thickness of each post is 200 µm. This leaves a gap of 700 µm between the two posts, which is sufficient for the capillary of the wire bonding machine to wind the coils without any collisions. The height of the SU-8 posts is controlled between 600 – 800 µm to accommodate the coil turns and have sufficient tolerance at the bottom for wire bonding and at the top to prevent the coils from snapping out due to vibrations or accidental shocks.

(f) *Thick SU-8 Deposition:* the SU-8 2150 photoresist (from Kayaku Advanced Materials Inc.–formally MicroChem Corp.) is used to fabricate the coil posts. A layer with a thickness of 600 – 800 µm needs to be deposited on the wafer to provide the required height of the posts. Since this thickness cannot be deposited using spin coating, a manual dispenser is used to apply the photoresist to the 4-inch wafer. This corresponds to a volume between 4.9 – 6.5 ml of photoresist. However, a volume between 7 – 9 ml is dispensed to account for losses caused by stiction between the resist and the dispenser and for variation in the resist thickness over the wafer due to surface tension (higher thickness towards the center and lower towards the edge). The SU-8 is dispensed while the wafer is placed on a hot plate at 85 °C. The wafer is then kept on the hot plate at 95 °C for 8 hours to spread the SU-8 more evenly over the wafer and to get rid of any trapped air bubbles.

(g) *Photolithography of Coil Posts:* the next step is photolithography using UV exposure ($\lambda$ = 365 nm and energy density of 1800 mJ/cm$^2$). After that, the wafer is left for post-exposure bake (PEB) for 11 hours, following the temperature curve in Appendix A.4. The photoresist is then developed using PGMEA for 2 hours. This is followed by 15 minutes of isopropanol cleaning.

After the photoresist development, the second major step is completed, and each chip on the wafer has two SU-8 posts standing on top of the coil electrodes, as shown in Figure 6.6(g) and Figure 6.7(b). The posts height is measured using

vertical scanning interferometry (VSI) (Contour ELITE from Bruker) to make sure the required height is achieved before coil winding.

### Coil Winding:

This is the third and final major step in the fabrication of the bottom substrate. The number of turns for the two coils is adopted from the state-of-the-art [108, 135–138], which is 20 for the inner levitation coil and 12 for the outer stabilization coil. This is based on maximizing levitation force and ease of operation while ensuring an operation range below the resonance frequency of the two coils.

The levitation force increases with increasing the number of turns in the coil, as discussed in Section 3.3. However, as the number of turns increases, the distance between the bottommost turn and the proof mass increases, which reduces its contribution to levitation. Consequently, the levitation force saturates and does not increase further with adding more turns. For the ease of operation, the number of turns is chosen to have a matching impedance of the two coils. This allows using the same AC input signal to activate the two coils and reduces the complexity of the electrical setup.

The resonance frequency of the two coils is another important factor since the coil impedance increases dramatically around the resonance frequency, which would require much higher power to drive the coils that can go beyond the limitations of the driving circuits. And when operating in a range higher than the resonance frequency, the coils turn into capacitors instead of inductors and the levitation will not be achieved.

The skin effect is another frequency-dependent factor considered in this context, which increases with the increase in the operating frequency and consequently increases the levitation resistance in the proof mass. For the reported design of the two coils, the resonance frequency was found to be around 100 MHz [108, 136], and therefore a much lower operating frequency of 10 MHz was chosen.

(h) *Coil Winding:* after fabricating the SU-8 coil posts, the wafer is diced into 4 quarters to facilitate the coil winding. A cleaning step using $O_2$ plasma

(100 W) for 5 minutes is performed to remove any contaminants on the surface from previous processing steps and to improve the adhesion of the coil pads prior to wire bonding. The levitation and stabilization coils are then wound around the SU-8 posts on each quadrant of the wafer with a Cu wire with 25 µm diameter using the wire bonding machine (ESEC 3100 Plus) and following the 3D coil winding process outlined in [122, 140–142]. The bond parameters used are summarized in Appendix B.1. Figure 6.7(c) shows a zoom-in view of the two coils after winding around the SU-8 posts. In the final step, each quadrant is diced into single chips, each is 9.2 mm $\times$ 7.2 mm. Figure 6.7(a) shows a complete single chip with the inner and outer coils after dicing.

In order to validate the functionality of the fabricated bottom chips and the coils, sample chips are used to test the levitation of aluminum discs. The chips are placed

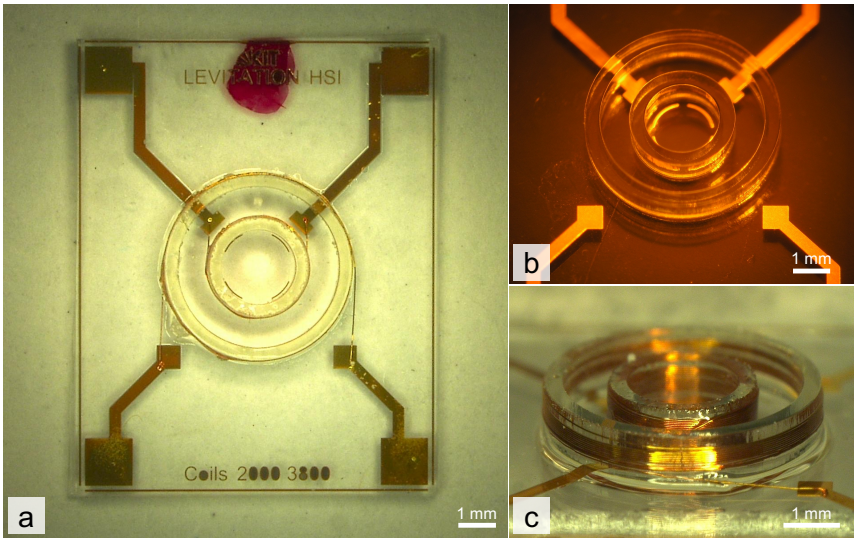


**Figure 6.7:** (a) Complete bottom substrate of the micro-levitation chip with 3D wire-bonded coils after wafer dicing. (b) Zoom-in view showing the SU-8 coil posts after photolithography and resist stripping without coils. (c) Zoom-in view of the 3D microcoils after winding.

on small PCBs with patterned Cu pads and fixed using double-sided adhesive tape. A wire bonding machine (HB05 Wire Bonder from TPT Wirebonder GmbH & Co. KG) with a 50 µm diameter aluminum wire is used to form wedge-wedge bonds to connect the coil pads to the PCB pads, using the parameters in Appendix B.2. A metal wire is then soldered to the PCB pads so that the two coils are connected in series with a phase-shift of 180°. The PCB is then connected to the electrical setup described in Section 6.5.1 to supply the AC input signal to the coils. After all the connections are made, an aluminum proof mass with 3.2 mm diameter is placed on top of the coil posts, using a vacuum tweezer (Polyvac-Pickup from POLYPLAS Hameln GmbH), as shown in Figure 6.8(Left). After activating the coils by supplying the AC signal, the Al proof mass can be seen levitating in Figure 6.8(Right).

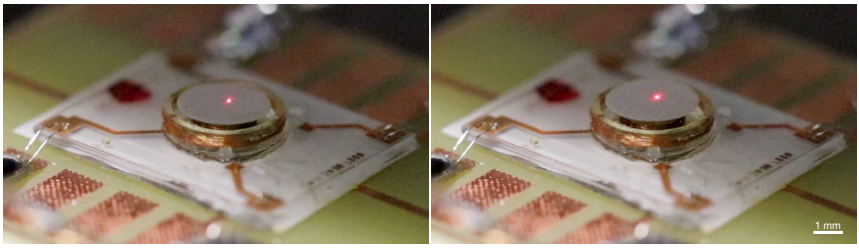


**Figure 6.8:** Validation of the fabricated bottom chip and coils using an aluminum disk as a proof mass. (Left) The proof mass is placed on top of the coil posts. (Right) The proof mass is levitating after activating the coils.

The levitation height is measured as a function of input AC current using a laser sensor (LK-G32 from KEYENCE, Japan). The AC current values correspond to amplitude values in the range of 300 to 400 mV (with $\Delta$V of 20 mV) of the square AC voltage input signal with 10 MHz frequency supplied by the function generator. The rms values of the AC current in the coils are determined by soldering a 100 Ω resistor to the PCB, in series with the two coils, and measuring the voltage across the resistor. Figure 6.9 shows the results where the levitation height increases with increasing the input current. The levitation height is measured with reference to the stationary position of the proof mass on top of the coil posts prior to activating

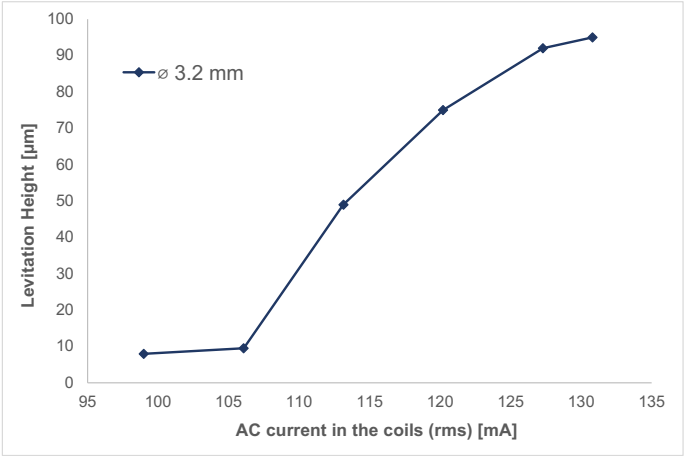


**Figure 6.9:** Levitation height of a 3.2 mm diameter aluminum proof mass at different values of the AC current in the microcoils.

the coils. After validating the functionality of the fabricated bottom chips and coils, the next step is to fabricate the top chip of the rotating slit device to incorporate the slit rotation electrodes while encapsulating the coils and providing an optical path for imaging through the device.

#### 6.3.1.2 Fabrication of Electrodes Substrate

The top chip carries the slit actuation electrodes on the top side and will be assembled with the coils substrate from the bottom side. The fabrication process of the Si-based top substrate is adapted from the state-of-the-art [108, 138, 139] by adding a through-hole in the center of the chip to provide an optical path for imaging. The fabrication consists of three major steps: patterning of the slit actuation electrodes, opening the center hole, and the backside deep etching of the center hole and the groove to encapsulate the coils when assembled with the bottom substrate. The detailed fabrication steps are illustrated in Figure 6.10 and are described in the following:

### Patterning of Slit Actuation Electrodes:

The slit actuation electrodes are used to control the rotation of the levitating slit disc based on the variable capacitance principle, explained in Section 3.4. The design of the rotation electrodes is presented in Section 6.4.1.

(a) *Wafer Cleaning:* a 4-inch silicon wafer with 625 µm thickness and 1 µm thick $SiO_2$ layer on the top side is used. The $SiO_2$ layer serves as an electrical insulator between the electrodes because the Si wafer has low electrical resistivity. The fabrication starts by cleaning the top side of the wafer using $O_2$ plasma.

(b) *Cr/Au Evaporation:* a metal layer consisting of Cr/Au with a thickness of 20/200 nm is deposited using metal evaporation to form the rotation electrodes.

(c) *Photolithography of Slit Electrodes:* the photoresist AZ 1505 (from Micro-Chemicals GmbH) is used to create a mask to pattern the electrodes. The photoresist is spin-coated on top of the Au layer, using the parameters in Appendix A.5, to have a thickness of 1.5 µm. After spin coating, the wafer is placed on the hot plate and kept at a temperature of 95 °C for 5 min. The next step is photolithography using UV exposure ($\lambda$ = 365 nm and energy density of 80 mJ/cm$^2$). After exposure, the resist developer AZ 400K (from MicroChemicals GmbH) is used, in a solution with a concentration of 1:4 (1 part developer and 4 parts DI water), to etch away the exposed resist, since AZ 1505 is a positive resist. The remaining resist provides the electrodes pattern that will serve as a mask during metal etching.

(d) *Metal Etching & Photoresist Stripping:* the metal layers are etched away to leave only the rotation electrodes and their connection pads. First the Au layer is etched by placing the wafer in I/KI solution for 2 minutes. After that, the Cr layer is etched by keeping the wafer in the Cr etch solution for 130 seconds. After metal etching, the remaining photoresist is stripped using a concentrated AZ 400K solution.

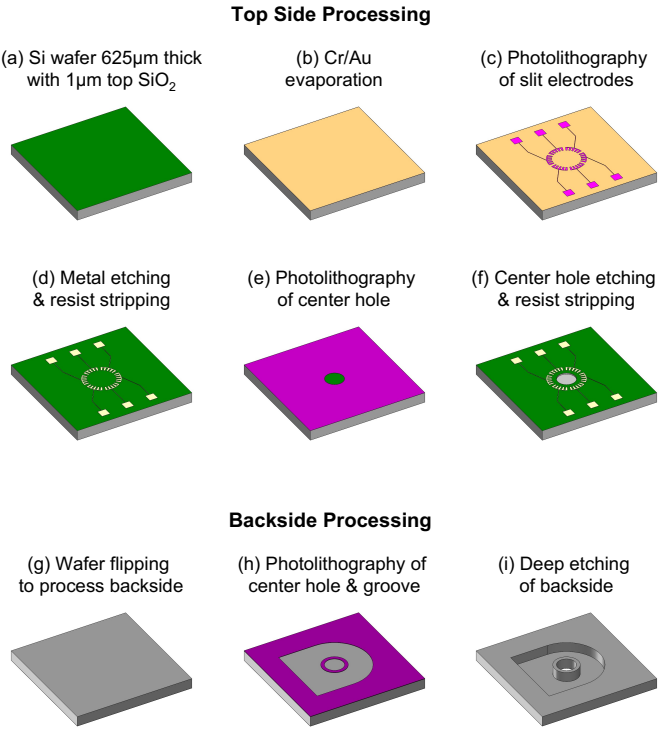


**Figure 6.10:** Fabrication steps of the top Si substrate with topside slit actuation electrodes, a backside deep-etched groove to encapsulate the coils, and a center through-hole for imaging.

### Opening the Center Hole:

After fabricating the rotation electrodes, the next step is opening the center hole for imaging from the top side of the chip.

(e) *Photolithography of Center Hole:* the photoresist AZ 4533 (from Micro-Chemicals GmbH) is used to pattern the mask for opening the center hole. The resist is spin-coated to have a thickness of 5 µm to etch the top $SiO_2$ layer. The spin coating is followed by a soft bake at 95 °C for 5 min to polymerize the resist. The photolithography is carried out using UV exposure

($\lambda$ = 365 nm and energy density of 120 mJ/cm$^2$). This is followed by resist development using AZ 400K with a solution concentration of 1:4. This opens the center hole in the resist layer, which is used as a mask to etch the center hole in the $SiO_2$ layer.

(f) *Center Hole Etching & Photoresist Stripping:* first, the center hole is etched into the $SiO_2$ layer. This can be done using the cryogenic deep reactive ion etching (DRIE) process, using the parameters summarized in Appendix A.6, where etching the 1 µm thickness of the $SiO_2$ layer requires 7 minutes. Another alternative is using wet etching, where the wafer is kept in a buffered hydrofluoric acid (HF) solution for 31 minutes. After opening the center hole in the $SiO_2$, the DRIE etching continues into the silicon to open the center hole to a depth between 70 and 100 µm. After opening the center hole into the $SiO_2$ layer and the bulk Si wafer, the remaining resist on the top side is stripped using a concentrated solution of AZ 400K.

### Backside Deep Etching:

After finishing the top side of the chip, the fabrication continues on the backside to continue opening the center hole through the chip and to open the groove to encapsulate the levitation coils. This deep etching step is important to bring the levitation coils as close as possible to the top surface, after assembly, for the levitation to take effect.

(g) *Wafer Flipping:* before flipping the wafer to process the backside, the top side is covered with a thin layer of photoresist to protect the fabricated electrodes.

(h) *Photolithography of Center hole & Coils Groove:* the photoresist AZ 4562 (from MicroChemicals GmbH) is used to spin-coat a 35 µm thick layer on the backside to be used as mask to pattern the center hole and the coils groove. This is followed by a soft bake at 95 °C for 10 min. After careful backside alignment, photolithography with UV exposure ($\lambda$ = 365 nm and

energy density of 3000 mJ/cm$^2$) is carried out to pattern the resist layer to define the center hole and the coils groove. The resist is developed using AZ 400K with 1:4 concentration.

(i) *Deep Etching & Resist Stripping:* after patterning the resist layer, the next step is to etch the center hole and the coils groove into the backside silicon using cryogenic DRIE to completely open the center hole through the chip and to etch the coils groove to a depth between 585 and 595 µm. This should be sufficient to encapsulate the coils while leaving a 30 – 40 µm device layer to carry the top rotation electrodes. The next step after DRIE is removing the remaining photoresist. The final steps include wafer dicing, cleaning, and then flip chip bonding to assemble the top and bottom substrates together to produce a complete levitation chip.

However, an etching depth of more than 70 µm could not be achieved with the cryogenic DRIE process available at our institute. This limitation, along with the inherent drawbacks of the deep etching process, which requires several hours for each wafer, provided the motivation to go beyond the state-of-the-art and improve the fabrication process. The following subsections present the efforts to achieve this improvement to make the fabrication process simpler, faster, and more compatible with optical applications.

### 6.3.2 Glass-Etch Approach

The first attempt at improving the fabrication process was to replace the top silicon substrate with a glass substrate. The first advantage of this approach is eliminating the need to etch a center hole through the chip since imaging can be done directly through the glass. However the assembly with the bottom chip still requires a deep groove in the top chip to encapsulate the levitation coils. The second advantage of this approach is that etching this groove in glass can be done using laser, which is faster, simpler, and cheaper than the cryogenic DRIE process. Figure 6.11 shows the construction of the all-glass levitation device based on this approach.

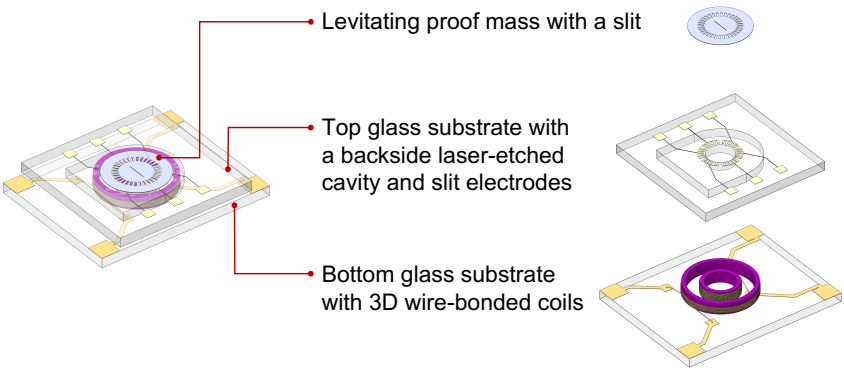


**Figure 6.11:** Construction of the all-glass micro-levitation chip with a laser-etched coils groove in the top substrate.

The fabrication process of this approach consists of the bottom substrate (coils) fabrication, the top substrate (slit electrodes) fabrication, and the assembly of the two substrates together to produce a complete device. The same fabrication process of the bottom substrate, adopted from the state-of-the-art [108, 109, 122, 135], is used as described in Subsection 6.3.1.1. The fabrication of the slit electrodes on the top side of the top substrate follows the steps described in Subsection 6.3.1.2. Instead of the Si wafer, a 4-inch glass wafer (MEMpax® borosilicate from SCHOTT AG) with 500 µm thickness is used. A Cr/Au (20/200 nm) layer is evaporated on the top side and patterned using photolithography and wet metal etching to fabricate the slit rotation electrodes. However, before the fabrication of the slit electrodes, the coil grooves are opened in the backside first using laser etching.

The laser etching is carried out using the Tangerine system (from Amplitude Laser), which has the fixed parameters summarized in Appendix C.1. Three main variable process parameters can be used to control the laser etching, which are the laser power, the cutting speed, and the number of repetitions. The laser power is controlled as a percentage of the total power of the system (29 W). The cutting

speed is the speed at which the laser beam travels across the machined surface (in mm/s). And the number of process repetitions is how many times the laser beam travels the same path across the surface during processing. These parameters affect the etching depth and the quality of the etched grooves and were varied to optimize the outcome of the etching process.

If a low power percentage is used, a higher number of repetitions is needed to reach the required etching depth. With each repetition, the laser removes more glass from the machined surface. Consequently, increasing the number of repetitions increases the etching depth. However, the increased repetitions increase the thermal stresses in the glass and can lead to cracks in the substrate. On the other hand, using a high power percentage can damage the glass and result in holes in the substrate if the laser induced damage threshold (LIDT) is exceeded. The effect of the laser power and the number of repetitions on the achieved etching depth can be found in Appendix C.1. Using a high cutting speed of 1000 mm/s was observed to produce surfaces with better quality and less formation of glass debris. Using higher cutting speeds, however, was found to have negative effects since it requires increasing the repetition cycles which leads to increased thermal stresses and cracks in the glass.

The glass debris, which is glass particles etched by the laser but are redeposited again on the surface during processing, represents a major challenge in this approach. This debris severely degrades the optical quality of the chip and introduces artifacts and noise when imaging through the center part of the chip. Being hard to remove from the surface after processing makes the debris problem even worse.

One method to mitigate the debris redeposition was to apply a protective thin layer of photoresist prior to laser machining and then removing it afterwards. Figure 6.12(a) shows a glass substrate with laser-etched grooves where no protective layer was used, whereas Figure 6.12(b) shows another substrate where a protective layer was applied before machining and then removed after etching the grooves. The protective layer was spin-coated using the photoresist AZ 1505 with a thickness of 1.5 µm (soft bake at 95 °C for 5 minutes). From each substrate, the groove with the highest etching depth, without holes or cracks, is highlighted in

a yellow rectangle and is shown in a magnified view in Figure 6.12(c) and (d), respectively. The glass debris can be seen more clearly in (c), where no protective layer was used. Meanwhile, the use of the protective layer in (d) has reduced the amount of redeposited glass debris. Figure 6.12(e-h) shows the imaging quality through the center part of each groove and the impact of the glass debris on the resulting images. In (e) and (f), the surface of the center cylinder was brought into focus to show the glass debris deposition, while in (g) and (h), the target plane was brought into focus to show the effect of the debris on the image quality. The glass debris can be seen clearly in (e), where no protective layer was used, and

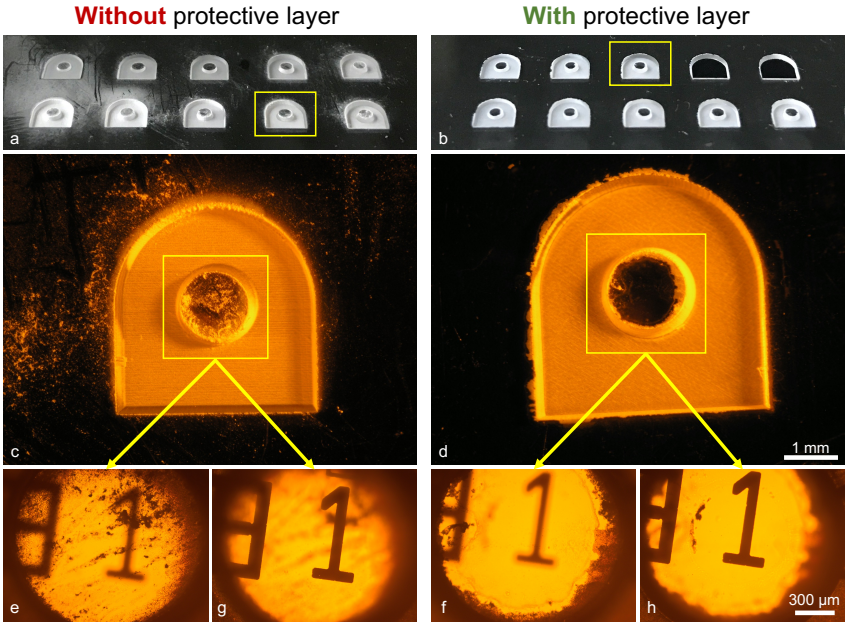


**Figure 6.12:** (Left) Impact of glass debris redeposition during laser etching on imaging quality versus (Right) using a photoresist layer for protection. (a) and (b) depict laser-etched grooves in the two substrates, with the deepest groove highlighted in yellow. (c) and (d) provide magnified views of these highlighted grooves. (e) and (f) demonstrate imaging through the center part with the focus on the top surface to show the glass debris. (g) and (h) focus on the target plane to illustrate the effect of glass debris on imaging quality.

the resulting target image in (g) is heavily degraded by the debris. On the other side, when using a protective layer, the glass debris is reduced in (f) and the target image has less noise in (h). However, while the protective layer has relatively improved the image quality, there is still traces of the glass debris in (f) and (h) affecting the overall quality of the resulting image.

Another challenge faced with the laser etching approach was achieving the desired etching depth. Since the height of the SU-8 coil posts is around 600 µm, the grooves need to be etched to a depth of 450 µm at least, out of the 500 µm thickness of the glass substrate, in order to encapsulate most of the levitation coils. The remaining gap would be then filled with the adhesive material to assemble the top and bottom substrates. However, the etching depth achieved in Figure 6.12(c) was 396 µm, (50% power, 400 mm/s cutting speed, and 12 repetitions) and 384 µm in (d) (70% power, 1000 mm/s cutting speed, and 14 repetitions). This is because increasing the laser power or the number of repetitions, in attempt to increase the etching depth, usually results in cracks and holes in the glass. Due to these challenges, this approach was discontinued in favor of another laser-based approach for the fabrication of the top substrate of the levitation chip, which is the Glass-Cut approach.

### 6.3.3 Glass-Cut Approach

The Glass-Cut approach is based on replacing the thick top substrate with a thin glass substrate to carry the slit rotation electrodes and a stack of glass spacers, with varying thicknesses, to form the groove to encapsulate the levitation coils, as shown in Figure 6.13. Similar to the Glass-Etch approach, this has the advantage of using all-glass substrates which allows for direct imaging through the chip and eliminates the need for costly and time-consuming DRIE etching in silicon. In addition, this approach avoids the laser etching challenges, of glass debris formation and controlling the etching depth, by using the laser to cut the coils groove in a stack of glass spacers.

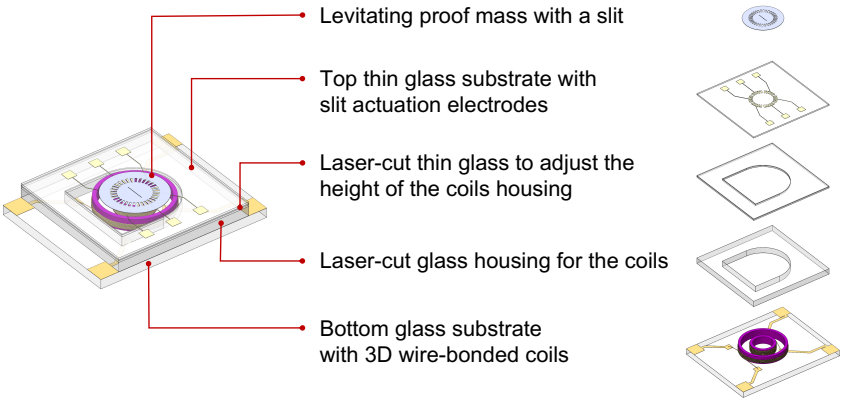


**Figure 6.13:** Construction of the all-glass micro-levitation chip with laser-cut spacers to encapsulate the coils and a thin top substrate for slit actuation.

The fabrication process of this approach starts by fabricating the slit rotation electrodes on the top thin glass substrate. This is done following the same steps described in Subsection 6.3.1.2. A 4-inch glass wafer with 30, 50, or 100 µm thickness (D 263® T from SCHOTT AG) is used instead of the 500 µm-thick wafer used for glass etching. The reason for opting for such thin substrates is to minimize the distance between the rotating slit and the levitation coils in order to maximize the levitation effect. After patterning the Cr/Au layer on the top side using photolithography and wet etching to fabricate the slit rotation electrodes, the glass spacers are fabricated to form the groove for the levitation coils. This is done using laser to cut the shape of the grooves in glass substrates with 50, 100, and 500 µm thickness. These spacers are then stacked on top of each other to match the height of the SU-8 posts and to completely encapsulate the coils when assembled with the bottom substrate. The Tangerine system (from Amplitude Laser) is used again here to cut the glass spacers.

The laser machining parameters for each wafer thickness are given in Table C.2 in Appendix C.2. The top substrate and the spacers are then diced into single chips, as shown in Figure 6.14. After that, the top substrate and the spacers are

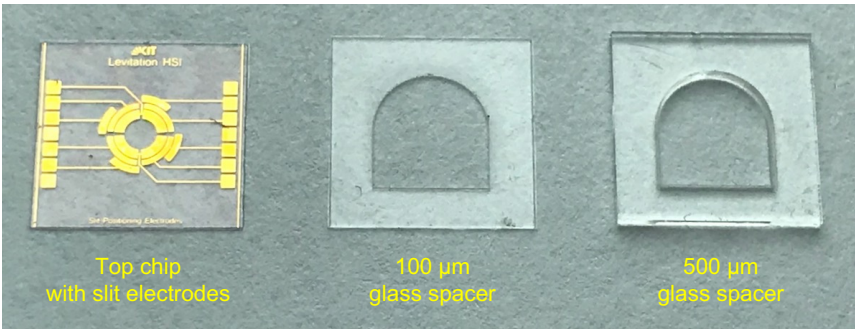


**Figure 6.14:** The top thin glass substrate with slit electrodes after dicing next to laser-cut glass spacers with two different thicknesses of 100 µm and 500 µm, which can be stacked on top of each other to accommodate for variations in the height of the SU-8 coil posts.

assembled with the bottom chip to make a complete levitation device, as shown in Figure 6.15. The number and thickness of the spacer chips used are determined after measuring the height of the SU-8 posts. The chips are assembled together using Urethane resin (Crystal), which is applied to the chips using a syringe and then left to cure at room temperature for 3 to 4 hours.

Despite the advantages of the Glass-Cut approach, there were still a number of disadvantages. First, processing and handling ultra-thin glass substrates with 30 or

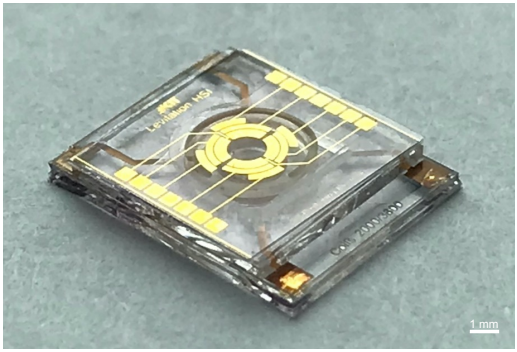


**Figure 6.15:** Assembly of the all-glass micro-levitation device with a thin glass top substrate and laser-cut glass spacers.

50 µm thickness proved to be challenging. For example, the wafers were observed to bend during the post-exposure bake of the photoresist SU-8 3025, as seen in Figure 6.16(Left). In order to avoid the bending, the cooling down from 95 °C to room temperature was slowed down from 12 minutes to 8 hours, which managed to reduce the bending but it was not eliminated completely. Another example is the floating of these wafers on the surface of the etching solution during the wet etching of metal layers. Another problem was the sticking of the wafers to surfaces like the spin coater, the electroplating mount, or the wafer box. This sticking increase the risk of breaking or cracking the wafers, as seen in Figure 6.16(Right), during processing or during transition from one fabrication step to the next. Therefore, the 100 µm was eventually used to fabricate the top substrate. However this increases the distance between the rotating slit and the levitation coils since this wafer thickness is added to the distance between the top turn of the inner coil and the top surface of the SU-8 posts. Taking into account the variation in height in the SU-8 posts, due to manual dispensing of the resist, this distance can increase in a way that affects the levitation range.

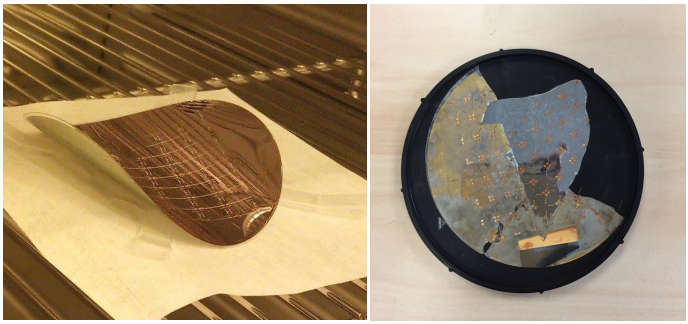

**Figure 6.16:** Challenges in processing and handling ultra-thin glass wafers, with 30 µm and 50 µm thickness, included (Left) wafer bending during photoresist post-exposure bake and (Right) sticking to surfaces leading to cracks and breaking of the wafer.

The other disadvantage of this approach is the increased number of single chips that need to be assembled together to produce a complete levitation device. This increases the time required for the repeated steps of chip alignment, gluing and

curing. This assembly process also needs to be done after measuring the height of the SU-8 posts in order to match that height in the number and thickness of the spacers used. All these problems with this multi-chip device assembly inspired the new fabrication approach described in the following subsection.

### 6.3.4 Single-Substrate Approach

The Single-Substrate approach represents the fourth and final approach in this thesis in the pursuit to develop an optically compatible micro-levitation chip. This approach overcomes the challenges discussed in the previous subsections and simplifies the fabrication process in a way that can benefit other optical and non-optical applications of micro-levitation.

A single thin glass substrate is used to carry the slit rotation electrodes on one side and the levitation coils on the other side, as illustrated in Figure 6.17. This immediately eliminates the cumbersome process of etching a deep groove to encapsulate the coils, whether using DRIE in silicon or using laser in glass. This also means there are less constraints on the height of the SU-8 posts of the coils. The height needs only to be sufficient for winding the prescribed number of coil turns. But the exact height is no longer critical, which relaxes the need for precise control over the SU-8 dispensing volume and also reduces the need to measure the height of the posts before assembling each chip. The use of a single substrate also removes many of the intricate and time-consuming steps associated with the assembly process in the previous “multi-chip” approaches, including chip alignment, bonding, and curing. In addition, winding the levitation coils starting from the bottom side of the chip means the distance between the top turn of the coils and the proof mass is consistently defined only by the substrate thickness and the offset between the wafer surface and the starting point of coil winding. This means the levitation height is no longer affected by variations in height of the SU-8 posts or other variations during assembly.

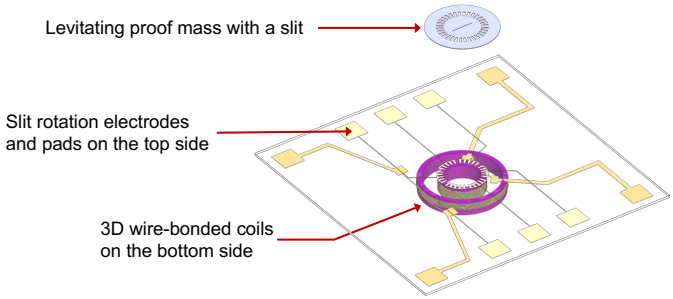


**Figure 6.17:** Illustration of the single-substrate thin glass chip with slit electrodes on the top side and levitation coils on the bottom side.

The fabrication process is modified from that described in the previous subsections. All the steps associated with the encapsulation groove and the assembly are removed, while the rest of the process is adapted to meet the considerations of fabricating on both sides of the wafer. The fabrication steps are illustrated in Figure 6.18 and are explained in detail in the following:

(a) *Wafer Cleaning:* a 4-inch (100 mm) borosilicate glass wafer (D 263® T from SCHOTT AG) with 100 µm thickness is used as the single substrate that will carry the slit electrodes on one side and the levitation coils on the other. The wafer is cleaned using $O_2$ plasma for 10 minutes to remove any contaminants and to improve the surface adhesion prior to metallization.

(b) *Cr/Au Evaporation on Both Sides:* the seed layers for the slit electrodes and for the coil pads are deposited on both sides of the wafer using metal evaporation. A layer of Cr with 20 nm thickness is deposited first on the glass to improve its adhesion to gold. This is followed by a 60 nm Au layer deposited on top of the chromium.

#### 6.3.4.1 Top Side Processing:

After cleaning the wafer and evaporating the metal seed layers, the fabrication begins by processing the top side of the wafer, where the rotating slit will be placed.

(c) *Slit Electrodes Patterning:* similar to Subsection 6.3.1.2, the photoresist AZ1505 (from MicroChemicals GmbH) is spin-coated to a thickness of 1.5 µm, followed by a soft bake at 95 °C for 2 minutes. The photolithography is carried out using UV exposure ($\lambda$ = 365 nm and energy density of 80 mJ/cm$^2$). After that, AZ 400K developer with 1:4 concentration is used for 30 sec to remove the exposed resist, since AZ1505 is a positive resist. The remaining resist provides the mask for patterning the slit electrodes.

(d) *Gold Etching & Resist Stripping:* the gold etching in this process is carried out using dry etching, instead of the wet etching, described earlier in 6.3.1.2. This is due to the presence of another gold layer on the other side of the wafer that is yet to be processed. Therefore, to avoid damaging the backside gold layer, the reactive ion etching (RIE) process is used. An Argon plasma (100 W) is applied for 20 minutes using the Etchlab 200 machine (from SENTECH Instruments GmbH). After that, the wafer is cleaned with acetone and isopropanol before stripping the resist mask using $O_2$ plasma for 10 minutes.

#### 6.3.4.2 Bottom Side Processing:

After gold etching, the wafer is flipped to process the backside. At this point, only the Cr seed layer remains without processing on the top side. However, this will be etched together with the Cr layer on the bottom side.

(e) *Photolithography of Coil Pads:* the photoresist SU-8 3025 (from Kayaku Advanced Materials Inc.–formally MicroChem Corp.) is spin-coated to a thickness of 20 µm, similar to Subsection 6.3.1.1, to pattern the mould for

electroplating. This is followed by a soft bake at 95 °C for 12 minutes and UV exposure ($\lambda$ = 365 nm and energy density of 400 mJ/cm$^2$), and a post-exposure bake (PEB) at 65 °C for 30 minutes. The wafer is cooled gradually to avoid stresses and cracks by placing it on a preheated plate at 45 °C and then switching off the hot plate and leaving the wafer to cool for 10 minutes before moving it away from the plate to cool to room temperature. After that, the resist is developed using PGMEA for 20 minutes and then the wafer is placed in an oven at 30 °C for 2 hours for drying.

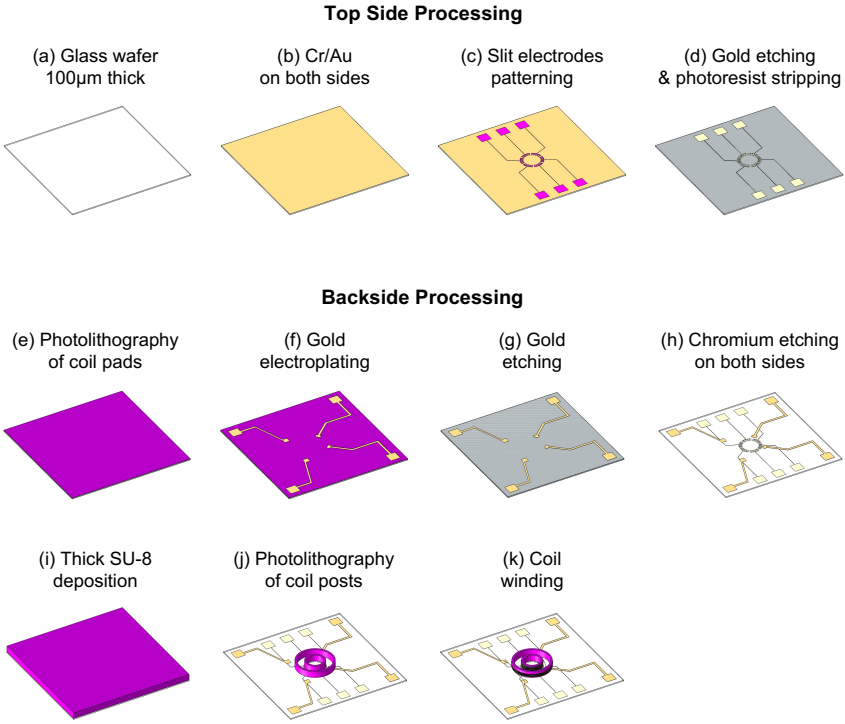


**Figure 6.18:** Fabrication steps of the single-substrate thin glass chip with silt rotation electrodes on the top side and levitation coils on the bottom side.

(f) *Gold Electroplating:* before placing the wafer in the electroplating solution, the wafer is fixed to a holder and placed in a vacuum oven to remove any residual bubbles that can get trapped in the electroplated layer and degrade its conductivity. Similar to 6.3.1.1, the electroplating is used to increase the thickness of the coil pads and connectors to 10 µm to increase their conductivity and to improve the forming of the ball-wedge bonds during wire bonding.

(g) *Resist Stripping & Gold Etching:* the photoresist mould is stripped with $O_2$ plasma (1200 W) for 2 hours using the R3T machine (from MUEGGE GmbH). After that, the wafer is placed in an Acetone bath to remove any remaining SU-8 residues and then cleaned with isopropanol. Dry etching is used again here, instead of wet etching, to etch the Au seed layer without damaging the slit electrodes on the other side.

(h) *Chromium Etching on Both Sides:* at this point, the wafer has the slit electrodes on the top side and the coil pads and connectors on the bottom side. However, both sides are still covered with seed Cr layer. Both layers can now be etched using Cr Etch 200 (from NB Technologies GmbH) for 10 minutes. Etching both layers simultaneously make it easier to detect when the Cr is completely etched since the glass wafer becomes transparent again once the Cr is removed.

(i) *Thick SU-8 Deposition:* the SU-8 2150 is used, similar to 6.3.1.1, to form the coil posts. A volume between 7 – 9 ml is manually dispensed using a pipette to achieve a height between 600 – 800 µm for the posts. The precise control of the posts height is no longer critical in the single-substrate approach since there is no subsequent assembly steps that will bring the posts inside a closed cavity. The wafer is placed on the hotplate, which is gradually heated to 85 °C over 30 minutes. The temperature is stalled for 15 minutes, during which the dispensing is carried out to distribute the resist evenly over the

wafer surface. After dispensing, the temperature is increased to 95 °C and the wafer is kept at this temperature for 8 hours before exposure.

(j) *Photolithography of Coil Posts:* the wafer is exposed with UV ($\lambda$ = 365 nm and energy density of 1800 mJ/cm$^2$). This is followed by a long cycle of post-exposure bake where the temperature is slowly increased from 22 °C to 65 °C over 15 hours, maintained at 65 °C for 10 hours, and then gradually decreased to 22 °C over 10 hours. This slow heating and cooling is to avoid stresses and cracks in the thin glass wafer, which is more fragile than the thicker wafers used earlier. After that, the resist is developed using PGMEA for 75 minutes. After cleaning with acetone and isopropanol, the wafer is placed in an oven to dry for 1 hour. At this stage, the coil posts are robustly formed and ready for coil winding.

(k) *Coil Winding & Wafer Dicing:* in the final step, the levitation and stabilization coils are wound around the SU-8 posts using the automatic wire bonder ESEC 3100 Plus and a 25 µm diameter Cu wire following the 3D coil winding process outlined in [122, 140–142] and the bond parameters in Appendix B.1. Before coil winding, the wafer is diced into 4 quadrants using the laser machine PIRANHA® II (from ACSYS Lasertechnik GmbH). This represents another advantage for the single-substrate thin glass approach since dicing with laser is more precise, faster, and cleaner than conventional wafer dicing where the thin glass wafer needs to be glued to a thicker carrier wafer, which makes it difficult to separate the two wafers and the single chips later on. After coil winding, each quadrant is diced into single chips using the same laser machine.

Figure 6.19 shows a complete single chip (12.5 mm × 12.5 mm) based on the single-substrate approach after coil winding and dicing. This chip represents a complete device for levitating and rotating a proof mass and offers a more compact, simpler, and optically compatible form compared to the state-of-the-art. The next

subsection presents the design and fabrication of the rotating slit disc to be used with this chip.

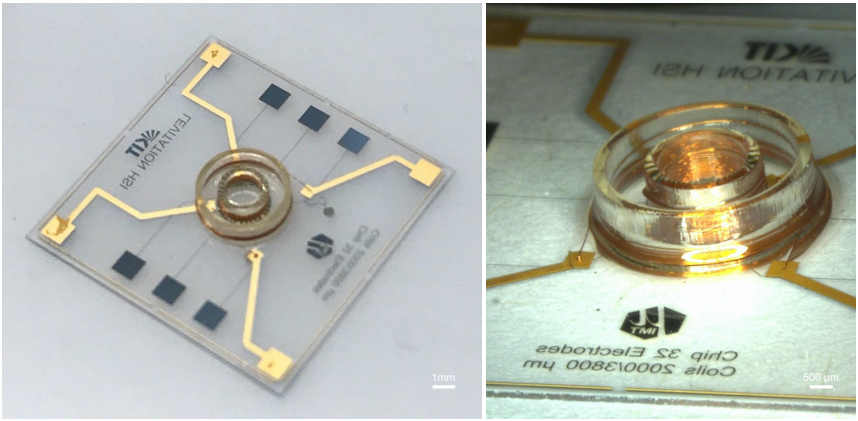

**Figure 6.19:** Thin glass single-substrate micro-levitation chip after coil winding and dicing (Left) with a zoom-in view of the two coils (Right).

## 6.4 Rotating Slit

The rotating slit is made of a conductive non-magnetic metal disc with a slit opening surrounded by a circular array of actuation electrodes. In this thesis, aluminum is used due to its high conductivity and low density, which allows higher levitation for the same disc volume and input signal compared to other metals like copper. Using the chip described in the previous section, the slit disc can be levitated and rotated in a frictionless controlled manner to sequentially scan a chosen field of view during hyperspectral imaging. The working principle is based on electromagnetic induction, explained in Section 3.3, and electrostatic actuation, explained in Section 3.4. The following subsections present the design of the rotation electrodes and the fabrication of the slit disc.

### 6.4.1 Design of Rotation Electrodes

The rotation electrodes includes the slit (rotor) electrodes and the chip (stator) electrodes. The rotation of the slit disc is achieved by the sequential activation of the stator electrodes, following the variable capacitance principle explained in Section 3.4. The design of the stator and rotor electrodes defines the stepping motion of the rotating slit and consequently affects the data acquisition during hyperspectral imaging. This includes the number of angular positions of the slit and the resolution of the step angle between each contiguous positions. The design of the electrodes also needs to ensure the levitation of the slit disc can still be achieved.

Levitation is a prerequisite step to enable the slit rotation in a frictionless manner. Therefore, the openings in the metal disc defining the slit aperture and the rotation electrodes need to avoid disrupting the eddy currents induced in the disc to generate levitation. From the work of Lu et al. [108, 143], the distribution of the eddy current density is concentrated above the inner coil (radius of 1.2 mm) and at the outer rim of the levitating disc (radius of 1.6 mm), whereas the center area contributes less than 1% of the levitation force. This allows the placement of

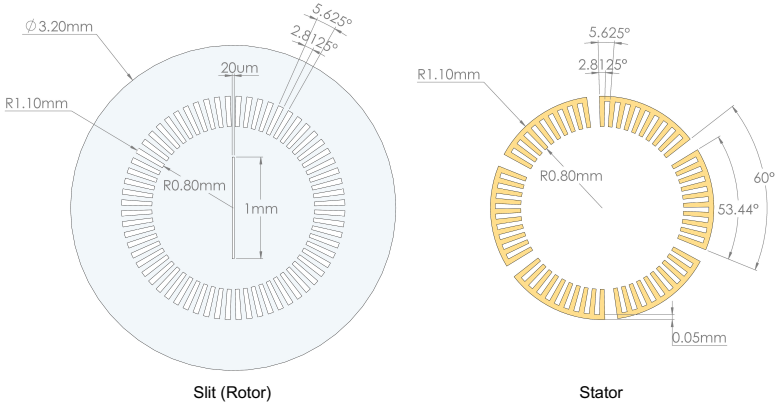


**Figure 6.20:** Design of 64-electrode rotating slit and the corresponding three-phase stator electrodes.

the slit opening in the center part. As shown in Figure 6.20, the slit has a width of 20 µm and a length of 1 mm, similar to that used in Chapters 4 and 5. The slit electrodes are designed to have an outer radius of 1.1 mm, which is smaller than that of the inner coil to allow the flow the eddy currents. The inner radius is 0.8 mm to maximize the electrodes area and consequently the electrostatic force for rotation.

The number of slit electrodes is defined in accordance with the slit width to ensure that a complete rotation of the slit disc provides a full scan of the field view to avoid any loss of data during hyperspectral imaging. This can be achieved when the step angle $\theta_s$ of the rotating slit is not larger than the arc angle $\theta_{\text{SlitArc}}$ defined by the slit width, which is given by:

$$\theta_{\text{SlitArc}} = 2 \times \arctan\left(\frac{\text{Slit Width}}{\text{Slit Length}}\right) = 2.29^\circ \tag{6.1}$$

Using the rotor and stator design shown in Figure 6.20, a step angle $\theta_s$ of 1.875° can be achieved as demonstrated in Figure 6.21. The slit disc (rotor) in this design has 64 equidistant electrodes. The stator has 60 electrodes divided into 6 groups with each two opposite groups forming one of the three phases of the stepper motor, as shown in Figure 6.21. The mismatch in the number of electrodes between the rotor and the stator results in partial overlap between the rotor electrodes and the following phase of the stator in the activation sequence, which corresponds to the step angle.

The stepwise rotational motion of the slit disc following the sequential activation of the stator electrodes is illustrated in Figure 6.21, where a ring with a width of 100 µm is cut through the slit electrodes to reveal the alignment with the underlying stator electrodes in each position. In the initial position (a), the slit electrodes are aligned with the active phase (1) of the stator and the slit is vertically aligned. The remaining slit electrodes show partial alignment with the other two phases, which results in a higher resolution stepping motion. In position (b), phase (2) is activated and the slit rotates with the step angle of 1.875° to align its electrodes

with those of the active phase. The same happens in positions (c) and (d), where activating phase (3) and then phase (1) rotates the slit with an additional step angle each time to angular positions 3.750° and 5.625°, respectively. By continuing the sequential activation of the three phases, the slit can be rotated through 180° to cover a full scan of the field of view.

### 6.4.2 Fabrication

The slit disc is fabricated from an aluminum foil with 10 µm thickness (from Advent Research Materials Ltd) using laser cutting. First, the foil is flattened with a press and then applied to a 4-inch wafer that acts as a holder. After that, the wafer is placed in the laser cutting machine (Tangerine system from Amplitude Laser) and the slit disc design is cut into the aluminum using the parameters summarized in Appendix C.3. Figure 6.22 shows different versions of the slit disc after laser cutting, which are fabricated to test the electrostatic rotation using different numbers of slit electrodes.

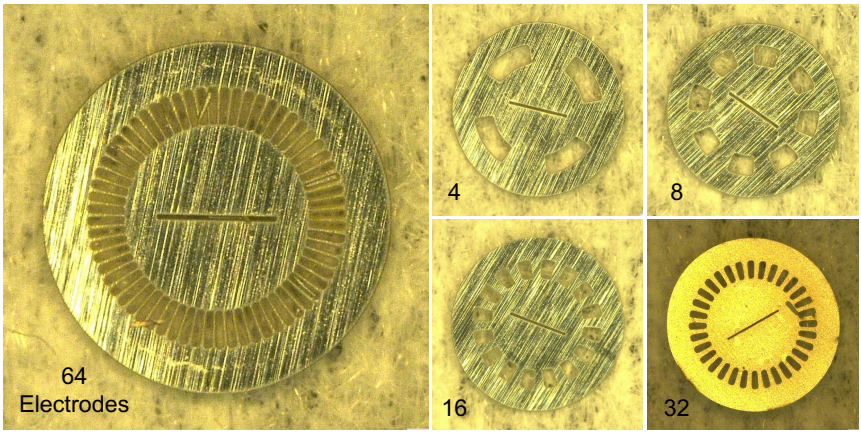


**Figure 6.22:** Different versions of the Al rotating slit with different numbers of actuation electrodes (4, 8, 16, 32, and 64) were fabricated using laser cutting.

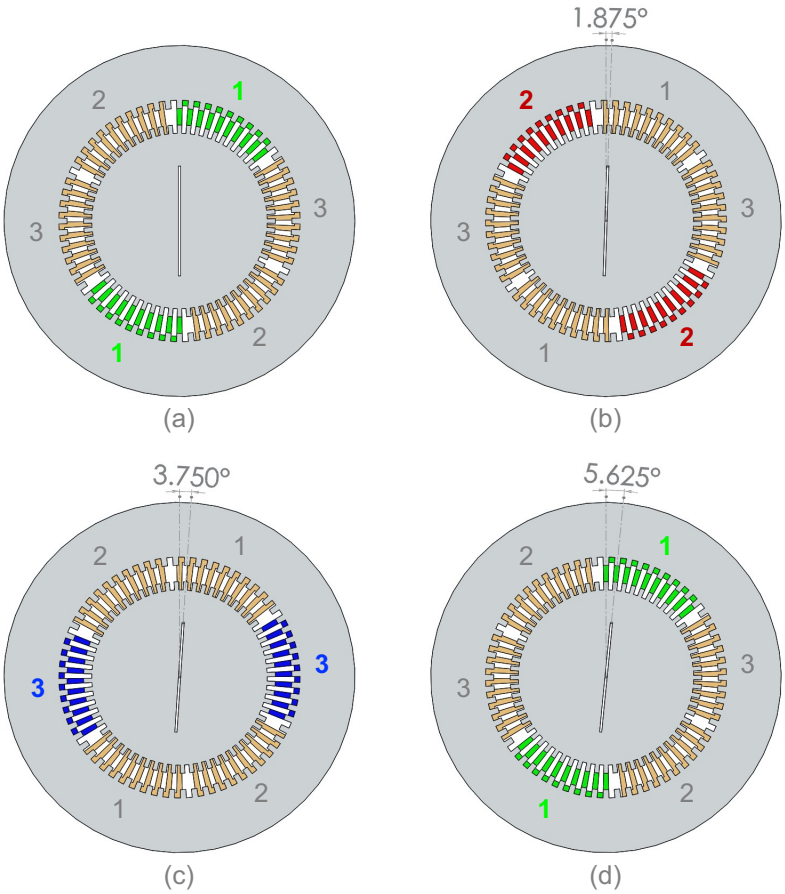


**Figure 6.21:** Rotation of the 64-electrode slit through the sequential activation of the three phases of the stator (chip) electrodes. A ring with 100 µm width is cut through the slit electrodes to reveal the alignment with the underlying stator electrodes. (a) Initial position where the slit is aligned vertically when phase 1 is active. (b) Phase 2 is activated and the slit rotates with the step angle 1.875°. (c) Activating phase 3 and (d) activating phase 1 again rotates the slit with an additional step angle each time to 3.750° and 5.625°, respectively.

## 6.5 Validation

The first step in the experimental work involving the newly fabricated chips and slit discs is validating their functionality to ensure they are free from any defects and that levitation can be established. This begins by establishing the experimental setups described in Sections 6.5.1–6.5.3 and then followed by the levitation validation in Section 6.5.4.

### 6.5.1 Electrical Setup

The electrical setup used for levitation is shown in Figure 6.23. An arbitrary signal generator (HMF2525 from Rohde & Schwarz, Germany) is used to generate a square AC signal, which generates the time-varying electromagnetic field that

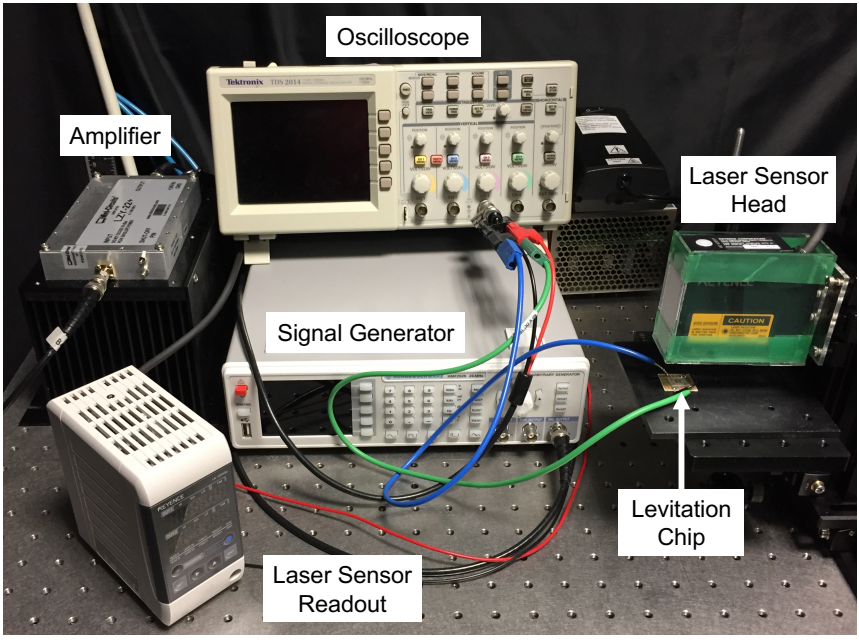


**Figure 6.23:** Electrical setup to generate the AC signal to activate the levitation coils and test the micro-levitation chips and slit discs

induces the eddy currents in the slit disc. A signal frequency of 10 MHz is chosen to be far below the resonance frequency of the coils around 100 MHz, as reported in [108, 136]. The signal is amplified using the amplifier LZY-22+ (from Mini-Circuits, USA), which is powered with a DC power supply (DRP-240-24 from Mean Well, Taiwan). The output signal of the amplifier is connected to the PCB where the levitation chip is mounted. The coil pads are connected to the PCB pads, using wire bonding or conductive adhesive. The connection is made so that there is a phase-shift of 180° between the two coils. This is done by connecting the amplifier output with one pad of the inner coil and one pad of the outer coil while connecting the other two pads of the inner and outer coils together with a wire in a way that the electric current direction in each coil is opposite to the other coil. This can be seen in Figure 6.24, where this connection was incorporated in the PCB. An oscilloscope (TDS2014 from Tektronix, USA) is connected in parallel to the levitation coils to measure the signal during levitation. The laser sensor LK-G32 and the readout unit LK-GD500 (from Keyence, Japan) are used to measure the levitation height of the aluminum slit disc.

### 6.5.2 PCB

The design of the PCB used to mount the single-substrate double-sided levitation chip is shown in Figure 6.24. The PCB has four pads that align with the coil pads and a drilled through-hole for inserting the coil posts, when mounting the chip, as seen in Figure 6.24(c) and (d). This allows for imaging through the chip while also protecting the coils since the PCB thickness is larger than the height of the coil posts. The PCB pads and the coil pads are connected using an adhesive conductive silver paste (L100 from Keno Electronic GmbH, Germany). The levitation signal from the amplifier is supplied to the PCB through port (E), which is connected to one pad of the inner coil and one pad of the outer coil. Two Vias at points (1) and (2) and the backside connector in between (seen in Figure 6.24(b) and (d)) connect the remaining two pads of the inner and outer coils in a way that reverses the current direction between the two coils and therefore creates a phase-shift of 180°,

which is required for levitation. Port (3) is the input point for the electrostatic signal for slit rotation, where each line is used to connect one of the three phases of the motor. The PCB pads are connected to the slit actuation pads on the chip by means of wire bonding using the HB05 machine (from TPT Wirebonder GmbH & Co. KG) and a 50 µm diameter Al wire. The adjacent electrodes of each phase are connected together via point (4) and the connection lines between (3) and (4) on

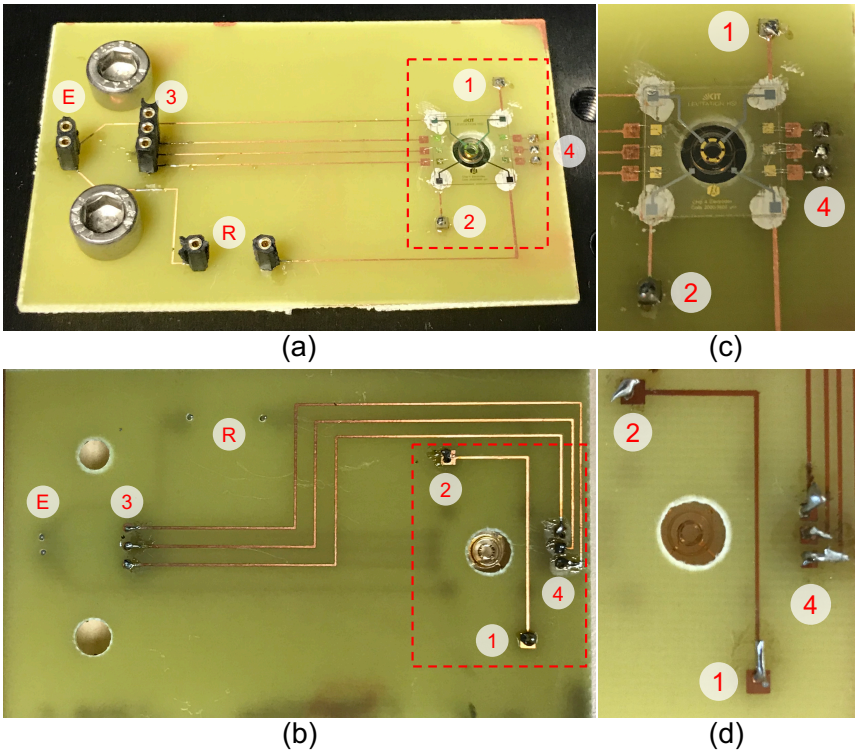


**Figure 6.24:** The PCB used to mount the levitation chip shown from the top side (a, c) and from the bottom side in (b, d), where (c) and (d) show a magnification of the dotted squares in (a) and (b). The PCB provides the electrical levitation signal through point E and the electrostatic rotation signal through points 3 and 4. The Vias at points 1 and 2 and the backside connection between the two establishes the 180° phase-shift between the two coils. A resistor is inserted at point R, which is used to measure the AC current in the circuit.

the backside, as shown in Figure 6.24(b). Port (R) is used to insert a resistor, in series with the coils, to facilitate the measurement of the AC current by measuring the voltage across the resistor. The PCB is fabricated using photosensitive copper boards (from CIF, France).

### 6.5.3 Optical Setup

The optical setup is constructed to test the imaging performance of the miniaturized rotating slit device in spatial and spectral modes. The setup is adapted from that used in Chapter 5 to demonstrate the rotational-scan concept. However, The setup is mounted in a vertical position, as shown in Figure 6.25, to accommodate the micro-levitation chip and the slit disc and prevent it from falling off. The chip and the slit disc, together, form the miniaturized rotating slit device that is mounted on a PCB and positioned in the system to replace the commercial rotating slit mechanism (from Thorlabs) that was used earlier. The PCB is fixed to a 3-axis precision platform to facilitate the precise positioning of the chip in the intermediate image plane of the system's front optics. As described in Chapter 5, the front optics combine a wide angle machine vision lens (3.5 mm EFL, product no. MVL4WA, Thorlabs, USA) and an f60 biconvex lens. A microscope objective (GF Planachromat 12.5×/0.25, Zeiss Jena, Germany) is placed behind the slit to collimate and magnify the image line selected by the slit and project it on the Dove Prism (Thorlabs No. PS992M-A). The Dove prism is mounted on a rotational stepper motor (Thorlabs No. K10CR1). The CCD camera (DMK 23U274 for monochrome or DFK 23U274 for color, from The Imaging Source, Germany) is coupled with an objective lens (Xenoplan 2.8/50-0902, Schneider Kreuznach, Germany) and used to record the images. In the spectral imaging mode, the grating (300 lines/mm – Thorlabs No. GT13-03) is inserted between the Dove Prism and the CCD camera, while the camera is rotated to the angle of the first diffraction order.

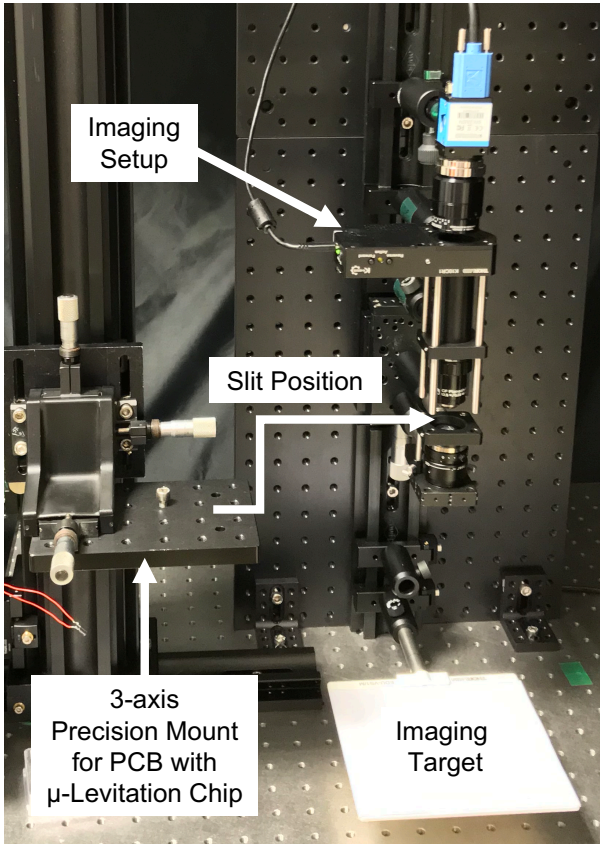


**Figure 6.25:** Optical setup for testing the miniaturized rotating slit device in scanning a target image in spatial and spectral modes

### 6.5.4 Levitation Validation

The levitation measurements are carried out using the single-substrate double-sided micro-levitation chip, which is mounted on the PCB and connected as described in the previous subsections. A sample slit disc with 3 mm diameter and 8 electrodes is placed on top of the chip as shown in Figure 6.26(Left). The function generator is used to generate a square AC signal with an amplitude of

450 mV and a frequency of 10 MHz, which is amplified and supplied to the coils via the PCB. When the levitation signal is switched on, the slit disc levitates, as shown in Figure 6.26(Right). A levitation height of 120 µm was measured using the laser sensor. This provides validation for the functionality of the new levitation chips based on the single-substrate approach. This result also provides validation that incorporating the slit aperture and the rotation electrodes in the aluminum discs does not disturb the induction of eddy currents, required for levitation. This opens the door for using these new designs for upcoming work, and also for future applications of electromagnetic inductive levitation.

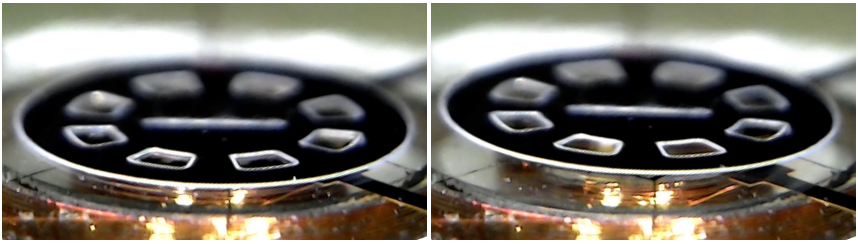

**Figure 6.26:** Levitation validation using the single-substrate micro-levitation chip and a 3 mm diameter slit disc with 8 rotation electrodes. (Left) The slit disc is placed on the levitation chip mounted on the PCB. (Right) The slit disc is levitating after supplying the AC signal to the coils.

## 6.6 Conclusions

This chapter presented the development of a new all-glass single-substrate micro-levitation chip for the levitation and rotation of a miniaturized slit disc, based on the principles of electromagnetic inductive levitation and electrostatic actuation. This represents the initial step towards the miniaturization of the rotational-scan hyperspectral imaging system, presented in Chapter 5, where the rotating slit mechanism is a key component.

The new chip was realized through a series of improvements to the micro-fabrication process of the state-of-the-art micro-levitation devices, based on the configuration consisting of two concentric 3D wire bonded microcoils for levitation and stabilization. The improvements aimed at overcoming the limitations

of the state-of-the-art, which consisted of a top silicon substrate and a bottom glass substrate assembled together. The limitations included the absence of an optical path for imaging though the chip, the time-consuming deep reactive ion etching (DRIE) in silicon, the need to control and match the height of coil posts and the depth of coil grooves, and the intricate alignment and bonding of the two substrates together.

Different approaches were pursued, in this thesis, to overcome these limitation including the deep etching of a through-hole in the top silicon substrate, the replacement of the top silicon substrate with a glass substrate with laser-etched coils groove, and the combination of multiple laser-cut glass substrates to replace the top silicon substrate and encapsulate the coils. However, these approaches still suffered from the same limitations to varying extents and in some cases introduced other downsides like the redeposition of glass particles during laser etching, which degraded the optical quality of the chip.

The successful approach was based on a thin single glass substrate with fabrication on both sides (double-sided). The fabrication of the coils on one side and the rotation electrodes on the other side led to an improved, faster, and simplified microfabrication process. The resulting new chip is 100 µm in thickness with dimensions of 12.5 mm $\times$ 12.5 mm and having a clear optical path for imaging through the chip. The inner and outer 3D microcoils with 20 and 12 windings, respectively, are fabricated with an automatic wire bonder using a Cu wire with 25 µm diameter. Different versions of a three-phase rotating slit disc with different numbers of rotation electrodes, corresponding to different numbers of slit positions, were fabricated with laser cutting using an aluminum foil with 10 µm thickness. The successful demonstration of levitation using the new thin glass chip, and the slit discs, provides validation for the new microfabrication approach and opens the door for more optical, and non-optical, applications for micro-levitation.

# 7 Conclusions & Future Work

This chapter provides a comprehensive summary of the results obtained in the course of this thesis and highlights potential future advancements. Section 7.1 distills and consolidates the findings from the different thesis chapters. Section 7.2 proposes future research directions in relation to the concepts introduced in this work and also in relation to other initiatives that have emerged during the course of this research.

## 7.1 Conclusions

The motivation behind this thesis was to unlock the potential of hyperspectral imaging technology in the public health domain. Among the various techniques for hyperspectral data acquisition, the spatial-scan technique was identified as the optimal candidate for applications in this domain. This is owing to its ability to provide high spatial and spectral resolution across a wide spectral range. This satisfies a crucial criterion of health-related applications, which require the detection of intricate features and details pertaining to sensitive health conditions. Therefore, the work of this thesis was focused at overcoming the limitations of existing spatial-scan systems that prevent their adoption on a wider scale. These limitations include restricted flexibility and adaptability due to the prevailing reliance on static components, resulting in an inherent dependance on relative motion between the system and the target for data acquisition, and the limited progress in miniaturization to provide mobile and affordable systems.

Two novel spatial-scan systems were introduced in this thesis, adopting an "inside approach" in design and construction by employing internal active components. The first system combined an internal line-scanning unit, consisting of a slit

mounted onto a linear piezoelectric motor, and a rotating camera mechanism. This enabled a dual-mode system that can switch between spatial and spectral imaging and can scan the target image without any relative motion. A novel feed-forward compensation function was programmed into the control software to automatically synchronize the motion of active components during data acquisition in a way that compensates for the shift in the diffraction angle resulting from the slit lateral movement. This has preserved the spectral calibration of the system and ensured utilizing the maximum area of the image sensor and the maximum scanning range. This was reflected in the demonstrated high spectral resolution of 2 nm, which is comparable to the state-of-the-art and well-suited for a wide range of applications. The enhanced performance and flexibility of this system is also reflected in the possibility to adapt the acquisition parameters such as scanning speed or the selection of specific regions of interest.

The second system in this thesis expands the range of spatial-scan techniques, that includes the pushbroom (line-by-line) and the whiskbroom (point-by-point), by introducing a novel rotational-scan technique. This was achieved by combining a rotating slit and a rotating Dove prism, where the slit rotation scans the target image and the concurrent Dove prism rotation realigns the transmitted light with the diffraction grating to prevent spectral crosstalk and facilitate the extraction of spectral information. While the precise alignment of the rotating components proved to be critical, this combination still demonstrated high spatial resolution of 250 µm and high spectral resolution of 2 nm while enabling higher flexibility by eliminating the relative motion during data acquisition.

The miniaturization work in this thesis was focused on the rotating slit mechanism as an initial step towards the overall miniaturization of the rotational-scan system. A new chip was developed based on the principles of electromagnetic inductive levitation and electrostatic actuation to levitate and rotate an aluminum disc with a slit aperture. The state-of-the-art configuration of two concentric 3D wire bonded microcoils for levitation and stabilization was adopted, and an improved microfabrication process was developed. The improved process enabled the realization of the new chip on a single 100 µm thin glass substrate with features

incorporated on both sides (double-sided) to overcome the limitations associated with state-of-the-art micro-levitation devices. Unlike the state-of-the-art, the new chip is well-suited for optical applications, providing an optical path for imaging through the glass. The single-substrate and double-sided approach eliminated the laborious processing steps involving deep etching, precise control of the coil posts height, chip alignment, and bonding of multiple substrates, which are encountered in the state-of-the-art devices. The new chip, measuring 12.5 mm $\times$ 12.5 mm, features the coils on one side and the slit actuation electrodes on the other side. The slit discs were laser-cut from a 10 µm thin aluminum foil to have patterned electrodes resembling a three-phase motor. Successful levitation using the new glass chip and slit discs was demonstrated, paving the way for more applications in the future.

While the results obtained in this thesis signify advancements in spatial-scan hyperspectral imaging systems and a progress towards system miniaturization, further developments are necessary to fully realize the potential of this technology and achieve a widespread adoption in public health applications. These prospective future developments are discussed in the subsequent section.

## 7.2 Future Work

The envisaged future research following the work of this thesis is more dedicated towards miniaturization. The development of the glass micro-levitation chip to drive a levitating rotational-scanning slit is an initial step. Continued development and extensive characterization of this slit mechanism are still necessary to bring higher maturity and application readiness, as discussed in Subsection 7.2.1.

While the main focus, in this thesis, was on the spatial-scan technique, other innovative approaches were also explored within this research, resulting in the creation of new project proposals. One approach, developed in collaboration with Furtwangen University, involves the realization of a levitating filter wheel based on porous silicon optical filters as a key element for a miniaturized multispectral imaging system, as explained in Subsection 7.2.2. Another approach, in collab-

oration with two institutes at KIT, proposes a novel method for spectral data acquisition based on optical unmixing, which is discussed in Subsection 7.2.3.

### 7.2.1 Next Steps for the MEMS Levitation Slit

The miniaturization work detailed in Chapter 6 was concluded with the successful demonstration of levitation using the newly developed thin glass chip. Future work would build upon this initial validation with an extensive characterization of the levitation performance under varying input parameters.

The following step involves establishing slit rotation using the electrostatic actuation electrodes. The different versions of slit discs allow for different permissible slit positions. The rotation performance would be characterized in terms of rotation speed, latency, and stability under different sets of actuation voltages. This characterization should also assess the impact of the applied electrostatic force on levitation.

After comprehensive experimental work to map out levitation and rotation performance, the focus would shift to optical experiments. The miniaturized slit device is integrated into the optical setup, shown in Figure 6.25, and carefully positioned at the plane of the intermediate image formed by the front optics. First the rotating slit is tested in the spatial mode to demonstrate the scanning of a field of view and the reconstruction of the spatial image, as demonstrated in Chapter 5. Subsequently, the system is switched to the spectral mode and the miniaturized rotating slit is then tested in the spectral mode to demonstrate the acquisition of the hyperspectral data cube.

After validating the optical performance of the miniaturized rotating slit, the research focus would then be directed to the miniaturization of other key components in the system, specifically the rotating Dove prism, with the aim of achieving a mobile and affordable system.

### 7.2.2 Levitation PSi Filter Wheel for Spectral Imaging

Another project was initiated, within the course of this thesis, with the aim of developing miniaturized spectral imaging systems to benefit public health applications. This project proposes a levitating and rotating miniaturized filter wheel based on porous silicon (PSi) rugate filters to enable a portable wavelength-scanning multispectral imaging system. Figure 7.1 provides a schematic representation of this concept. The light from the target is focused on a filter segment of the wheel, with a specific wavelength, and then reflected into the imaging sensor to be recorded as one plane in the data cube. Rotating the filter wheel allows imaging and recording the target at each wavelength and stacking these 2D images to construct the rest of the data cube. This collaboration project brings contributions in the area of micro-levitation, similar to that presented in Chapter 6, from our institute (IMT), and in the area of porous silicon optical filters from the Institute for Microsystems Technology (IMST) at Furtwangen University. The proposed concept was published by the two groups in [MA3, MA5].

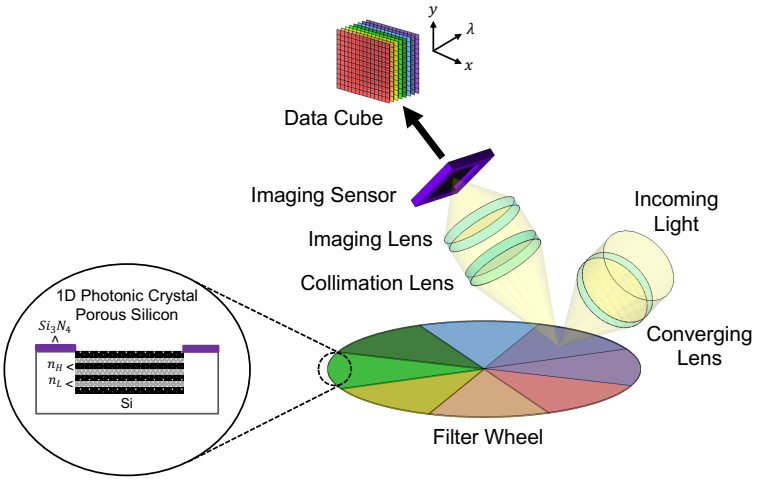


**Figure 7.1:** Illustration of the wavelength-scanning approach based on a rotating porous silicon rugate filter wheel. Reproduced from [MA3], licensed under CC BY 4.0.

Porous silicon is formed through the electrochemical etching (anodization) of crystalline silicon. This is done in an electrolyte based on hydrofluoric acid (HF). The resulting porosity and pore sizes are determined by the applied current density, HF concentration, and the doping level of silicon. Porous silicon can be used to produce rugate optical filters, also referred to as gradient-index filters. This is a type of optical filters characterized by periodic continuous variation of the refractive index along the direction normal to the filter's plane. This variation leads to selective high reflectivity around specific wavelengths of light and very low reflectivity elsewhere. This is similar to a Distributed Bragg Reflector (DBR) with the difference that the profile of refractive index variation in rugate filters resembles a continuous sinusoidal pattern rather than a stepwise variation. Fabricating PSi rugate filters can be achieved by applying a varying current density with a sinusoidal profile during the anodization process. This profile will be reflected in the porosity distribution in the formed porous silicon and consequently in the resulting refractive index profile, where higher porosity corresponds to lower PSi refractive index [MA3, MA5].

In this project, a novel approach is proposed to simultaneously fabricate PSi rugate filter segments, with varying resonance peak wavelengths, on a miniaturized filter wheel [MA3, MA5]. This approach is based on the "current squeezing effect" during the anodization process. This is achieved by varying the geometrical sizes of the filter segments of the wheel which leads to local current redistributions in the filter segments and consequently to a different PSi formation rate and different porosity in each segment. This results in a different reflecting resonance peak wavelength for each filter segment. This approach allows the fabrication of low-cost filter wheels suited for portable multispectral imaging systems. By patterning the segments of the filter wheel and fabricating them on top of an aluminum film, the wheel can be levitated and rotated, following the methods described in Chapters 3 and 6, to enable the wavelength scanning.

Initial samples were fabricated to test the levitation. One of the samples is shown in Figure 7.2 which has a diameter of 3.2 mm and consists of a thinned silicon layer on one side and a deposited aluminum layer on the other side. This sample

did not have structured PSi filters and it was intended as a first step to assess the feasibility of levitating the proposed filter wheel. However levitation could not be achieved with the initial samples. Possible reasons for this include the significantly higher thickness of the samples. The sample in Figure 7.2(b) has a thickness over 87 µm which is much higher compared to the aluminum discs levitated in Chapter 6 which had a thickness of only 10 µm. Another possibility could be the poor quality of the produced samples, which included cracks on the edges of the sample, as shown in Figure 7.2(c), and the poor quality of the deposited aluminum layer which can affect its conductivity, compared to the aluminum sheets used earlier for the slit discs. This can affect the induction of eddy currents in the samples and consequently the feasibility of levitation. A closer look at the sample in Figure 7.2 while trying to levitate it showed slight bending of the sample when the levitation signal was activated. This can be attributed to the two-layer structure and the mismatch in the thermal expansion between them.

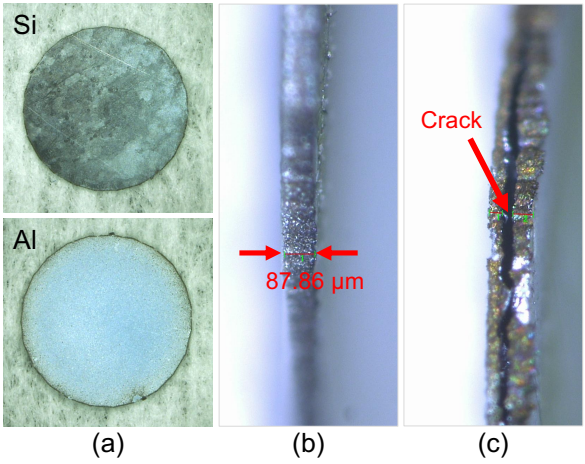


**Figure 7.2:** One of the initial samples used to test the levitation of the proposed filter wheel with 3.2 mm diameter. (a) The sample consists of thinned Si on one side and deposited Al on the other side. (b) The total sample thickness is 87.86 µm. (c) Shows a crack on the edge of the sample.

Future work in this project includes reducing the thickness of the silicon layer to reduce the overall weight of the sample acting against the levitation force. The work also includes improving the quality of the deposited aluminum and evaluating its conductivity compared to the aluminum sheets used for the rotating slit. After establishing levitation, the next step would be testing samples with structured PSi filters and patterned rotation electrodes with the aim of establishing levitation and controlled rotation of the filter wheel. Finally, optical experiments with the rotating filter wheel can be carried out to demonstrate spectral imaging.

### 7.2.3 Portable Hyperspectral Analysis by Real-Time Optical Unmixing – PHARAO

PHARAO is another endeavor initiated within the course of this thesis in alignment with the motivation of developing miniaturized, portable, and real-time hyperspectral imaging systems to benefit public health applications. PHARAO was conceived as a proposal for a joint research project in collaboration with the Institute of Industrial Information Technology (IIIT) and the Institute for Anthropomatics and Robotics (IAR) at KIT. The aim is for the three participating groups to deliver scientific contributions in the areas of microfabrication and signal processing that will open the door for ubiquitous hyperspectral imaging. These contributions include enabling hyperspectral imaging by means of "*Optical Unmixing*" and enabling the 3D nanoprinting of active opto-electro-mechanical systems to fabricate a "*Programmable Optical Filter Array (POFA)*".

The optical unmixing is proposed in PHARAO as a novel hyperspectral analysis modality that simplifies signal processing by shifting part of the computational load to the optical side. This has the advantage of avoiding the time-consuming process of acquiring the entire 3D hyperspectral data cube and alleviating the high computational and memory demands of existing systems. The optical unmixing can be achieved by applying specifically designed and reprogrammable spectral filter functions, which can be implemented through the proposed POFA, to the

incoming light to only acquire the relevant data. This allows the direct recording of endmember abundances from the measured data.

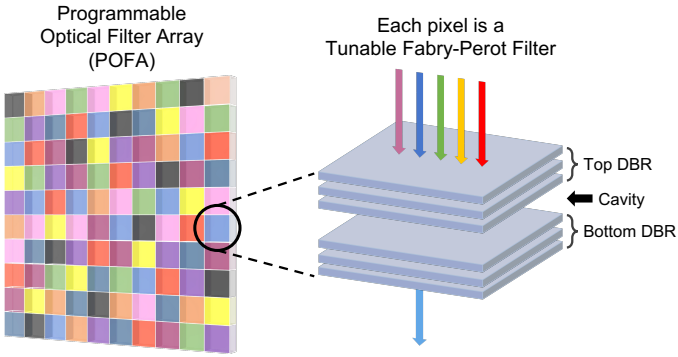


**Figure 7.3:** Schematic representation of the Programmable Optical Filter Array (POFA) where each pixel is a Fabry-Pérot tunable filter controlled separately.

The programmable optical filter array (POFA) is key to the proposed optical unmixing approach. POFA enables the design and reconfiguration of the spectral filter functions of the system which makes it possible to adapt to different applications. Figure 7.3 illustrates the concept of POFA where each element in the array is a Fabry-Pérot tunable optical filter that can be actuated and tuned individually to allow the separate control of the wavelength transmitted through each pixel of the array. Each element consists of two distributed Bragg reflectors (DBR) forming the parallel reflective surfaces of the Fabry-Pérot interferometer, and defining the interference cavity in between. Tuning the cavity size controls the transmitted wavelength. This tuning is proposed through electrostatic actuation and tuning each pixel separately requires each element to be addressed individually to apply the actuation voltage corresponding to the desired wavelength. Achieving this in an efficient way requires a complex 3D wiring network to provide a separate connection for each pixel. The realization of POFA with the individual active elements and the wiring network using existing microfabrication techniques is complex and time-consuming. That is why PHARAO aims to push the limits of 3D

nanoprinting, also known as direct laser writing (DLW), and to investigate novel transparent and electrically conductive photoresists to enable the direct fabrication of miniaturized 3D active opto-electro-mechanical systems such as POFA.

The project proposal was submitted in a research grant application to the DFG[1], first in August 2016, and then a revised version in June 2018, and the concept was published in [MA6]. While the grant application received positive feedback for originality, impact in the society, and potential commercial opportunities, the funding was not granted on the basis of the project being more industry-oriented rather than pursuing fundamentally new scientific approaches. Therefore, in the future, other funding programs that are more suited to the project objectives are to be considered to bring the proposed contributions to execution and further advance the hyperspectral imaging technology for the benefit of public health.

[1] Deutsche Forschungsgemeinschaft—German Research Foundation

# A Microfabrication Parameters

In this appendix, the process parameters applied in different microfabrication steps of the micro-levitation chip in Chapter 6 are summarized.

## A.1 $O_2$ Plasma Cleaning

The $O_2$ plasma is used to clean wafer surfaces prior to further processing to remove any contaminants and to improve surface adhesion. For this purpose, the 4TEC plasma machine is used with the parameters in Table A.1

**Table A.1:** $O_2$ plasma cleaning parameters

| Parameter | Value |
|---|---|
| $O_2$ gas flow | 0.6 SLM |
| Chamber pressure | 0.2 bar |
| RF power | 100 W |

## A.2 SU-8 3025 Spin Coating

The photoresist SU-8 3025 (from Kayaku Advanced Materials Inc.–formally MicroChem Corp.) is used to form the mold for electroplating. The photoresist is applied to the wafer using the spin coating parameters in Table A.2.

## A.3 Au Electroplating

The gold electroplating process is used to increase the thickness of a thin seed layer to a desired thickness. The parameters summarized in Table A.3 are used to

**Table A.2:** SU-8 3025 spin coating parameters

| Parameter | Value |
|---|---|
| Initial speed | 0 rpm |
| Speed ramp | 100 rpm $s^{-1}$ |
| Intermediate speed | 500 rpm |
| Stall time | 10 s |
| Speed ramp | 300 rpm $s^{-1}$ |
| Final speed | 5000 rpm |
| Stall time | 30 s |

increase the thickness of the seed layer from 100 nm to 10 µm to form the pads and connectors of the microcoils. The wafer is kept in the electroplating solution for 15 minutes before starting the process.

**Table A.3:** Au electroplating parameters

| Parameter | Value |
|---|---|
| Solution temperature | 55 °C |
| Current density | 0.2 A/$dm^2$ |
| Electric current | 12 mA |

## A.4 SU-8 2150 Post-Exposure Bake

The photoresist SU-8 2150 (from Kayaku Advanced Materials Inc.–formally MicroChem Corp.) is used to fabricate the coil posts. Due to the high thickness of the deposited layer, a long cycle of post-exposure bake is required to harden the exposed resist before development and coil winding. Figure A.1 shows the temperature curve used for this process.

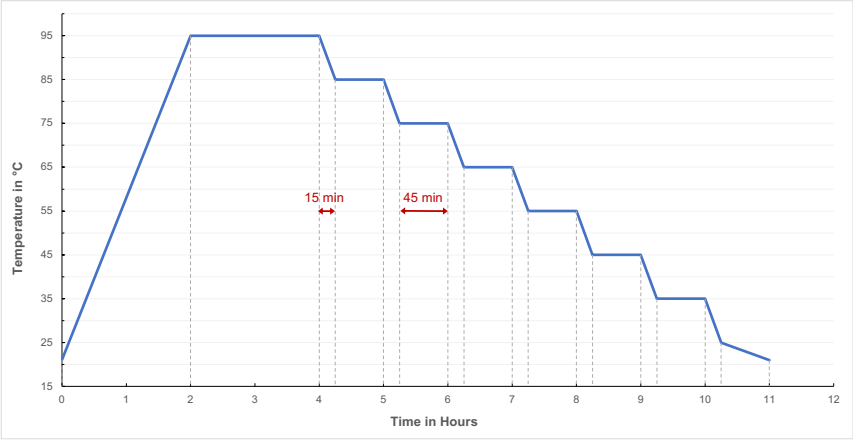


**Figure A.1:** Temperature curve for the post-exposure bake of the thick SU-8 2150 photoresist in the fabrication of the coil posts.

## A.5 AZ 1505 Spin Coating

The photoresist AZ 1505 (from MicroChemicals GmbH) is used as a mask during the etching of thin metal layers, such as the evaporated Cr/Au seed layer. The photoresist is applied to the wafer using the spin coating parameters in Table A.4.

**Table A.4:** AZ 1505 spin coating parameters

| Parameter | Value |
|---|---|
| Initial speed | 0 rpm |
| Speed ramp | 500 rpm $s^{-1}$ |
| Final speed | 1500 rpm |
| Stall time | 60 s |

## A.6 Cryogenic Deep Reactive Ion Etching (DRIE)

The cryogenic deep reactive ion etching (DRIE) is used for deep anisotropic etching. The parameters in Table A.5 are used for etching the $SiO_2$ layer on top of the bulk Si wafer, to open the center hole.

**Table A.5:** Cryogenic DRIE process parameters

| Parameter | Value |
|---|---|
| Etchant gas | $CHF_3$ |
| Flow rate | $455\,cm^3\,min^{-1}$ |
| RF power | 50 W |
| ICP power | 2500 W |

# B Wire Bonding Parameters

This appendix summarizes the wire bonding parameters used for winding the levitation coils (Cu ball-wedge bond) and for connecting the coil pads to the PCB pads (Al wedge-wedge bond) to supply the AC signal to the coils.

## B.1 Cu Ball-Wedge Bond

The winding of the levitation coils is made with a Cu wire with 25 µm diameter, using the wire bonder (ESEC 3100 Plus). The parameters listed below are provided by Dr. Hossein Davoodi, who was responsible for the wire bonder at the institute, for the Cu ball-wedge bonds on the Au coil pads. The parameters for the formation of the "Free Air Ball (FAB)", which is the initial spherical ball formed at the tip of the bonding wire by a high-voltage spark, are given in Table B.1. Then the parameters for creating the ball bond and the wedge bond are given in Table B.2.

**Table B.1:** Free Air Ball (FAB) parameters

| Parameter | Value |
|---|---|
| Pre spark voltage | 4500 V |
| Current | 100 mA |
| Time | 0.50 ms |
| Tail length | 500 µm |
| Electrode-to-wire distance | 1000 µm |

**Table B.2:** Bond parameters for Cu ball bond and Cu wedge bond

| Parameter | Value | |
|---|---|---|
| | Cu ball bond | Cu wedge bond |
| Bond mode | Standard | Standard |
| Impact force | 200 mN | 350 mN |
| Bond force | 350 mN | 700 mN |
| Ultrasonic power | 78 % | 38 % |
| Bond time | 40 ms | 40 ms |
| Ultrasonic rise time | 1 ms | 1 ms |
| Search height | 150 µm | 150 µm |
| Pre Ultrasonic power | 45 % | 10 % |

## B.2 Al Wedge-Wedge Bond

The wire bonding of the levitation coil pads to the PCB is made with a 50 µm Al wire using the wire bonder HB05 (from TPT Wirebonder GmbH & Co. KG) following the parameters listed in Table B.3. The first bond is on the Au pad of the coil and the second bond is on the Cu pad of the PCB.

**Table B.3:** Al wedge-wedge bond parameters

| Parameter | Bond 1 (Au) | Bond 2 (Cu) |
|---|---|---|
| Ultrasonic | 230 | 350 |
| Time | 120 | 200 |
| Force | 70 | 70 |

# C Laser Machining Parameters

This appendix provides a summary of the laser machining parameters of the Tangerine system (from Amplitude Laser) used to etch and cut glass wafers in the fabrication of the levitation chip, as well as to cut aluminum foil for producing the slit discs. The fixed parameters of the Tangerine system are listed in Table C.1.

**Table C.1:** Fixed parameters of the Tangerine laser system

| Parameter | Value |
|---|---|
| Wavelength | 1030 nm |
| Frequency | 200 kHz |
| Pulse width | 400 fs |
| Total power | 29 W |
| Beam diameter at the sample | 30 µm |

## C.1 Laser Etching in Glass

The laser etching in glass is achieved through the sequential removal of glass particles by moving the laser over a predefined path. The Tangerine system is used and the machining parameters are varied to achieve the desired depth and quality. The power is controlled as a percentage of the system total power, while the cutting speed and number of repetitions are used as two more variable parameters to control the outcome of the laser machining process. Figure C.1 shows the effect of the laser power and the number of repetitions on the etching depth in glass. The parameters are optimized experimentally to produce the required quality and avoid defects such as that shown in Figure C.2.

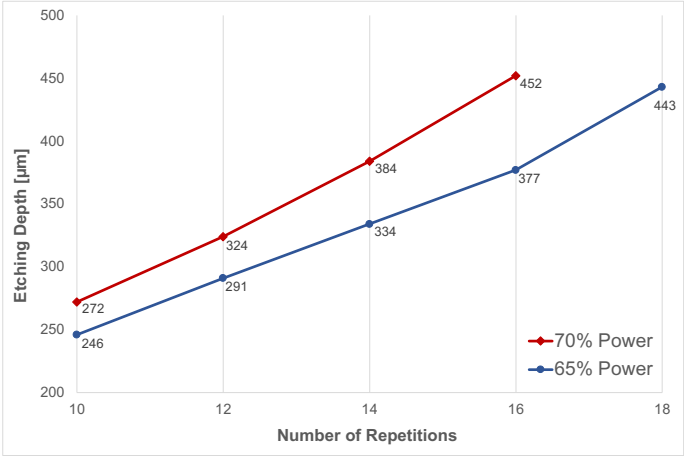


**Figure C.1:** The effect of laser power and number of repetitions on the achieved etching depth in glass laser etching. The cutting speed is fixed at 1000 mm/s.

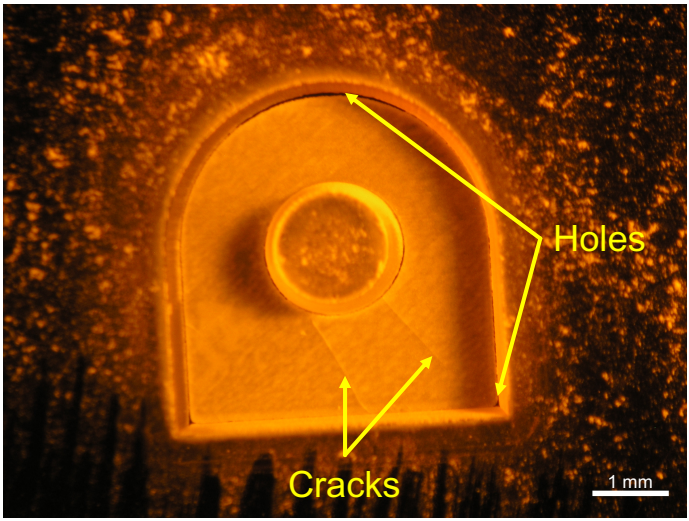


**Figure C.2:** High laser power and high number of repetitions can cause cracks and holes in the glass substrate during laser etching.

## C.2 Laser Cutting of Glass

The cutting of glass wafers with different thicknesses in the fabrication of the levitation chip is carried out using the parameters in Table C.2.

**Table C.2:** Laser cutting parameters of glass

| Parameter | Value (based on wafer thickness) | | |
|---|---|---|---|
| | 50 µm | 100 µm | 500 µm |
| % of Total power | 50% | 60% | 70% |
| Cutting speed | 1000 mm/s | 1000 mm/s | 1000 mm/s |
| No. of repetitions | 2 | 4 | 18 |

## C.3 Laser Cutting of Aluminum

The proof masses and slit discs are fabricated from an aluminum foil with 10 µm thickness (from Advent Research Materials Ltd) using the parameters in Table C.3.

**Table C.3:** Laser cutting parameters of Aluminum

| Parameter | Value |
|---|---|
| Wavelength | 343 nm |
| Frequency | 200 kHz |
| Pulse width | 400 fs |
| Total power | 6 W |
| % of Total power | 70 % |
| Beam diameter at the sample | 20 µm |
| Cutting speed | 1000 mm |
| No. of repetitions | 9 |

# List of Figures

# List of Tables

# Bibliography


[1] José M Bioucas-Dias, Antonio Plaza, Nicolas Dobigeon, Mario Parente, Qian Du, Paul Gader, and Jocelyn Chanussot. "Hyperspectral unmixing overview: Geometrical, statistical, and sparse regression-based approaches". In: *IEEE Journal of Selected Topics in Applied Earth Observations and Remote Sensing* 5.2 (2012), pp. 354–379.

[2] Aziz ul Rehman and Shahzad Ahmad Qureshi. "A review of the medical hyperspectral imaging systems and unmixing algorithms' in biological tissues". In: *Photodiagnosis and Photodynamic Therapy* 33 (2021), p. 102165.

[3] Ali Nahidi, William E Roper, and Richard B Gomez. "Hyperspectral systems' role in understanding the composition of atmospheric air pollution". In: *Geo-Spatial and Temporal Image and Data Exploitation III*. Vol. 5097. SPIE. 2003, pp. 167–177.

[4] Alexander FH Goetz, Gregg Vane, Jerry E Solomon, and Barrett N Rock. "Imaging spectrometry for earth remote sensing". In: *science* 228.4704 (1985), pp. 1147–1153.

[5] Hiroshi Okamoto, Tetsuro Murata, Takashi Kataoka, and SHUN-ICHI HATA. "Plant classification for weed detection using hyperspectral imaging with wavelet analysis". In: *Weed biology and Management* 7.1 (2007), pp. 31–37.

[6] Elke Bauriegel and Werner B Herppich. "Hyperspectral and chlorophyll fluorescence imaging for early detection of plant diseases, with special reference to Fusarium spec. infections on wheat". In: *Agriculture* 4.1 (2014). Licensed under CC BY 3.0: https://creativecommons.org/licenses/by/3.0/, pp. 32–57. URL: `https://doi.org/10.3390/agriculture4010032`.

[7] Pilar Beatriz García Allende, Olga María Conde Portilla, José Miguel López Higuera, et al. *Hyperspectral imaging for raw material sorting and processed product quality control*. Intech, 2011.

[8] Petra Tatzer, Thomas Panner, Markus Wolf, and Gerhard Traxler. “Inline sorting with hyperspectral imaging in an industrial environment”. In: *Real-Time Imaging IX*. Vol. 5671. SPIE. 2005, pp. 162–173.

[9] Thomas Arnold, Martin De Biasio, Raghavendra Kammari, and Krithika Sayar-Chand. “Development of VIS/NIR hyperspectral imaging system for industrial sorting applications”. In: *Algorithms, Technologies, and Applications for Multispectral and Hyperspectral Imaging XXVII*. Vol. 11727. SPIE. 2021, pp. 298–304.

[10] Javier Rivera, Fernando Valverde, Manuel Saldaña, and Vidya Manian. “Security inspection in ports by anomaly detection using hyperspectral imaging technology”. In: *Algorithms and Technologies for Multispectral, Hyperspectral, and Ultraspectral Imagery XIX*. Vol. 8743. SPIE. 2013, pp. 65–75.

[11] Matthew P Nelson, Andrew Basta, Raju Patil, Oksana Klueva, and Patrick J Treado. “Development of a handheld widefield hyperspectral imaging (HSI) sensor for standoff detection of explosive, chemical, and narcotic residues”. In: *Next-Generation Spectroscopic Technologies VI*. Vol. 8726. SPIE. 2013, pp. 12–20.

[12] Gerda J Edelman, Edurne Gaston, Ton G Van Leeuwen, PJ Cullen, and Maurice CG Aalders. “Hyperspectral imaging for non-contact analysis of forensic traces”. In: *Forensic science international* 223.1-3 (2012), pp. 28–39.

[13] Michele Hinnrichs and Bob Piatek. “Hand-held hyperspectral imager for chemical/biological and environmental applications”. In: *Environmental Monitoring and Remediation III*. Vol. 5270. SPIE. 2004, pp. 10–18.

[14] Hermann Kaufmann, Karl Segl, Sabine Chabrillat, Stefan Hofer, Timo Stuffler, Andreas Mueller, Rudolf Richter, Gunter Schreier, Rupert Haydn, and Heike Bach. “EnMAP a hyperspectral sensor for environmental mapping and analysis”. In: *2006 IEEE International Symposium on Geoscience and Remote Sensing*. IEEE. 2006, pp. 1617–1619.

[15] TVV King, RF Kokaly, TM Hoefen, KB Dudek, and KE Livo. *Surface materials map of Afghanistan: iron-bearing minerals and other materials*. Public domain. 2011. URL: `https://www.usgs.gov/media/images/surface-materials-map-afghanistan-`

iron - bearing - minerals - and - other - materials (visited on 02/07/2022).

[16] Lou Gevaux, Jordan Gierschendorf, Juliette Rengot, Marie Cherel, Pierre Séroul, Alex Nkengne, Julie Robic, Alain Trémeau, and Mathieu Hébert. "Real-time skin chromophore estimation from hyperspectral images using a neural network". In: *Skin Research and Technology* 27.2 (2021), pp. 163–177.

[17] Svetlana V Panasyuk, Shi Yang, Douglas V Faller, Duyen Ngo, Robert A Lew, Jenny E Freeman, and Adrianne E Rogers. "Medical hyperspectral imaging to facilitate residual tumor identification during surgery". In: *Cancer biology & therapy* 6.3 (2007). ©copyright 2007, reprinted by permission of Informa UK Limited, trading as Taylor & Taylor & Francis Group, http://www.tandfonline.com, pp. 439–446.

[18] Quoc Thien Pham and Nai-Shang Liou. "Hyperspectral imaging system with rotation platform for investigation of jujube skin defects". In: *Applied Sciences* 10.8 (2020). Licensed under CC BY 4.0: https://creativecommons.org/licenses/by/4.0/, p. 2851. URL: https://doi.org/10.3390/app10082851.

[19] Hongzhe Jiang, Wei Wang, Hong Zhuang, Seung-Chul Yoon, Yi Yang, and Xin Zhao. "Hyperspectral imaging for a rapid detection and visualization of duck meat adulteration in beef". In: *Food Analytical Methods* 12 (2019), pp. 2205–2215.

[20] Hui Huang, Li Liu, and Michael O Ngadi. "Recent developments in hyperspectral imaging for assessment of food quality and safety". In: *Sensors* 14.4 (2014), pp. 7248–7276.

[21] Yankun Peng and Wei Wang. "Prediction of pork meat total viable bacteria count using hyperspectral imaging system and support vector machines". In: *Food Processing Automation Conference Proceedings, 28-29 June 2008, Providence, Rhode Island*. American Society of Agricultural and Biological Engineers. 2008, p. 35.

[22] Yankun Peng, Jing Zhang, Wei Wang, Yongyu Li, Jianhu Wu, Hui Huang, Xiaodong Gao, and Weikang Jiang. "Potential prediction of the microbial spoilage of beef using spatially resolved hyperspectral scattering profiles". In: *Journal of Food Engineering* 102.2 (2011), pp. 163–169.

[23] Diwan P Ariana and Renfu Lu. “Evaluation of internal defect and surface color of whole pickles using hyperspectral imaging”. In: *Journal of Food Engineering* 96.4 (2010), pp. 583–590.

[24] Juan Xing, Wouter Saeys, and Josse De Baerdemaeker. “Combination of chemometric tools and image processing for bruise detection on apples”. In: *Computers and electronics in agriculture* 56.1 (2007), pp. 1–13.

[25] Eugenio Ivorra, Joel Girón, Antonio J Sánchez, Samuel Verdú, Jose M Barat, and Raúl Grau. “Detection of expired vacuum-packed smoked salmon based on PLS-DA method using hyperspectral images”. In: *Journal of food engineering* 117.3 (2013), pp. 342–349.

[26] Won Jun, Moon S Kim, Byoung-Kwan Cho, Patricia D Millner, Kuanglin Chao, and Diane E Chan. “Microbial biofilm detection on food contact surfaces by macro-scale fluorescence imaging”. In: *Journal of food engineering* 99.3 (2010), pp. 314–322.

[27] Guolan Lu and Baowei Fei. “Medical hyperspectral imaging: a review”. In: *Journal of biomedical optics* 19.1 (2014), pp. 010901–010901.

[28] David T Dicker, Jeremy Lerner, Pat Van Belle, DuPont Guerry 4th, Meenhard Herlyn, David E Elder, and Wafik S El-Deiry. “Differentiation of normal skin and melanoma using high resolution hyperspectral imaging”. In: *Cancer biology & therapy* 5.8 (2006), pp. 1033–1038.

[29] Zhi Liu, Hongjun Wang, and Qingli Li. “Tongue tumor detection in medical hyperspectral images”. In: *Sensors* 12.1 (2011), pp. 162–174.

[30] Dmitry Yudovsky, Aksone Nouvong, and Laurent Pilon. “Hyperspectral imaging in diabetic foot wound care”. In: *Journal of diabetes science and technology* 4.5 (2010), pp. 1099–1113.

[31] William R Johnson, Daniel W Wilson, Wolfgang Fink, Mark Humayun, and Greg Bearman. “Snapshot hyperspectral imaging in ophthalmology”. In: *Journal of biomedical optics* 12.1 (2007), pp. 014036–014036.

[32] Peter Usenik, Miran Bürmen, Aleš Fidler, Franjo Pernuš, and Boštjan Likar. “Evaluation of cross-polarized near infrared hyperspectral imaging for early detection of dental caries”. In: *Lasers in Dentistry XVIII*. Vol. 8208. SPIE. 2012, pp. 85–91.

[33] Yuval Garini, Ian T Young, and George McNamara. “Spectral imaging: principles and applications”. In: *Cytometry part a: the journal of the international society for analytical cytology* 69.8 (2006), pp. 735–747.

[34] IJ Wilson and TD Cocks. “Development of the airborne reflective emissive spectrometer (ARES)-a progress report”. In: *Proc. of 3rd EARSeL Workshop on Imaging Spectroscopy*. Citeseer. 2003, pp. 13–16.

[35] T Weser, F Rottensteiner, J Willneff, and CS Fraser. “An improved pushbroom scanner model for precise georeferencing of ALOS PRISM imagery”. In: *ISPRS Congress*. Vol. 21. 2008, pp. 724–729.

[36] Shen-En Qian. “Hyperspectral satellites, evolution, and development history”. In: *IEEE Journal of Selected Topics in Applied Earth Observations and Remote Sensing* 14 (2021). Licensed under CC BY-NC-ND 4.0: https://creativecommons.org/licenses/by-nc-nd/4.0/, pp. 7032–7056. URL: https://doi.org/10.1109/JSTARS.2021.3090256.

[37] Xiaomei Liu, Ziqi Jiang, Tianci Wang, Fuhong Cai, and Dan Wang. “Fast hyperspectral imager driven by a low-cost and compact galvo-mirror”. In: *Optik* 224 (2020), p. 165716.

[38] Xue Dong, Xingchen Xiao, Yining Pan, Guangyao Wang, and Yiting Yu. “DMD-based hyperspectral imaging system with tunable spatial and spectral resolution”. In: *Optics express* 27.12 (2019), pp. 16995–17006.

[39] Johannes Brauers, Nils Schulte, and Til Aach. “Multispectral filter-wheel cameras: Geometric distortion model and compensation algorithms”. In: *IEEE transactions on image processing* 17.12 (2008), pp. 2368–2380.

[40] Aiwu Zhang, Shaoxing Hu, Xizhen Zhang, Taipei Zhang, Mengnan Li, Haiyu Tao, and Yan Hou. “A handheld grassland vegetation monitoring system based on multispectral imaging”. In: *Agriculture* 11.12 (2021), p. 1262.

[41] Thomas D Rahmlow Jr, William Cote, and Robert Johnson Jr. “Hyperspectral imaging using a Linear Variable Filter (LVF) based ultra-compact camera”. In: *Photonic Instrumentation Engineering VII*. Vol. 11287. SPIE. 2020, pp. 249–260.

[42] Shigeng Song, Des Gibson, Sam Ahmadzadeh, Hin On Chu, Barry Warden, Russell Overend, Fraser Macfarlane, Paul Murray, Stephen Marshall, Matt Aitkenhead, et al. “Low-cost hyper-spectral imaging system using a linear variable bandpass filter for agritech applications”. In: *Applied optics* 59.5 (2020), A167–A175.

[43] Nicolaas Tack, Andy Lambrechts, Philippe Soussan, and Luc Haspeslagh. “A compact, high-speed, and low-cost hyperspectral imager”. In: *Silicon Photonics VII*. Vol. 8266. SPIE. 2012, pp. 126–138.

[44] Nahum Gat. “Imaging spectroscopy using tunable filters: a review”. In: *Wavelet Applications VII*. Vol. 4056. SPIE. 2000, pp. 50–64.

[45] Rami Mannila, Christer Holmlund, Harri J Ojanen, Antti Näsilä, and Heikki Saari. “Short-wave infrared (SWIR) spectral imager based on Fabry-Perot interferometer for remote sensing”. In: *Sensors, Systems, and Next-Generation Satellites XVIII*. Vol. 9241. SPIE. 2014, pp. 426–433.

[46] Antti Näsilä, Roberts Trops, Ingmar Stuns, Tahvo Havia, Heikki Saari, Bin Guo, Harri J Ojanen, Altti Akujärvi, and Anna Rissanen. “Hand-held MEMS hyperspectral imager for VNIR mobile applications”. In: *MOEMS and Miniaturized Systems XVII*. Vol. 10545. SPIE. 2018, pp. 177–185.

[47] Jong-Ha Lee and Chang-Hee Won. “Characterization of lung tissues using liquid-crystal tunable filter and hyperspectral imaging system”. In: *2009 Annual International Conference of the IEEE Engineering in Medicine and Biology Society*. IEEE. 2009, pp. 1416–1419.

[48] J Ward, M Farries, C Pannell, and E Wachman. “An acousto-optic based hyperspectral imaging camera for security and defence applications”. In: *Electro-Optical Remote Sensing, Photonic Technologies, and Applications IV*. Vol. 7835. SPIE. 2010, pp. 285–293.

[49] Myeong-su Ahn, Charles Soon Hong Hwang, Kyung-Won Jang, and Ki-Hun Jeong. “Compact hyperspectral camera using angle-sensitive plasmonic structures”. In: *SPIE Advanced Biophotonics Conference (SPIE ABC 2021)*. Vol. 12159. SPIE. 2022, pp. 22–26.

[50] Cui Ma, Ming Yu, Fokui Chen, and Hui Lin. “An efficient and portable LED multispectral imaging system and its application to human tongue detection”. In: *Applied Sciences* 12.7 (2022), p. 3552.

[51] Annemarie McCarthy, Killian Barton, and Liam Lewis. “Low-cost multispectral imager”. In: *Journal of Chemical Education* 97.10 (2020), pp. 3892–3898.

[52] Anna Rissanen, Bin Guo, Heikki Saari, Antti Näsilä, Rami Mannila, Altti Akujärvi, and Harri Ojanen. "VTT's Fabry-Perot interferometer technologies for hyperspectral imaging and mobile sensing applications". In: *Moems and Miniaturized Systems Xvi*. Vol. 10116. SPIE. 2017, pp. 119–130.

[53] Te-Yu Tseng, Pau-Jen Lai, and Kung-Bin Sung. "High-throughput detection of immobilized plasmonic nanoparticles by a hyperspectral imaging system based on Fourier transform spectrometry". In: *Optics express* 19.2 (2011), pp. 1291–1300.

[54] Andrew Robert Harvey and David William Fletcher-Holmes. "Birefringent Fourier-transform imaging spectrometer". In: *Optics Express* 12.22 (2004), pp. 5368–5374.

[55] Antonio Perri, BE Nogueira De Faria, DC Teles Ferreira, D Comelli, G Valentini, F Preda, D Polli, AM De Paula, G Cerullo, and C Manzoni. "Hyperspectral imaging with a TWINS birefringent interferometer". In: *Optics express* 27.11 (2019), pp. 15956–15967.

[56] Nathan Hagen and Michael W Kudenov. "Review of snapshot spectral imaging technologies". In: *Optical Engineering* 52.9 (2013). Licensed under CC BY 4.0: https://creativecommons.org/licenses/by/4.0/, pp. 090901–090901. URL: https://doi.org/10.1117/1.OE.52.9.090901.

[57] Andy Lambrechts, Pilar Gonzalez, Bert Geelen, Philippe Soussan, Klaas Tack, and Murali Jayapala. "A CMOS-compatible, integrated approach to hyper-and multispectral imaging". In: *2014 IEEE International Electron Devices Meeting*. IEEE. 2014, pp. 10–5.

[58] Bert Geelen, Nicolaas Tack, and Andy Lambrechts. "A compact snapshot multispectral imager with a monolithically integrated per-pixel filter mosaic". In: *Advanced fabrication technologies for micro/nano optics and photonics VII*. Vol. 8974. SPIE. 2014, pp. 80–87.

[59] Jaesoong Lee, Yeonsang Park, Hyochul Kim, Young-Zoon Yoon, Woong Ko, Kideock Bae, Jeong-Yub Lee, Hyuck Choo, and Young-Geun Roh. "Compact meta-spectral image sensor for mobile applications". In: *Nanophotonics* 11.11 (2022). Licensed under CC BY 4.0: https://creativecommons.org/licenses/by/4.0/, pp. 2563–2569. URL: https://doi.org/10.1515/nanoph-2021-0706.

[60] Bert Geelen, Nicolaas Tack, and Andy Lambrechts. “A snapshot multispectral imager with integrated tiled filters and optical duplication”. In: *Advanced Fabrication Technologies for Micro/Nano Optics and Photonics VI*. Vol. 8613. SPIE. 2013, pp. 173–185.

[61] Carolina Blanch-Perez-del-Notario, Siri Luthman, Robin Lefrant, Pilar Gonzalez, and Andy Lambrechts. “Compact high-speed snapshot hyperspectral imager in the SWIR range (1.1-1.65 nm) and its potential in sorting/recycling industry”. In: *Algorithms, Technologies, and Applications for Multispectral and Hyperspectral Imaging XXVIII*. Vol. 12094. SPIE. 2022, pp. 47–55.

[62] Bert Geelen and Klaas Tack. “A new compact snapshot multispectral mosaic imager with an improved deposition process”. In: *Integrated Optics: Devices, Materials, and Technologies XXVI*. Vol. 12004. SPIE. 2022, pp. 180–186.

[63] Andrew McClung, Sarath Samudrala, Mahsa Torfeh, Mahdad Mansouree, and Amir Arbabi. “Snapshot spectral imaging with parallel metasystems”. In: *Science advances* 6.38 (2020), eabc7646.

[64] N Danz, B Höfer, E Förster, T Flügel-Paul, T Harzendorf, P Dannberg, R Leitel, S Kleinle, and R Brunner. “Miniature integrated micro-spectrometer array for snap shot multispectral sensing”. In: *Optics Express* 27.4 (2019), pp. 5719–5728.

[65] M Hubold, R Berlich, R Brüning, and R Brunner. “System calibration and characterization of an ultra-compact multispectral snapshot imaging system”. In: *Photonics and Education in Measurement Science 2019*. Vol. 11144. SPIE. 2019, pp. 213–218.

[66] Sascha Grusche. “Basic slit spectroscope reveals three-dimensional scenes through diagonal slices of hyperspectral cubes”. In: *Applied optics* 53.20 (2014), pp. 4594–4603.

[67] Takayuki Okamoto and Ichirou Yamaguchi. “Simultaneous acquisition of spectral image information”. In: *Optics letters* 16.16 (1991), pp. 1277–1279.

[68] Ralf Habel, Michael Kudenov, and Michael Wimmer. “Practical spectral photography”. In: *Computer graphics forum*. Vol. 31. 2pt2. Wiley Online Library. 2012, pp. 449–458.

[69] Michael E Gehm, Renu John, David J Brady, Rebecca M Willett, and Timothy J Schulz. “Single-shot compressive spectral imaging with a dual-disperser architecture”. In: *Optics express* 15.21 (2007), pp. 14013–14027.

[70] Ashwin Wagadarikar, Renu John, Rebecca Willett, and David Brady. “Single disperser design for coded aperture snapshot spectral imaging”. In: *Applied optics* 47.10 (2008), B44–B51.

[71] Ashwin A Wagadarikar, Nikos P Pitsianis, Xiaobai Sun, and David J Brady. “Video rate spectral imaging using a coded aperture snapshot spectral imager”. In: *Optics express* 17.8 (2009), pp. 6368–6388.

[72] Spectral Imaging Ltd Specim. *Specim FX10*. URL: `https://www.specim.com/products/specim-fx10/` (visited on 07/12/2022).

[73] Hyung-Kew Lee, Kyu-Sang Kim, Il-Joo Cho, and Euisik Yoon. “A wide range linearly-tunable optical filter using magnetic actuation”. In: *17th IEEE International Conference on Micro Electro Mechanical Systems. Maastricht MEMS 2004 Technical Digest*. IEEE. 2004, pp. 93–96.

[74] Chang-Kyu Kim, Myung-Lae Lee, and Chi-Hoon Jun. “Electrothermally actuated Fabry-Perot tunable filter with a high tuning efficiency”. In: *IEEE Photonics Technology Letters* 16.8 (2004), pp. 1894–1896.

[75] Jarkko Antila, Akseli Miranto, Jussi Mäkynen, Mari Laamanen, Anna Rissanen, Martti Blomberg, Heikki Saari, and Jouko Malinen. “MEMS and piezo actuator-based Fabry-Perot interferometer technologies and applications at VTT”. In: *Next-Generation Spectroscopic Technologies III*. Vol. 7680. SPIE. 2010, pp. 192–203.

[76] NF Raley, DR Ciarlo, JC Koo, B Beiriger, J Trujillo, C Yu, G Loomis, and R Chow. “A Fabry-Perot microinterferometer for visible wavelengths”. In: *Technical Digest IEEE Solid-State Sensor and Actuator Workshop*. IEEE. 1992, pp. 170–173.

[77] Martti Blomberg, Hannu Kattelus, and Akseli Miranto. “Electrically tunable surface micromachined Fabry–Perot interferometer for visible light”. In: *Sensors and Actuators A: Physical* 162.2 (2010), pp. 184–188.

[78] Neelam Gupta, Songsheng Tan, and Dennis R Zander. “MEMS-based tunable Fabry-Perot filters”. In: *Next-Generation Spectroscopic Technologies IV*. Vol. 8032. SPIE. 2011, pp. 19–28.

[79] Nozomu Hirokubo, Hiroshi Komatsu, Nobuaki Hashimoto, Makoto Sonehara, and Toshiro Sato. “Wideband visible wavelength range MEMS Fabry-Perot Tunable Filter with Ag alloy mirror”. In: *Electronics and Communications in Japan* 96.3 (2013), pp. 17–23.

[80] Anna-Maria Raita-Hakola, Leevi Annala, Vivian Lindholm, Roberts Trops, Antti Näsilä, Heikki Saari, Annamari Ranki, and Ilkka Pölönen. “FPI Based Hyperspectral Imager for the Complex Surfaces-Calibration, Illumination and Applications”. In: *Sensors* 22.9 (2022). Licensed under CC BY 4.0: https://creativecommons.org/licenses/by/4.0/, p. 3420. URL: https://doi.org/10.3390/s22093420.

[81] Jarkko Antila, Rami Mannila, Uula Kantojärvi, Christer Holmlund, Anna Rissanen, Ismo Näkki, Jyrki Ollila, and Heikki Saari. “Spectral imaging device based on a tuneable MEMS Fabry-Perot interferometer”. In: *Next-Generation Spectroscopic Technologies V*. Vol. 8374. SPIE. 2012, pp. 123–132.

[82] Valery Zheludev, Ilkka Pölönen, Noora Neittaanmäki-Perttu, Amir Averbuch, Pekka Neittaanmäki, Mari Grönroos, and Heikki Saari. “Delineation of malignant skin tumors by hyperspectral imaging using diffusion maps dimensionality reduction”. In: *Biomedical Signal Processing and Control* 16 (2015), pp. 48–60.

[83] Anna Rissanen, Heikki Saari, Kari Rainio, Ingmar Stuns, Kai Viherkanto, Christer Holmlund, Ismo Näkki, and Harri Ojanen. “MEMS FPI-based smartphone hyperspectral imager”. In: *Next-Generation Spectroscopic Technologies IX*. Vol. 9855. SPIE. 2016, pp. 42–57.

[84] Bert Geelen, Carolina Blanch, Pilar Gonzalez, Nicolaas Tack, and Andy Lambrechts. “A tiny VIS-NIR snapshot multispectral camera”. In: *Advanced Fabrication Technologies for Micro/Nano Optics and Photonics VIII*. Vol. 9374. SPIE. 2015, pp. 194–201.

[85] Mary B Stuart, Andrew JS McGonigle, Matthew Davies, Matthew J Hobbs, Nicholas A Boone, Leigh R Stanger, Chengxi Zhu, Tom D Pering, and Jon R Willmott. “Low-cost hyperspectral imaging with a smartphone”. In: *Journal of Imaging* 7.8 (2021). Licensed under CC BY 4.0: https://creativecommons.org/licenses/by/4.0/, p. 136. URL: https://doi.org/10.3390/jimaging7080136.

[86] MohammadSadegh Faraji-Dana, Ehsan Arbabi, Hyounghan Kwon, Seyedeh Mahsa Kamali, Amir Arbabi, John G Bartholomew, and Andrei Faraon. “Hyperspectral imager with folded metasurface optics”. In: *ACS Photonics* 6.8 (2019), pp. 2161–2167.

[87] Jiadong Zhao, Weijie Kong, Changtao Wang, Mingbo Pu, Jinjin Jin, Xiaoliang Ma, Xiong Li, and Xiangang Luo. “Planar hyperspectral imager with small smile and keystone based on two metasurfaces”. In: *IEEE Photonics Journal* 14.1 (2021), pp. 1–8.

[88] João Paulo Carmo, Rui Pedro Rocha, Marian Bartek, Ger de Graaf, Reinoud F Wolffenbuttel, and Jose Higino Correia. “A review of visible-range Fabry–Perot microspectrometers in silicon for the industry”. In: *Optics & Laser Technology* 44.7 (2012), pp. 2312–2320.

[89] Nozomu Hirokubo, Hiroshi Komatsu, Nobuaki Hashimoto, Makoto Sonehara, and Toshiro Sato. “Wideband visible wavelength range MEMS Fabry–Perot tunable filter with highly accurate calibration system”. In: *IEEE Sensors Journal* 13.8 (2013), pp. 2930–2936.

[90] Aoife A Gowen, Colm P O’Donnell, Patrick J Cullen, Gérard Downey, and Jesus M Frias. “Hyperspectral imaging–an emerging process analytical tool for food quality and safety control”. In: *Trends in food science & technology* 18.12 (2007), pp. 590–598.

[91] Jonghee Yoon, James Joseph, Dale J Waterhouse, A Siri Luthman, George SD Gordon, Massimiliano Di Pietro, Wladyslaw Januszewicz, Rebecca C Fitzgerald, and Sarah E Bohndiek. “A clinically translatable hyperspectral endoscopy (HySE) system for imaging the gastrointestinal tract”. In: *Nature communications* 10.1 (2019), p. 1902.

[92] Fred Sigernes, Dag Arne Lorentzen, Karsten Heia, and Trond Svenøe. “Multipurpose spectral imager”. In: *Applied optics* 39.18 (2000), pp. 3143–3153.

[93] José A Gutiérrez-Gutiérrez, Arturo Pardo, Eusebio Real, José M López-Higuera, and Olga M Conde. “Custom scanning hyperspectral imaging system for biomedical applications: modeling, benchmarking, and specifications”. In: *Sensors* 19.7 (2019), p. 1692.

[94] Chenghai Yang, James H Everitt, Michael R Davis, and Chengye Mao. “A CCD camera-based hyperspectral imaging system for stationary and airborne applications”. In: *Geocarto International* 18.2 (2003), pp. 71–80.

[95] Mark Allen Lanoue. “Hyperspectral/multispectral dispersive system with scanning entry slit moving across lens focus plane”. US20080285027A1. US Patent App. 12/104,631. Nov. 2008.

[96] Reza Arablouei, Ethan Goan, Stephen Gensemer, and Branislav Kusy. “Fast and robust pushbroom hyperspectral imaging via DMD-based scanning”. In: *Novel Optical Systems Design and Optimization XIX*. Vol. 9948. SPIE. 2016, pp. 7–17.

[97] *DLP6500 0.65 1080p MVSP S600 DMD datasheet (Rev. B)*. URL: https://www.ti.com/lit/ds/symlink/dlp6500fye.pdf?ts=1657638113769%5C&ref%5C_url=https%3A%2F%2Fwww.ti.com%2Fproduct%2FDLP6500FYE (visited on 07/12/2022).

[98] *DLP7000 DLP 0.7 XGA 2x LVDS Type A DMD datasheet (Rev. F)*. URL: https://www.ti.com/lit/ds/symlink/dlp7000.pdf?ts=1657621810095%5C&ref%5C_url=https%3A%2F%2Fwww.ti.com%2Fproduct%2FDLP7000 (visited on 07/12/2022).

[99] Xingchen Xiao, Xue Dong, and Yiting Yu. “MEMS-based linear micromirror array with a high filling factor for spatial light modulation”. In: *Optics Express* 29.21 (2021), pp. 33785–33794.

[100] Werner Schmidt. *Optical Spectroscopy in Chemistry and Life Sciences. An Introduction*. Wiley Online Library, 2005. ISBN: 3527299114.

[101] Hans Zappe. *Fundamentals of Micro-optics*. Cambridge University Press, 2010. ISBN: 9780521895422.

[102] Spigget. *Dispersive Prism Illustration*. Wikimedia Commons. Licensed under CC BY-SA 3.0: https://creativecommons.org/licenses/by-sa/3.0/. 2010. URL: https://commons.wikimedia.org/wiki/File:Dispersive_Prism_Illustration_by_Spigget.jpg (visited on 06/04/2024).

[103] Joseph von Fraunhofer. *Fraunhofer Spectrum Medium*. Wikimedia Commons. Licensed under CC BY-SA 4.0: https://creativecommons.org/licenses/by-sa/4.0/. 1815. URL: https://commons.wikimedia.org/wiki/File:Fraunhofer_Spektrum_Medium.jpg (visited on 06/04/2024).

[104] William W Parson. *Modern optical spectroscopy*. Vol. 2. Springer, 2007.

[105] Eugene Hecht. *Optics*. Pearson Education, 20. ISBN: 9780321188786.

[106] Roberto Cecchini and Guiseppe Pelosi. “Diffraction: the first recorded observation”. In: *IEEE Antennas and Propagation Magazine* 32.2 (1990), pp. 27–30.

[107] Kirill Poletkin. *Levitation micro-systems: Applications to sensors and actuators*. Springer Nature, 2020. ISBN: 9783030589103.

[108] Zhiqiu Lu. “Micromachined inductive suspensions with 3D wirebonded microcoils”. PhD Thesis. Albert-Ludwigs-Universität Freiburg, 2016.

[109] V Badilita, S Rzesnik, K Kratt, and U Wallrabe. “Characterization of the 2nd generation magnetic microbearing with integrated stabilization for frictionless devices”. In: *2011 16th International Solid-State Sensors, Actuators and Microsystems Conference*. IEEE. 2011, pp. 1456–1459.

[110] Kirill V Poletkin, Vlad Badilita, Zhiqiu Lu, Ulrike Wallrabe, and Christopher Shearwood. “Micromachined inductive contactless suspension: Technology and modeling”. In: *Magnetic Sensors and Devices*. CRC Press, 2017, pp. 101–132.

[111] Raymond A Serway, John W Jewett, and Vahé Peroomian. *Physics for scientists and engineers*. Thomson Brooks/Cole, 2003. ISBN: 9780495089971.

[112] Ian S Grant and William Robert Phillips. *Electromagnetism*. John Wiley & Sons, 2013.

[113] David J Griffiths. *Introduction to electrodynamics*. Pearson Education, 2013.

[114] C Shearwood, CB Williams, PH Mellor, RB Yates, MRJ Gibbs, and AD Mattingley. “Levitation of a micromachined rotor for application in a rotating gyroscope”. In: *Electronics Letters* 31.21 (1995), pp. 1845–1846.

[115] C Shearwood, CB Williams, PH Mellor, KY Chang, and J Woodhead. “Electro-magnetically levitated micro-discs”. In: *IEE Colloquium on Microengineering Applications in Optoelectronics*. IET. 1996, pp. 6–1.

[116] C Shearwood, KY Ho, CB Williams, and H Gong. “Development of a levitated micromotor for application as a gyroscope”. In: *sensors and actuators A: physical* 83.1-3 (2000), pp. 85–92.

[117] Weiping Zhang, Wenyuan Chen, Xiaolin Zhao, Xiaosheng Wu, Wu Liu, Xiaogang Huang, and Shiyi Shao. “The study of an electromagnetic levitating micromotor for application in a rotating gyroscope”. In: *sensors and actuators A: physical* 132.2 (2006), pp. 651–657.

[118] Xiaosheng Wu, Wenyuan Chen, Xiaolin Zhao, and Weiping Zhang. “Development of a micromachined rotating gyroscope with electromagnetically levitated rotor”. In: *Journal of Micromechanics and Microengineering* 16.10 (2006), p. 1993.

[119] CB Williams, C Shearwood, PH Mellor, AD Mattingley, MRJ Gibbs, and RB Yates. “Initial fabrication of a micro-induction gyroscope”. In: *Microelectronic Engineering* 30.1-4 (1996), pp. 531–534.

[120] V Badilita, K Kratt, T Burger, JG Korvink, and U Wallrabe. “3D high aspect ratio, MEMS integrated micro-solenoids and Helmholtz micro-coils”. In: *TRANSDUCERS 2009-2009 International Solid-State Sensors, Actuators and Microsystems Conference*. IEEE. 2009, pp. 1106–1109.

[121] Kai Kratt, Vlad Badilita, Tobias Burger, Jürgen Mohr, Martin Börner, Jan G Korvink, and Ulrike Wallrabe. “High aspect ratio PMMA posts and characterization method for micro coils manufactured with an automatic wire bonder”. In: *Sensors and actuators A: Physical* 156.2 (2009), pp. 328–333.

[122] K Kratt, V Badilita, T Burger, JG Korvink, and U Wallrabe. “A fully MEMS-compatible process for 3D high aspect ratio micro coils obtained with an automatic wire bonder”. In: *Journal of Micromechanics and Microengineering* 20.1 (2009), p. 015021.

[123] Erik Förster, Moritz Stürmer, Ulrike Wallrabe, Jan Korvink, and Robert Brunner. “Bio-inspired variable imaging system simplified to the essentials: modelling accommodation and gaze movement”. In: *Optics express* 23.2 (2015), pp. 929–942.

[124] Erik Förster, Moritz Stürmer, Ulrike Wallrabe, Jan Korvink, Patrick Bohnert, and Robert Brunner. “Dual-mode spectral imaging system employing a focus variable lens”. In: *Advanced Optical Technologies* 5.2 (2016), pp. 167–176.

[125] Patrick Bohnert. “Entwurf und Aufbau eines Prüfplatzes für Leiterplattengeräte”. Master’s thesis. Fachbereich SciTec, Ernst-Abbe-Fachhochschule Jena, Mar. 2014.

[126] Craig J Sansonetti, Marc L Salit, and Joseph Reader. “Wavelengths of spectral lines in mercury pencil lamps”. In: *Applied optics* 35.1 (1996), pp. 74–77.

[127] Craig ST Daughtry, CL Walthall, MS Kim, E Brown De Colstoun, and JE McMurtrey Iii. “Estimating corn leaf chlorophyll concentration from leaf and canopy reflectance”. In: *Remote sensing of Environment* 74.2 (2000), pp. 229–239.

[128] Anatoly A Gitelson, Yuri Gritz, and Mark N Merzlyak. “Relationships between leaf chlorophyll content and spectral reflectance and algorithms for non-destructive chlorophyll assessment in higher plant leaves”. In: *Journal of plant physiology* 160.3 (2003), pp. 271–282.

[129] Moritz Stürmer, Matthias C Wapler, Jana Schmitt, Friedemann Völklein, and Ulrike Wallrabe. “Phase gratings with tunable diffraction efficiency”. In: *Optics Express* 24.21 (2016), pp. 23765–23776.

[130] Stefan Schuhladen, Kaustubh Banerjee, Moritz Stürmer, Philipp Müller, Ulrike Wallrabe, and Hans Zappe. “Variable optofluidic slit aperture”. In: *Light: Science & Applications* 5.1 (2016), e16005–e16005.

[131] *Thorlabs Mounted Dove Prisms*. URL: `https://www.thorlabs.com/newgrouppage9.cfm?objectgroup_id=6810&pn=PS992M-A` (visited on 06/07/2019).

[132] Arie Zigler. “Apparatus for performing hyperspectral endoscopy”. US6529769B2. US Patent 6,529,769. Mar. 2003.

[133] Fuhong Cai, Jie Chen, Xiaofeng Xie, and Jun Xie. “The design and implementation of portable rotational scanning imaging spectrometer”. In: *Optics Communications* 459 (2020), p. 125016.

[134] Longqiang Luo, Shuo Li, Xinli Yao, and Sailing He. “Rotational hyperspectral scanner and related image reconstruction algorithm”. In: *Scientific Reports* 11.1 (2021), p. 3296.

[135] Zhiqiu Lu, Kirill Poletkin, Bartjan den Hartogh, Ulrike Wallrabe, and Vlad Badilita. “3D micro-machined inductive contactless suspension: Testing and modeling”. In: *Sensors and Actuators A: Physical* 220 (2014), pp. 134–143.

[136] Zhiqiu Lu, Kirill Poletkin, Ulrike Wallrabe, and Vlad Badilita. “Performance characterization of micromachined inductive suspensions based on 3D wire-bonded microcoils”. In: *Micromachines* 5.4 (2014), pp. 1469–1484.

[137] Kirill Poletkin, Z Lu, B den Hartogh, U Wallrabe, and V Badilita. “Stability and spring constant investigation for micromachined inductive suspensions: theoretical analysis vs. experimental results”. In: *Journal of Physics: Conference Series*. Vol. 557. 1. IOP Publishing. 2014, p. 012133.

[138] K Poletkin, Z Lu, U Wallrabe, and V Badilita. “Hybrid electromagnetic and electrostatic micromachined suspension with adjustable dynamics”. In: *Journal of Physics: Conference Series*. Vol. 660. 1. IOP Publishing. 2015, p. 012005.

[139] Kirill Poletkin, Zhiqiu Lu, Ulrike Wallrabe, and Vlad Badilita. “A new hybrid micromachined contactless suspension with linear and angular positioning and adjustable dynamics”. In: *Journal of Microelectromechanical Systems* 24.5 (2015), pp. 1248–1250.

[140] Kai Kratt, Marit Seidel, Markus Emmenegger, Ulrike Wallrabe, and Jan G Korvink. “Solenoidal micro coils manufactured with a wire bonder”. In: *2008 IEEE 21st International Conference on Micro Electro Mechanical Systems*. IEEE. 2008, pp. 996–999.

[141] Kai Kratt. “Microcoils manufactured with a wire bonder”. PhD Thesis. Albert-Ludwigs-Universität Freiburg, 2010.

[142] Ali Moazenzadeh. “Wirebonded microtransformers for power on-chip applications”. PhD Thesis. Albert-Ludwigs-Universität Freiburg, 2015.

[143] Z Lu, F Jia, J Korvink, U Wallrabe, and V Badilita. “Design optimization of an electromagnetic microlevitation system based on copper wirebonded coils”. In: *Proceedings of the 2012 Power MEMS, Atlanta, GA, USA* (2012), pp. 2–5.

# List of Own Publications

## Journal Articles

[MA1] Mohammad Abdo, Erik Förster, Patrick Bohnert, Vlad Badilita, Robert Brunner, Ulrike Wallrabe, and Jan G Korvink. “Dual-mode pushbroom hyperspectral imaging using active system components and feed-forward compensation”. In: *Review of Scientific Instruments* 89.8 (2018).

[MA2] Mohammad Abdo, Vlad Badilita, and Jan Korvink. “Spatial scanning hyperspectral imaging combining a rotating slit with a Dove prism”. In: *Optics Express* 27.15 (2019), pp. 20290–20304.

[MA3] Shervin Keshavarzi, Andras Kovacs, Mohammad Abdo, Vlad Badilita, Rui Zhu, Jan G Korvink, and Ulrich Mescheder. “Porous silicon based rugate filter wheel for multispectral imaging applications”. In: *ECS Journal of Solid State Science and Technology* 8.3 (2019). Licensed under CC BY 4.0: https://creativecommons.org/licenses/by/4.0/, Q43. URL: `https://doi.org/10.1149/2.0251902jss`.

## Conference Contributions

[MA4] Mohammad Abdo, Erik Förster, Patrick Bohnert, Moritz Stürmer, Vlad Badilita, Robert Brunner, Ulrike Wallrabe, and Jan G Korvink. “Automatic correction of diffraction pattern shift in a pushbroom hyperspectral imager with a piezoelectric internal line-scanning unit”. In: *Photonic Instrumentation Engineering IV*. Vol. 10110. SPIE. 2017, pp. 24–31.

[MA5] Shervin Keshavarzi, Andras Kovacs, Mohammad Abdo, Vlad Badilita, Jan Gerrit Korvink, and Ulrich M Mescheder. “Miniaturized porous silicon rugate filter wheel for multispectral imaging applications”. In: *MikroSystemTechnik 2019; Congress*. VDE. 2019, pp. 1–4.

[MA6] Sebastian Bauer, Wolfgang Krippner, Ding Luo, Miro Taphanel, Mohammad Abdo, Vlad Badilita, Thomas Längle, Jürgen Beyerer, Jan Korvink, and F Puente León. “Ortsaufgelöste optische Bestimmung von Materialanteilen in Mischungen”. In: *XXX. Messtechnisches Symposium*. Walter de Gruyter GmbH & Co KG. 2016, pp. 69–76.

## Patents

[MA7] Mohammad Abdo and Jan G. Korvink. “A method and a device for acquiring spatially-resolved spectral information”. EP3748317A1. Application EP19178381. Dec. 2020.

## Supervised Master’s Theses

1. Sagar Wadhwa, “Development of a Micro-Levitated Rotating Slit for Spatial Scanning Hyperspectral Imaging”, Master’s Thesis, Karlsruhe Institute of Technology (KIT), July 2017.

2. Sridivya Mukkavilli, “Spectral Imaging Using A MEMS Based Actuator”, Master’s Thesis, Hochschule Karlsruhe-Technik und Wirtschaft, December 2019.

# Acknowledgments

As I finally close this chapter of my life, I would like to express my heartfelt gratitude to everyone who has supported me throughout my doctoral journey.

First and foremost, I am sincerely thankful to my supervisor, Prof. Dr. Jan G. Korvink, for the opportunity to conduct my PhD research in his group. I am grateful for the time you dedicated to our monthly meetings, the freedom to pursue my ideas, the support for the collaborations I initiated, and for a comprehensive academic experience where I got to publish in journals, present at conferences, supervise students, apply for funding, and file for patent.

I would like to extend my gratitude and appreciation to my group leader, Dr. Vlad Badilita. I am grateful for your continuous support, guidance, and motivation. Your persistent push for results, mixed with your positive and friendly demeanor, created a great work environment and turned our group into a small family. Thank you for many fruitful discussions of my work and for many pleasant chats on our way to campus.

I would like also to thank Prof. Dr. rer. nat. Robert Brunner, the co-reviewer of my dissertation, for dedicating his time to review my work and for providing his valuable feedback.

All the fabrication work in this thesis was made possible by the support from the cleanroom staff and other colleagues at IMT. Many thanks to Dr. Uwe Köhler for the cleanroom introductions and guidance. Special thanks to Heike Fornasier and Barbara Matthis for their dedication and patience in processing the delicate thin glass wafers. The gratitude is extended to Marco Heiler for metal evaporation, Giuseppe Papagno for wafer dicing, Heino Besser for laser machining, and Randy Fechner and Sanaz Rastjoo for for wire bonder introductions. A heartfelt thank

you to my colleague and officemate, Dr. Hossein Davoodi, for fabricating so many beautiful microcoils for the levitation chips.

I would like also to thank Uwe Hollenbach, Dr. Arndt Last, and Daniel Münch for providing introductions to the Optics Lab and laser safety and for maintaining a well-organized and safe lab environment.

Special thanks and appreciation goes to my master students, Sagar Wadhwa and Sridivya Mukkavilli, for the countless hours they spent in the cleanroom working on the fabrication during their master's theses and for the valuable contribution they made to the realization of the new levitation chips.

My appreciation also to Prof. Dr. Fernando Puente León and Sebastian Bauer from IIIT for the early discussions on HSI miniaturization, which evolved into the PHARAO project proposal. My appreciation is extended to Prof. Dr. Thomas Längle from Fraunhofer IOSB for his kind invitations to the "AK Multispektral" meetings and the OCM Conference.

I would like to thank everyone at the Karlsruhe School of Optics and Photonics (KSOP) for the excellent professional development program that enriched my PhD studies. Special thanks to Stefanie Peer for her continuous support and for making these opportunities accessible to everyone in the program. I also would like to thank Prof. Dr. Orestis Terzidis and Benedict Heblich from the Institute of Entrepreneurship, Technology Management & Innovation (EnTechnon) for their inspiring sessions on entrepreneurship and insightful discussions on startups and personal values.

As part of the KSOP program, I had the pleasure of having Dr. Martin Lauer from the Institute of Measurement and Control Systems (MRT) as a mentor. I would like to thank him for his time, advice, and support during our meetings.

Spending my PhD years with such a wonderful group of people in Prof. Korvink's group and at IMT has been a privilege. Special heartfelt thanks to my officemates–Shyam, Hossein, Diana, and Albina–for the fun times and beautiful memories in office 244. Thanks to Asa and Ronald for being my sounding board on optics, Kirill Poletkin for insightful discussions on levitation, Lorenzo for making long commutes and train delays between Freiburg and Karlsruhe more bearable, and Pedro for good times during our MBA courses and our entrepreneurial journey.

My sincere gratitude to my dear friend, Karim Salem, for being there for me during one of the most difficult times in my life after my father passed away.

My deepest gratitude goes to my family, whose unconditional love and support gave me the strength and patience to finish this thesis. To my beloved wife, Samar, for being by my side every step of the way with endless love, encouragement, and support. To my son, Faris, and my daughter, Layla, for being the sunshine in my life, filling it with love and joy. To my sister, Sara, and my brother, Yousef, for always lifting up my mood and spirit.

Finally, to my beloved parents, words cannot fully express my gratitude for your boundless love, support, and sacrifice. To my mother, Dr. Entesar, your constant encouragement and unwavering faith in me have been the bedrock of my success. I am endlessly grateful for your love and the countless ways you have lifted me up. To my father, Dr. Refaat, whom I miss every day, I wish more than anything that I could share this achievement with you. Your wisdom, kindness, and belief in me continue to be my greatest source of inspiration. Your spirit lives on in everything I do. May you rest in peace.